Developing Nucleic Acid-Based Sensors and Actuators

by

Raphaël Vincent Gayet

M.Sc., École Polytechnique Fédérale de Lausanne (2016)
M.Res., École Normale Supérieure de Lyon – Université Claude Bernard de Lyon (2016)
B.Sc., École Normale Supérieure de Lyon – Université Claude Bernard de Lyon (2013)

Submitted to the Department of Biology,
in partial fulfillment of the requirements for the degree of

Doctor of Philosophy

at the

Massachusetts Institute of Technology

September 2022

Signature of Author .....

Microbiology Graduate Program
August 26, 2022

Certified by .....

James J. Collins, Ph.D.
Henri A. Termeer Professor of Medical Engineering and Science
Professor of Biological Engineering
Thesis supervisor

Accepted by .....

Jacquin C. Niles, M.D., Ph.D.
Associate Professor of Biological Engineering
Chair of Microbiology Program

Developing Nucleic Acid-Based Sensors and Actuators

by

Raphaël Vincent Gayet

Submitted to the MIT Department of Biology on August 31st, 2022
in partial fulfillment of the requirements for the degree of
Doctor of Philosophy in Microbiology

ABSTRACT – As the field of synthetic biology matures, engineers are tackling increasingly ambitious problems that require the integration of regulatory logic in complex environments. Nucleic acids are attractive molecules for designing sense-and-respond modules: they are ubiquitous, information-rich and interact with each other through simple rules. Here, through two examples, I show that nucleic acids are particularly suited to create programmable molecular tools, in which inputs and outputs are defined independently from each other. In the first half of this thesis, I describe the development of a strategy to design nucleic acid-responsive materials using the CRISPR-associated nuclease Cas12a as a user-programmable sensor and material actuator. I exploit the programmability of Cas12a to actuate hydrogels containing DNA as an anchor for pendant groups or as a structural element. This versatile approach improves on the sensitivity of current DNA-responsive materials while enabling their rapid repurposing toward new sequence targets. In the second half of this thesis, I describe how to engineer programmable single-transcript RNA sensors *in vivo*, in which adenosine deaminases acting on RNA (ADARs) autocatalytically convert target hybridization into a translational output. This system amplifies the signal from editing by endogenous ADAR through a positive feedback loop. This topology confers high dynamic range, low background, minimal off-target effects, and a small genetic footprint. I envision that the approaches described here have broad applications from basic science to advanced diagnostics and therapeutics, illustrating the great potential of programmable nucleic acid-based controllers.

Thesis Advisor: James J. Collins, Ph.D.
Title: Henri A. Termeer Professor of Medical Engineering and Science
Professor of Biological Engineering

« La lutte elle-même vers les sommets suffit à remplir un cœur d'homme.
Il faut imaginer Sisyphe heureux. »

— Albert Camus, *Le Mythe de Sisyphe* (1942)

Table of Contents

List of Figures

List of Tables

Acknowledgements

The work compiled in this thesis, and my whole graduate school experience, would not have been possible is it were not for the incredible support I have received from my family, friends, colleagues and mentors.

I want to start by thanking my advisor, James Collins, whose mentorship greatly contributed to making me the scientist that I am today. By generously offering me to join his team, and through his unwavering support, Jim fostered my scientific enthusiasm and creativity over the years. I am also indebted to the members of my committee, Kristala Prather and Kevin Esvelt, who were not only great supports even when my projects took unexpected turns, but also role models who made sure that graduate school was an opportunity for me to grow as a scientist. Thank you to Ming-Ru Wu, who taught me so much about synthetic biology, and kindly accepted to share his expertise by reviewing this work.

During my time at MIT, I was lucky to meet, work with, and befriend truly exceptional people. I want to thank all my coauthors, whose dedication and talent made the work presented here possible. I have learnt from every single one of my colleagues in the Collins Lab, and the impact that such bright minds have had on my learning experience cannot be overstated. I thank them for welcoming me in the team, and for sharing their commitment and their enthusiasm in the pursuit of bold new ideas.

As I was writing this thesis and preparing to defend it, I reflected on the learning journey behind me. It started long before I joined MIT, and I owe a great deal to all

the people who took a chance on me, and opened doors along the way. In particular, René Blanchet, Mark Howarth, Samy Gobaa and Timothy Lu have been instrumental in my academic progress. I thank them for the opportunities they offered me and that ultimately lead me to graduate school.

Finally, and most importantly, I want to thank all the people who supported me from across the Atlantic; for that, of course, I feel that I must write in French. À Pierre: merci de m'avoir montré qu'une simplicité bienveillante peut déplacer les montagnes. À mon Grand-Père: je l'ai enfin trouvé, ce mystérieux sujet de thèse. J'aurais aimé pouvoir te le décrire, et j'espère que tu en aurais été fier. À ma Môman: ils paraissent bien loin, les « *huit fois sept, cinquante-six* », mais ces petits pas ont été le début d'un grand et long chemin. Merci de m'avoir appris à apprécier tout ce que la Nature a de beau et de poétique. À mon Pôpa: merci de m'avoir transmis le goût de l'effort et le sens du travail bien fait. Ce sera toujours toi, le vrai Docteur Gayet. Enfin, à mon Teuteu: merci d'être depuis toujours une inspiration, un modèle de résilience, et une épaule sur laquelle m'appuyer dans mes moments de doute. Bref, à ma famille: vous m'avez tout appris; la persévérance, l'intégrité, la curiosité, la capacité de s'émerveiller – tout ce sans quoi l'exercice scientifique serait bien futile. Je ne saurais exprimer combien votre soutien compte pour moi au quotidien. Les mots me manquent pour vous dire à quel point votre support inconditionnel a été source de réconfort et de force.

De tout mon cœur : merci.

The research work presented here, as well as exploratory work that did not make it into this thesis, was generously supported by funding from the following sources: the Air Force Basic Research Initiative program, the Defense Threat Reduction Agency, the MIT Abdul Latif Jameel Clinic for Machine Learning in Health, the MIT Department of Biology, the MIT Microbiology Graduate Program, the National Institute of Health (NIBIB/NIDDK), the Paul G. Allen Frontiers Group, and the Wyss Institute for Biologically Inspired Engineering at Harvard University.

Note on Previous Publications and Author Contributions

A large portion of the work presented in this thesis is either published in the scientific literature, or undergoing the peer-review process at the time of writing of this dissertation. In particular, parts of this work were partially reprinted or adapted (with the authors and publishers' authorization) from the following articles and manuscripts:

- English, M.A.[†], Soenksen, L.R.[†], **Gayet, R.V.**[†], de Puig, H.[†], Angenent-Mari, N.M.[‡], Mao, A.S.[‡], Nguyen, P.Q. and Collins, J.J. (2019). Programmable CRISPR-responsive smart materials. Science *365*, 780-785. ([†,‡] *denote equal contributions*)

- **Gayet, R.V.**[†], de Puig, H.[†], English, M.A.[†], Soenksen, L.R.[†], Nguyen, P.Q., Mao, A.S., Angenent-Mari, N.M. and Collins, J.J. (2020). Creating CRISPR-responsive smart materials for diagnostics and programmable cargo release. Nature Protocols *15*, 3030-3063. ([†] *denotes equal contributions*)

- English, M.A.[†], **Gayet, R.V.**[†] and Collins, J.J. (2021). Designing biological circuits: synthetic biology within the operon model and beyond. Annual Review of Biochemistry *90*, 221-244. ([†] *denotes equal contributions*)

– **Gayet, R.V.**[†], Ilia, K.[†], Razavi, S.[†], Tippens, N.D.[†], Lalwani, M.A., Zhang, K., Chen, J.X., Chen, J.C. and Collins, J.J. (2022). Autocatalytic base editing for RNA-responsive translational control. [Manuscript under review] ([†] *denotes equal contributions*)

As is often the case in science, the work listed above is the product of successful collaborations between scientists of diverse backgrounds, who combined their individual expertises to imagine, design and implement new ideas. It seems difficult – if not impossible – to perfectly define where everyone's contributions started and ended, especially since many experiments were conducted by several people at the same time. My work in the CRISPR-actuated biomaterials project was particularly focused on hydrogel chemistry and Cas-based actuation (with an emphasis on PEG-based implementations), and my work on programmable cellular riboregulator was focused on sequence design and prototyping.

List of Abbreviations

AAV ..... Adeno-associated virus
ADAR ..... Adenosine deaminase acting on RNA
ALP ..... Alkaline phosphatase
ANOVA ..... Analysis of variance
AuNP ..... Gold nanoparticle
APS ..... Ammonium persulfate

BCIP ..... 5-Bromo-4-chloro-3-indolyl phosphate
BFP ..... Blue fluorescent protein
BMP-2 ..... Bone morphogenic protein 2

C6 ..... 6-carbon chain linker
CAS ..... Chemical abstracts service (number)
Cas ..... CRISPR-associated (nuclease)
CB ..... Carbon black
cDNA ..... Complementary DNA
CFSE ..... Carboxyfluorescein succinimidyl ester
CL ..... Closed loop
CRISPR ..... Clustered regularly interspaced short palindromic repeats

DMEM ..... Dulbecco's modified Eagle's medium
DNA ..... Deoxyribonucleic acid
dsDNA ..... Double-stranded DNA
dsRNA ..... Double-stranded RNA
DTPA ..... Dithiol phosphoramidite

EBOV ..... Ebola virus

EDTA . . . . . Ethylenediaminetetraacetic acid

FACS . . . . . Fluorescence-assisted cell sorting
FAM . . . . . Carboxyfluorescein
FBS . . . . . Fetal bovine serum
FITC . . . . . Fluorescein isothiocyanate
FQ . . . . . Fluorescence quencher

GFP . . . . . Green fluorescent protein
gRNA . . . . . Guide RNA

HRP . . . . . Horseradish peroxidase

IDE . . . . . Interdigitated electrode
IVT . . . . . *In vitro* transcription
IRES . . . . . Internal ribosome entry site

KSHV . . . . . Kaposi's sarcoma herpesvirus / human herpesvirus 8

LAMP . . . . . Loop-mediated isothermal amplification

MCP . . . . . Major coat protein
MCS . . . . . Multiple cloning site
mRNA . . . . . Messenger RNA
MRSA . . . . . Methicillin-resistant *Staphylococcus aureus*

NBT . . . . . Nitro blue tetrazolium chloride
NES . . . . . Nuclear export signal
NGS . . . . . Next-generation sequencing
NLS . . . . . Nuclear localization signal

OL . . . . . Open loop

PA . . . . . Polyacrylamide
PAM . . . . . Protospaced-adjacent motif

PAN-ENE ..... Polyadenylated nuclear RNA expression and nuclear retention element
PBMC ..... Peripheral blood mononuclear cell
PBS ..... Phosphate buffered saline
PCR ..... Polymerase chain reaction
PEG ..... Poly(ethylene glycol)

qPCR ..... Quantitative PCR

RFID ..... Radio frequency identification
RNA ..... Ribonucleic acid
RPA ..... Recombinase polymerase amplification
RSSI ..... Received signal strength indicator
RT ..... Reverse transcription
RBS ..... Ribosome binding site

SDA ..... Strand displacement amplification
SH ..... Thiol
SINE ..... Short interspersed nuclear elements
SIRLOIN ..... SINE-derived nuclear RNA localization
ssDNA ..... Single-stranded DNA
ssRNA ..... Single-stranded RNA

TCEP ..... Tris(2-carboxyethyl)phosphine
TEA ..... Triethanolamine
TEMED ..... N,N,N',N'-Tetramethylethylenediamine

UHF ..... Ultra-high frequency
UTR ..... Untranslated region

VS ..... Vinylsulfone

ZFN ..... Zinc finger nuclease

μPAD ..... Microfluidic paper-based analytical device

CHAPTER 1

Introduction

1.1 The interplay of forward and reverse engineering in life sciences

Biology can be thought of as the daunting process of deciphering the formidable complexity of living systems. To do so, life scientists typically work backward, starting from observable functional processes selected by evolution; they attempt to pinpoint the key players involved, and deconstruct how they interact with each other to explain their emergent properties. In turn, as major cellular and molecular mechanisms are identified, research increasingly focuses on systematically defining in which processes a given biological molecule is involved [Weissman, 2010]. In both of these processes, a wealth of engineering approaches, for instance derived from control and systems theory, can be applied to help biologists understand the behavior of complex cellular systems [Alon, 2006; Iglesias & Ingalls, 2009].

The biochemical and genetic characterization of cellular mechanisms has, in turn, enabled the emergence of a new engineering discipline. A little over twenty years ago, two landmark papers described the assembly of synthetic gene networks in living

cells: a genetic toggle switch [Gardner *et al.*, 2000] and a synthetic genetic oscillator or "repressillator" [Elowitz & Leibler, 2000]. These seminal works demonstrated that well-defined biological "parts" (e.g. genes) could be combined to build larger circuits and generate pre-programmed behaviors in biological systems. Since then, synthetic biology has emerged as a powerful framework for hypothesis testing in biological research. Minimal and well-controlled analogues of complex systems can be studied in isolation, while synthetic reporter modalities can be used to create human-interpretable readouts of natural biological processes [Bashor & Collins, 2018]. Most notably, early efforts in synthetic biology have played an important role in fundamental investigations into the architectures of gene regulatory networks [Becskei & Serrano, 2000; Guido *et al.*, 2006; Hooshangi *et al.*, 2005; Isaacs *et al.*, 2003], as well as the origins and the functional consequences of noise in cells [Blake *et al.*, 2003; Elowitz *et al.*, 2002; Ozbudak *et al.*, 2002; Rosenfeld *et al.*, 2005].

There is a permanent, constructive interplay between fundamental and synthetic biology. Progress in metagenomics highlights the existence of a hugely diverse repertoire of biomolecules and sequences with untapped potential, which are yet to be characterized [Almeida *et al.*, 2019; Johns *et al.*, 2018; Sberro *et al.*, 2019]. As biochemical and molecular studies provide a better understanding of new biological components, these are co-opted as tools for synthetic biology. In turn, engineers assemble synthetic programs and devices from first principles, providing a "proof-by-construction" for biological hypotheses.

1.2 The need for programmable tools in synthetic biology

As an engineering discipline, synthetic biology has always been motivated by its applications to real-world challenges. These include the design of therapeutic and diagnostic devices, as well as the industrial or on-demand production of fuels, complex chemicals, medicines, and materials [Khalil & Collins, 2010; Meng & Ellis, 2020; Voigt, 2020]. Yet progress has been slower than anticipated and after twenty years the number of mature, widely-adopted technologies remains low. Significant constraints on the scope and utility of the behaviors that we can program into biological systems still hamper translation into clinics and industrial pipelines. As we move away from toy systems and towards synthetic tools that operate in real-world contexts, the types of behaviors that need to be detected or generated is often dictated by the application rather than the ease of manipulation. In other words, to harness the information processing and chemical capabilities of living organisms and achieve the goals envisaged for new biotechnologies, synthetic tools must be better integrated into arbitrary operational environments. This requirement calls for platform technologies that are easily repurposed to operate in new contexts. The development of molecular tools suited to the detection of user-defined cues and the programmable actuation of complex behaviors is therefore an important step towards the ambitious goals of synthetic biology.

1.3 A key role for nucleic acid-based technologies

Nucleic acids are intrinsically well-suited for the development of versatile sense-and-response modules. Both DNA and RNA are, by essence, information-rich molecules.

The former is a stable molecule encoding the identity of virtually every living being, as well as clinically relevant phenotypes (e.g. the presence of drug resistance genes, or somatic mutations)[CRyPTIC Consortium, 2018; Mustjoki & Young, 2021]; it is therefore an attractive target for the development of diagnostics and environmental sensing technologies. The latter, while more transient, provides information about cell states and types – for example across the different organs of a multicellular organism [Tabula Sapiens Consortium, 2022], in which cells are almost identical at the DNA level. In both cases, the simplicity of Watson-Crick base pairing rules facilitates the design of molecules hybridizing to sequences of interest. These properties suggest that biological sensors can be created based on the specific pairing between complementary nucleic acid molecules, provided that the interaction between a biological target and an engineered sensor can be coupled to a functional output.

In this thesis, we explore different ways to detect nucleic acids through the means of "interpreter" proteins; we exploit the conditional activity of these proteins to link the specific base pairing between nucleic acids to an enzymatic activity, from which we generate a variety of downstream responses. In a first example (Chapter 2), we describe how a CRISPR-based diagnostic strategy can be adapted to create bio-responsive materials, thereby coupling a programmable nucleic acid signal into a macro-scale chemical or physical actuation [English *et al.*, 2019; Gayet *et al.*, 2020]. Then, in Chapter 3, we focus on how within a cell, endogenous RNA editing enzymes can be harnessed to create specific and sensitive sense-and-respond genetic controllers [Gayet *et al.*, 2022].

CHAPTER 2

Programmable CRISPR-Responsive Smart Materials

2.1 Background, Motivation

Microbial clustered regularly interspaced short palindromic repeats (CRISPR) and CRISPR-associated (Cas) adaptive immune systems contain RNA-guided endonucleases capable of multiple-turnover nucleic acid hydrolysis [Chen *et al.*, 2018; Li *et al.*, 2018]. Because of their specificity and programmability, CRISPR-Cas enzymes have been exploited as efficient genome-editing tools [Knott & Doudna, 2018] and in nucleic acid diagnostic applications such as SHERLOCK [Gootenberg *et al.*, 2018, 2017] and DETECTR [Chen *et al.*, 2018].

Biologically responsive materials are important for biotechnology applications, including the fabrication of scaffolds for tissue engineering [Gjorevski *et al.*, 2016], the actuation of microfluidic valves [Na *et al.*, 2018], and the detection of analytes in sensors [Kahn *et al.*, 2015; Qin *et al.*, 2018]. DNA-responsive hydrogels are well suited to interface with synthetic DNA constructs or naturally occurring extracellular DNA [Heitzer *et al.*, 2015]. Current DNA-responsive hydrogels typically rely on strand displacement or structural changes in DNA cross-linkers [Cangialosi *et al.*, 2017; Yang *et al.*, 2008],

which require high concentrations of DNA triggers for actuation. Adapting such DNA hydrogels for activation with new trigger sequences involves the modification of nucleic acid components, which can conflict with the structural requirements (for example, length or secondary structure) imposed by the material. This limits the programmability of these systems and highlights the need for a strategy that uncouples structural and sensing constraints in DNA-based materials.

We use Cas enzymes to control the properties of hydrogels with integrated DNA components at multiple scales and in a modular fashion and thereby eliminate the need to encode target-sequence specificity into the gel structure. Our material platform is able to induce changes in hydrogels in response to user-defined target nucleic acid sequences by replacing a single component, a CRISPR guide RNA (gRNA) that governs sequence-specific Cas activation. We engineered different DNA-based materials to demonstrate a variety of nuclease-mediated responses, including the release of small molecules, enzymes, nanoparticles (NPs), and live cells, as well as the modulation of bulk electrical and permeability properties of DNA hydrogels for sensing and diagnostics (Figure 1).

2.2 Results

2.2.1 Cas12a has both targeted and collateral deoxyribonuclease activities

The Cas12a from *Lachnospiraceae* bacterium ND2006 [Chen *et al.*, 2018; Li *et al.*, 2018] displays a specific cleavage activity toward double-stranded DNA (dsDNA) fragments matching the gRNA spacer sequence (targeted cleavage) and subsequent indiscriminate single-stranded DNA (ssDNA) hydrolysis activity (collateral cleavage, Figure 2). Once the Cas12a-gRNA complex binds and cleaves its dsDNA target, the collateral cleavage

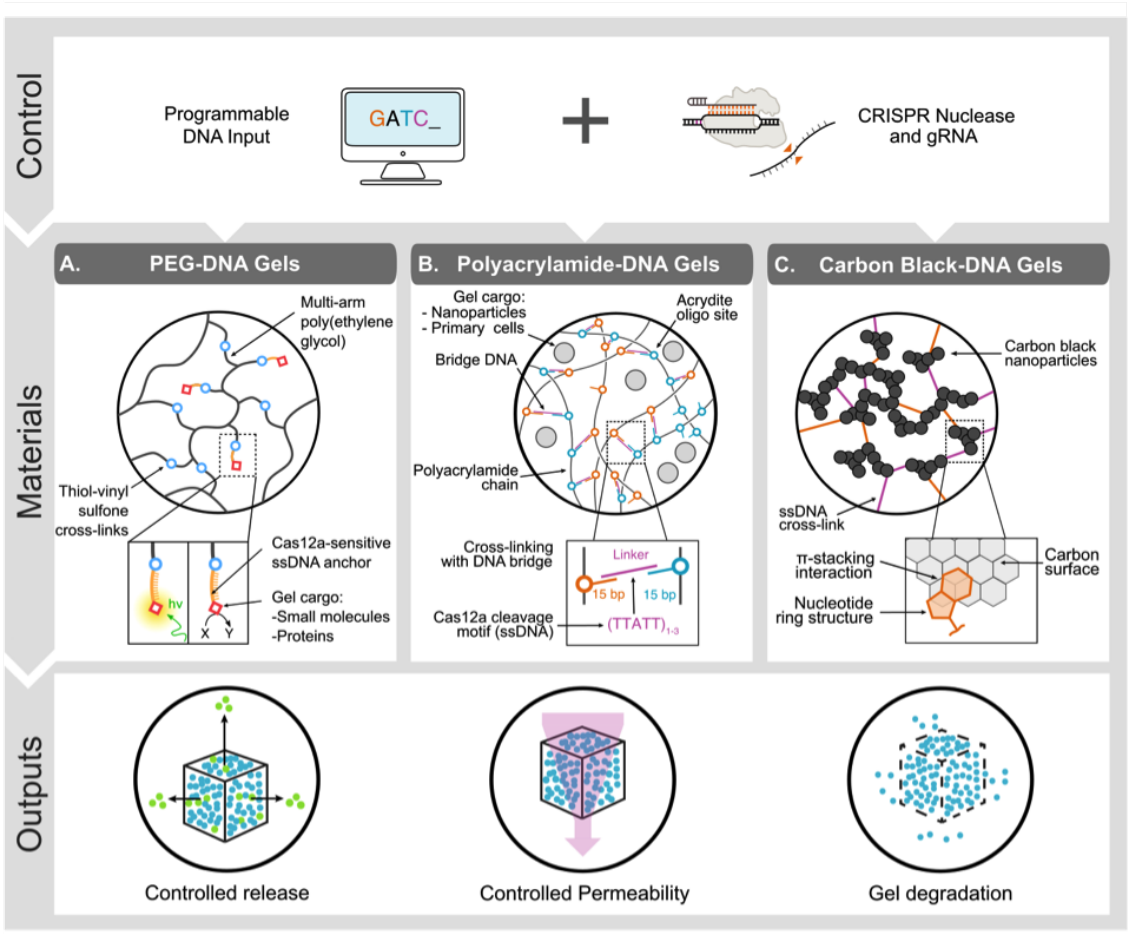

Figure 1 – CRISPR-mediated DNA-hydrogel modulation. RNA-guided Cas endonucleases can be easily programmed for specific DNA inputs (top panel) and used in combination with different hydrogel chemistries (middle panel) to modulate system properties at multiple scales, such as controlled release of molecules, particles, or live cells; fluid permeability; and bulk material degradation (bottom panel). Three basic CRISPR-gel systems were explored: (A) branched poly(ethylene glycol)-based hydrogels for release of DNA-anchored compounds; (B) degradable polyacrylamide-DNA hydrogels for release of encapsulated payloads (e.g., particles or live cells), as well as for controlling permeability of microfluidic systems via cleavage of a hydrogel ssDNA linker; and (C) conductive carbon black-DNA hydrogels for electrical circuit bridging with fuse-like responsiveness to dsDNA trigger activation. All presented CRISPR-gels respond to activation of a Cas12a-gRNA complex through the presence of a dsDNA trigger, and are designed to leverage either the highly specific dsDNA targeted cleavage activity of Cas12a for multiplexed response or the high-turnover ssDNA collateral cleavage activity of Cas12a to modulate large-scale hydrogel properties.

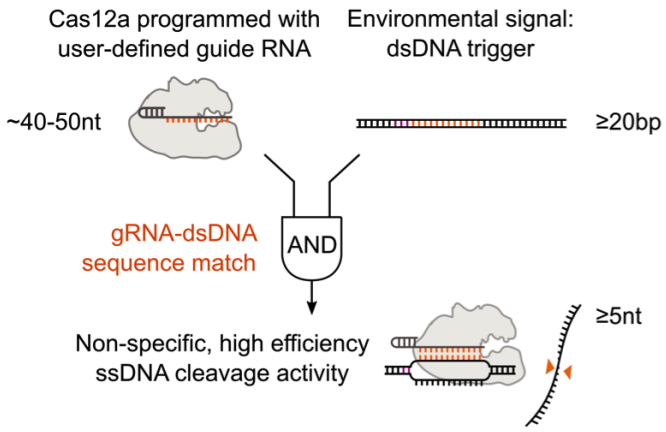

Figure 2 – Cas12a activation by dsDNA. The sequence specificity of Cas12a is programmed by a gRNA. Recognition and binding of the corresponding dsDNA trigger activates the ssDNA collateral cleavage activity.

of nearby ssDNA by Cas12a is highly efficient (1250 turnovers per second) [Chen *et al.*, 2018]. To demonstrate the target programmability of CRISPR gels, we tested gRNAs to detect fragments of the *mecA* antibiotic-resistance gene of methicillin-resistant *Staphylococcus aureus* (MRSA). We selected MRSA as a clinically relevant model to demonstrate the target programmability of CRISPR gels, given the high concentration of extracellular DNA in MRSA biofilms [Sugimoto *et al.*, 2018].

We first validated the collateral cleavage activity of Cas12a-gRNA in solution. Cleavage of an ssDNA reporter containing a quenched fluorophore by Cas12a in response to *mecA* dsDNA triggers confirmed the performance of the MRSA gRNA; Cas12a programmed with this gRNA detected its cognate trigger down to 16 pM in solution (Figure 3) and was selected for subsequent experiments. Sequence mismatches between the gRNA and trigger reduced the collateral cleavage rate, consistent with previously reported patterns [Chen *et al.*, 2018; Kleinstiver *et al.*, 2016]. Nonspecific activation of Cas12a by a scrambled dsDNA sequence was over 100-fold lower than that by the *mecA*

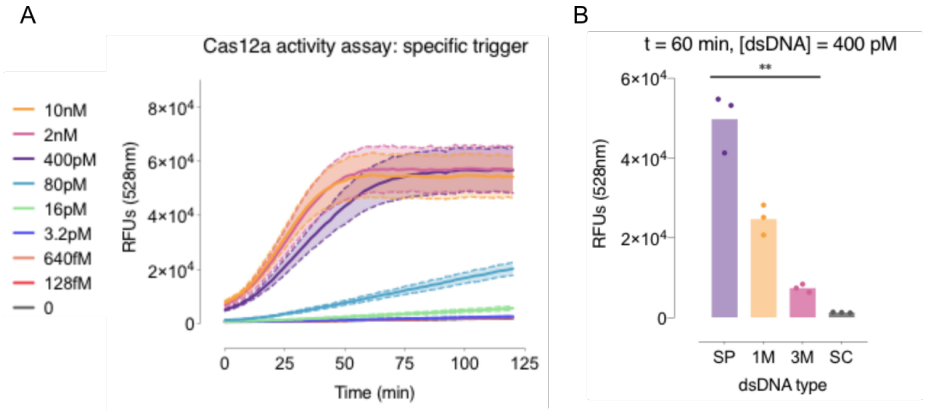

Figure 3 – In-solution validation of Cas12a-based detection system for *mecA*. (A) Fluorescence time-course results for MRSA gRNA Cas12a collateral cleavage assays with decreasing concentrations of a specific (SP) dsDNA trigger in solution. (B) We repeated the same experiment as in panel (A), except that the dsDNA trigger contained one mismatch (1M), three mismatches (3M) or was a randomly permutated control sequence (scrambled, SC). All reactions contained 50 nM Cas12a, 62.5 nM MRSA gRNA, 750 nM quenched fluorescently labeled ssDNA reporter and the specified concentrations of dsDNA triggers. The sequence of the fluorescently labeled reporter was: 5'(6FAM)-TTATT-(Iowa Black FQ)3'. As the number of nucleotide mismatches between the trigger and the gRNA increased, the rate of ssDNA collateral cleavage and the corresponding fluorescence signal at t = 60 min decreased. Statistics represent results from a Brown-Forsythe ANOVA ($p = 0.002$, with $p < 0.05$ for all Games-Howell's multiple comparison tests between means).

trigger (Figure 3). Cas12a's high dsDNA target specificity and rapid nonspecific ssDNA collateral cleavage activity make it an ideal candidate for modulating a wide range of physical and mechanical hydrogel properties.

Programmable materials capable of the controlled release of soluble compounds, as well as encapsulated cells, have broad utility in various therapeutic and research applications [Li & Mooney, 2016; Martino *et al.*, 2014; Purcell *et al.*, 2014; Rosales & Anseth, 2016]. Because of the diversity of DNA-based hydrogels in the literature, we selected material formulations that span a wide range of physical properties to demonstrate that they could be actuated by Cas proteins: (*i*) poly(ethylene glycol) (PEG) hydrogels with

covalently bound nonstructural DNA pendants that are released by Cas12a nuclease activity without degrading the overall hydrogel structure; (*ii*) acrylamide hydrogels with structural ssDNA cross-links that could be cleaved by Cas12a, resulting in bulk gel degradation as well as particle or cell release; and (*iii*) conductive hydrogels loaded with carbon black (CB) that were cleaved from the surface of electrodes by Cas12a, thus behaving like an electronic fuse.

2.2.2 Collateral Cas12a activity releases ssDNA-anchored cargos from hydrogel matrices

The targeted dsDNA cleavage activity of Cas12a can be used to preferentially release anchored cargos with near-single turnover; however, we focused on the collateral ssDNase activity of the enzyme, as it allows for the efficient transduction of external stimuli into changes in material properties through catalytic signal amplification. To illustrate the programmable actuation of materials using Cas12a, we covalently tethered a fluorophore (Cy3) into PEG hydrogels through an ssDNA linker (Figure 4) and monitored its release into solution upon Cas12a-induced cleavage (Figure 5). The Cas12a-gRNA complex alone was insufficient to catalyze cargo release; however, introduction of the *mecA* dsDNA trigger initiated the hydrolysis of ssDNA anchors (Figure 6B). By contrast, a randomly permutated version of the *mecA* dsDNA (scrambled control) failed to do so. We then used horseradish peroxidase (HRP) enzyme as a model for larger biomolecule payloads, demonstrating that biological function was preserved after immobilization in hydrogels using ssDNA anchors and subsequent release by Cas12a (Figure 6C). Within 10 min of exposure to a low-concentration (10 nM) dsDNA stimulus, we detected sufficient HRP activity in the supernatant for a visual readout (Figure 6C, inset). Further incubation allowed us to routinely discriminate trigger and scrambled dsDNA down

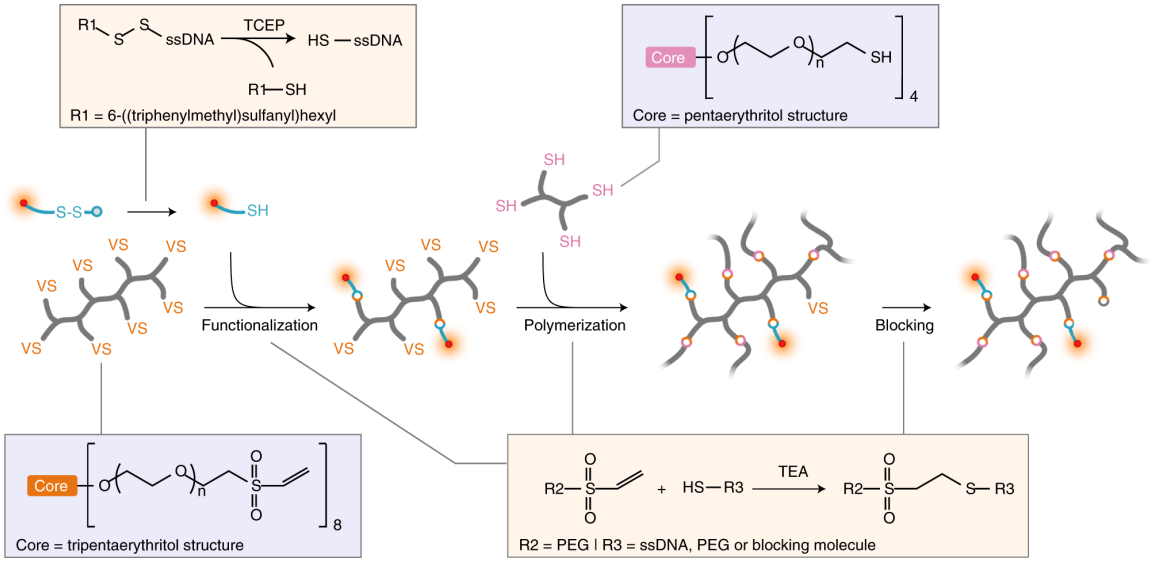

Figure 4 – Synthesis of PEG hydrogels harboring ssDNA-tethered molecules; ssDNA acts as a cleavable linker for attaching payloads to an inert PEG matrix. First, oligonucleotides (blue) carrying molecules of interest (red) on their 3' termini must be treated with a non-thiol reducing agent (TCEP) to deprotect the 5'-thiol reactive groups. The 8-arm vinyl sulfone (VS)-functionalized PEG macromers (orange) undergo three successive rounds of TEA-catalyzed thiol–ene Michael additions: first with the DNA anchors to graft the cargo molecules, then with thiol (SH)-functionalized 4-arm PEG macromers (pink) to polymerize the gels and finally with a blocking thiol.

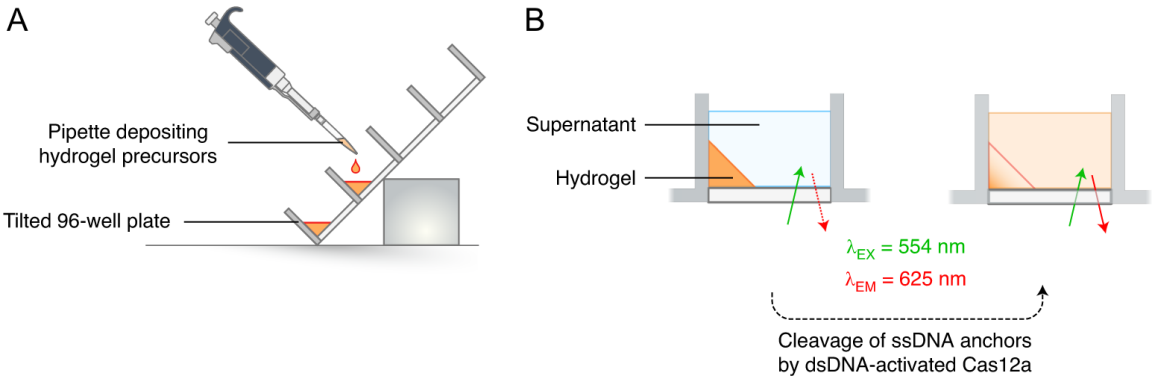

Figure 5 – (A) In our setup, the measurement plate is tilted on a support to ensure consistency when depositing precursors on the sides of the wells. (B) The release of cargo can be observed in real time by measuring the fluorescence increase in the hydrogel supernatant. The fluorometer is calibrated to measure signals on the side of the well opposite from the fluorophore-loaded material, to ensure that the signal recorded is generated only by molecules released into solution.

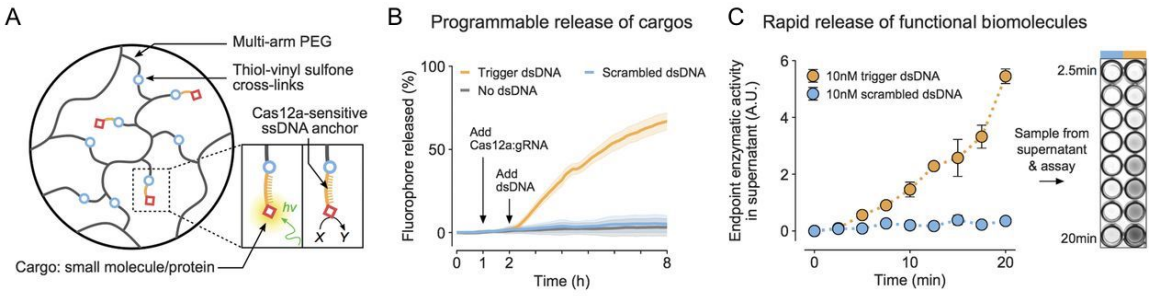

Figure 6 – Release of payloads from PEG hydrogels. (A) ssDNA acts as a cleavable linker for attaching payloads to an inert PEG matrix. hν, light energy. (B) Release of a tethered fluorophore by Cas12a is initiated only upon introduction of a specific dsDNA trigger and not a scrambled dsDNA control sequence. (C) Functional enzymes can be anchored into the hydrogel and released by Cas12a in sufficient quantities for visual detection in an HRP activity assay within minutes. A.U., arbitrary units. Plots show mean ± SD for n ≥ 3 replicates.

to 100 pM using HRP activity as a readout. These experiments are consistent with the efficient ssDNase activity of activated Cas12a [Chen *et al.*, 2018].

To demonstrate that changes to the gRNA were sufficient to entirely reprogram the target responsiveness of the material, we designed gRNAs to target a panel of genes involved in *S. aureus* antibiotic-resistance mechanisms. These include the antibiotic-resistance genes *ermA* and *ermC* [Arthur *et al.*, 1990; Strommenger *et al.*, 2003], the virulence factor gene *spa* [Okolie *et al.*, 2015], and the vancomycin-resistance gene *vanA* [Qureshi *et al.*, 2014]. Out of 25 combinations of gRNAs and dsDNA, those in which the sequence of the trigger matched the gRNA resulted in substantially higher fluorophore payload release from the hydrogel matrix (Figure 7). These results correlated to similar observations of the reactions performed in solution, and suggest that different gRNA-trigger pairs activate Cas12a to different extents [Chen *et al.*, 2018].

For many applications, the rate at which a molecule is delivered from a carrier conveys important biological information [Li & Mooney, 2016]. The speed of CRISPR-mediated hydrogel actuation corresponds to the amount of input dsDNA; conversely,

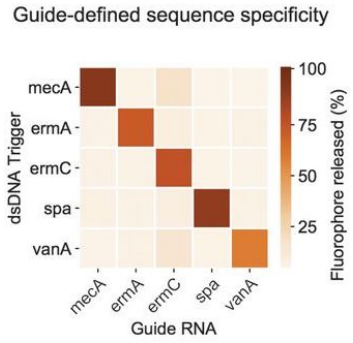

Figure 7 – Input programmability of Cas12a-mediated PEG hydrogel actuation. Activation of Cas12a and fluorophore release (t = 8 hours) is defined by the complementarity between a dsDNA sequence and the gRNA of Cas12a. Plots show mean ± SD for n ≥ 3 replicates.

for a given level of input, the response dynamics can be hard-coded into the system by altering the properties of the starting material (Figure 8). For example, pore size is expected to alter the mobility of macromolecules in polymer networks [Wang *et al.*, 2018]. On the basis of our macroscopic observations of programmed anchor hydrolysis, we hypothesized that this could be used to further tune the relationship between dsDNA input and Cas12a-mediated response. By modulating the cross-linking density of a PEG-DNA hydrogel and measuring the rate of fluorophore release by Cas12a-gRNA, we established another strategy by which the behavior of the CRISPR-responsive material could be controlled (Figure 8B).

In addition to controlling global dynamics of ssDNA cleavage through bulk material properties, we capitalized on the sequence-defined, addressable nature of the ssDNA linkers and the selectivity of the collateral cleavage activity of Cas12a for ssDNA over dsDNA [Chen *et al.*, 2018; Li *et al.*, 2018]. We attached two different fluorophores (Cy3 and 6-FAM) into PEG hydrogels with distinct ssDNA linkers and preprogrammed the differential sensitivity of one linker over the other to Cas12a collateral degradation by hybridizing it with a complementary blocking strand *in situ*. Whereas the release of the

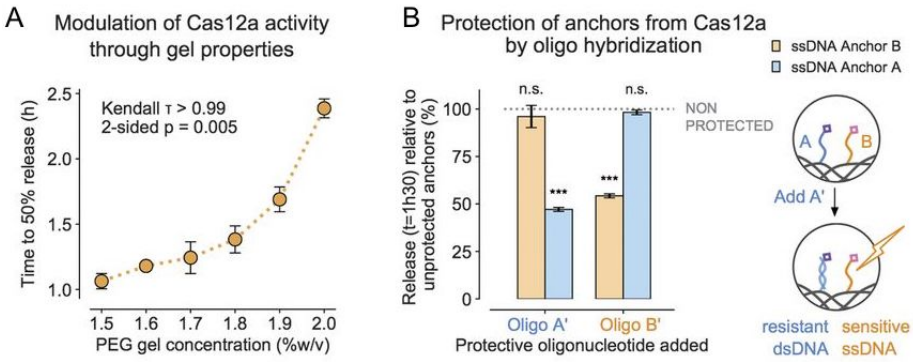

Figure 8 – Fine-tuning of cargo release by altering PEG hydrogel targets. (A) Cross-linking density of the PEG hydrogels modulates the release rate of the cargo by Cas12a. The correlation was analyzed using a Kendall rank test. (B) Prehybridization of the ssDNA linkers with a matching oligonucleotide selectively reduces the release rate of molecules anchored in the gel (observed at t = 1.5 hours). The means were compared with independent samples that were not preprotected with oligonucleotides (gray). Differences in the means of the test conditions and the unprotected controls were analyzed using a t test [Bonferroni-adjusted $\alpha = 0.0125$, P values: not significant (n.s.) $P > 0.05$, ***$P < 0.0001$]. Plots show mean ± SD for $n \geq 3$ replicates.

unprotected fluorophore was unaffected, the speed of release of the hybridized reporter was markedly reduced (Figure 8B).

2.2.3 Collateral Cas12a activity alters the large-scale mechanical properties of DNA hydrogels

The high catalytic efficiency of the dsDNA-activated Cas12a-gRNA complex ($k_{cat}/K_M \approx 1.7 \times 10^9$ $s^{-1}.M^{-1}$) [Chen *et al.*, 2018] makes it well suited for converting dsDNA signals into bulk material changes. To demonstrate this, we designed DNA cross-linked polyacrylamide (PA) hydrogels [Kahn *et al.*, 2015; Lin *et al.*, 2004] by separately incorporating two noncomplementary oligonucleotides into PA chains. We then cross-linked the PA-DNA precursors using an oligonucleotide strand that forms bridges between the PA-DNA chains. These cross-links contained single-stranded, AT-rich Cas12a collateral

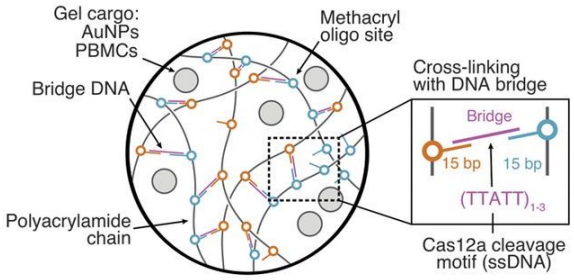

Figure 9 – ssDNA bridges lock DNA-functionalized PA chains into a 3D network

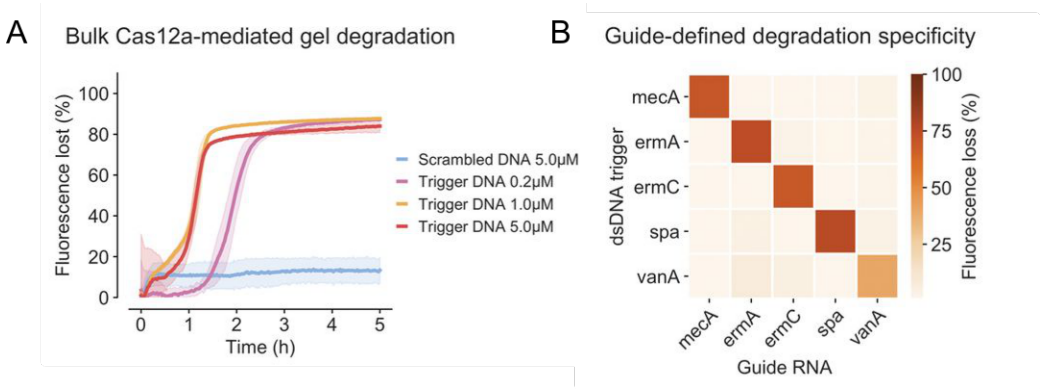

Figure 10 – Programmable Cas12a-gRNA mediated degradation of PA-DNA hydrogels. (A) Cas12a-mediated degradation of PA-DNA gels stained with EvaGreen intercalating DNA dye. (B) Degradation of gel with 25 combinations of gRNAs and dsDNA triggers and comparison of signals after 12 hours. Plots show mean ± SD for n ≥ 3 replicates.

cleavage sites (Figure 9); in these hydrogels, degradation of DNA cross-links physically disrupts the polymer networks [Wang *et al.*, 2018; Wei *et al.*, 2008], which we confirmed using nonspecific Mung Bean Nuclease (MBN) degradation assays.

The Cas12a-induced degradation of PA-based CRISPR gels was initially evaluated with a DNA-intercalating dye to label bridge sequences in PA-DNA gels and track gel integrity. The bridges were degraded upon exposure to gRNA-Cas12a and trigger dsDNA, as revealed by the dissipation of gel fluorescence at rates dependent on trigger

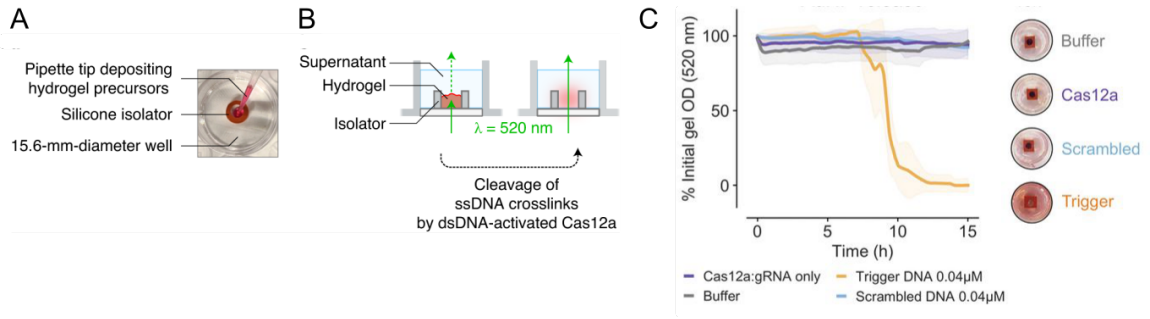

Figure 11 – Programmable release of AuNPs from PA-DNA hydrogels. (A) The PA-DNA gel precursor is cast in a circular silicone mold placed in the center of the microplate well. (B) Nanoparticles contained in the intact gel absorb light. Upon the detection of a trigger dsDNA by Cas12a, gel degradation causes the dispersion of the particles away from the optical path and into the surrounding solution, thereby causing a decrease in absorbance. (C) Release of AuNPs from 7% (w/v) PA-DNA gels using Cas12a collateral cleavage, tracked by measuring gel optical density. The Cas12a-gRNA and dsDNA trigger were encapsulated in the gel with the AuNPs (concentrations shown include supernatant volume). Plots show mean ± SD for n ≥ 3 replicates.

concentration (Figure 10A). Compared with experiments performed in solution, gel degradation appeared more robust to the introduction of sequence mismatches between the gRNA and dsDNA trigger. Using fluorescein isothiocyanate (FITC)-dextran particles physically entrapped in the hydrogel, we also visualized the degradation of millimeter-scale PA-DNA hydrogels.

Programmable degradation of PA-DNA hydrogels was assessed by testing 25 combinations of different gRNAs and dsDNA triggers. Consistent with the nondestructive cargo-release experiments (Figure 7), PA-DNA hydrogel degradation occurred only when the gRNA and dsDNA sequences were complementary (Figure 10B), demonstrating Cas12a-gRNA's ability to discriminate between inputs.

Though biomolecules can be tethered to materials through well-defined, single linkers (Figure 6), physical entrapment in a polymer matrix represents a more general strategy to control the release of larger payloads. We tested the release of nanoparticles

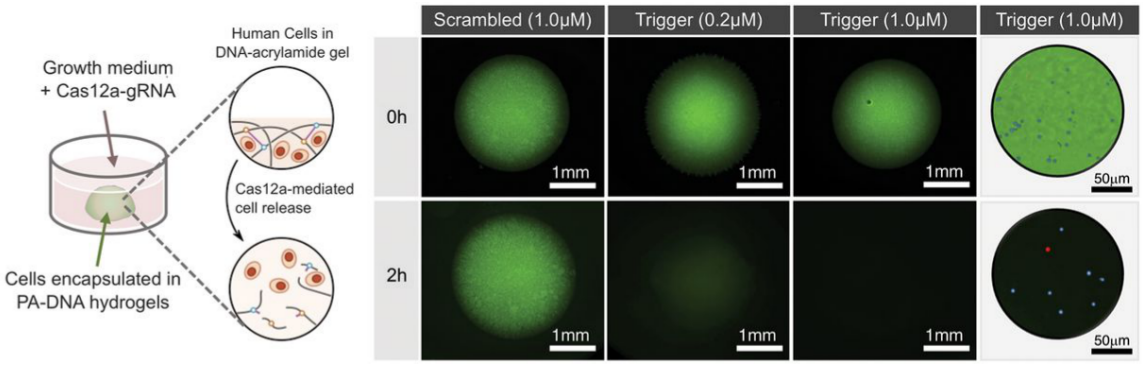

Figure 12 – Programmable release of primary cells from PA-DNA hydrogels. Sequence-specific degradation of PA-DNA gels leads to the release of encapsulated nonadherent PBMCs. Cells were stained before encapsulation using calcein acetoxymethyl ester (blue) and ethidium homodimer (red), and gels were labeled with a 6-FAM-functionalized ssDNA bridge.

(NPs) by encapsulating PEG-coated gold NPs (AuNPs) (Figures 9, 11A-B) in PA-DNA hydrogels. Loading gels with both Cas12a-gRNA and a dsDNA trigger led to total NP release through Cas12a activation and gel degradation, whereas gels loaded with a scrambled dsDNA trigger showed no significant release of AuNPs relative to a buffer-only background (Figure 11C). This was consistent with the disruption of the percolated network upon cross-link cleavage [Barker *et al.*, 2016; Zhu *et al.*, 2010].

The complex interactions between cells and surrounding materials have implications for tissue engineering and other therapeutic applications. We reasoned that Cas12a-gRNA would have the capacity to modify the extracellular matrix of cells encapsulated in DNA materials in response to predefined cues. We tested the reversible encapsulation of human primary peripheral blood mononuclear cells (PBMCs) in PA-DNA hydrogels by exposing the gels to activated gRNA-Cas12a. Complete gel degradation and cell release were observed within 2 hours in the presence of 1 μM dsDNA trigger (Figure 12), without compromising cell viability (as tested with a live/dead staining). Conversely, gels exposed to a scrambled dsDNA control remained intact in the same time frame. These

results demonstrate that NPs and live-cell payloads can be immobilized in biocompatible hydrogels and released upon addition of trigger dsDNA sequences without the need for hydrogel redesign to accommodate different input signals.

2.2.4 Conductive DNA-based materials act as Cas12a-actuated electronic fuses

We used Cas12a to modulate the attachment of a conductive DNA-based hydrogel to an electrode surface to act as an electrical fuse triggered by specific DNA sequences (Figure 13). A conductive, biologically responsive hydrogel may be desirable for a variety of sensing and diagnostic applications when the direct interface to electrical devices (such as analog circuits and microcontrollers) is required [Hajian *et al.*, 2019]. These conductive, self-assembled materials consisted of ssDNA networks cross-linked with carbon black-conductive NPs (CB-DNA gels). Carbon black (CB) is composed of spherical particles [Parant *et al.*, 2017] containing graphitic-like domains [Pawlyta *et al.*, 2015] and is widely used in industrial applications to impart electrical conductivity to polymers [Spahr *et al.*, 2016]; in this study, we used it as a conductive cross-linker in hydrogels. CB-DNA gels were synthesized through thermal melting of dsDNA followed by cooling in the presence of CB NPs. This leads to the strong, noncovalent association of the aromatic DNA nucleotides with nearby CB graphitic surfaces [Lu *et al.*, 2009] through hydrogen bonding and $\pi-\pi$ stacking interactions [Liu *et al.*, 2016; Manohar *et al.*, 2008; Xu *et al.*, 2010a]. In these hydrogels, DNA behaves as the main structural component, linking CB particles together to form a three-dimensional (3D) network [Xu *et al.*, 2010a,b].

We hypothesized that cleavage of the ssDNA at the electrode-material interface by Cas12a would disrupt the conductive path. To test this system, CB-DNA droplets were

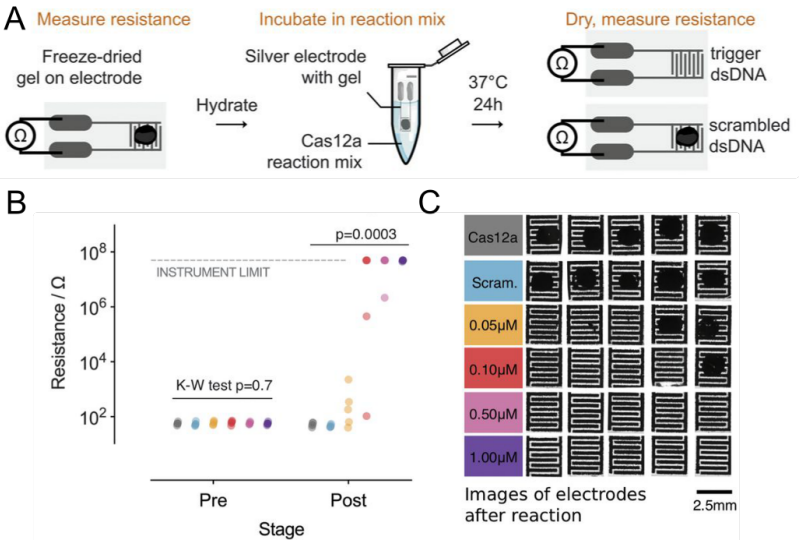

Figure 13 – CB-DNA hydrogels act as Cas12a-actuated electrical fuses. (A) Schematic of the experimental workflow. (B) Electrical resistance across silver interdigitated electrodes (IDEs) printed on polyethylene terephthalate, after removal from the reaction upon detachment of the CB-DNA gel or after 24 hours if no detachment occurred. Measurements before and after reaction were compared using a Kruskal-Wallis (K-W) test (before: $P = 0.7$, after: $P = 0.0003$) and Dunn's *post hoc* test (before: all > 0.99; after: $P < 0.05$ for both 1.0 μM and 0.5 μM versus controls, $P > 0.05$ otherwise). (C) Representative images of gels in the reaction mix. Scram., scrambled.

spotted onto printed interdigitated silver electrodes and lyophilized (Figure 13A). Before Cas12a-mediated degradation, lyophilized CB-DNA hydrogels showed conductivities comparable to that reported for graphene-DNA gels of similar compositions (≈4 mS/cm) [Xu *et al.*, 2010a]. After initial electrical testing, CB-DNA gels were incubated in a solution containing Cas12a-gRNA and dsDNA triggers. We visually monitored the CB-DNA hydrogels during Cas12a-mediated detachment, tested for conductivity (Figure 13B), and imaged the electrodes (Figure 13C) with increasing concentrations of dsDNA inputs. Cas12a-gRNA with 500 nM dsDNA trigger was able to completely detach 60% of the hydrogels from electrodes in 10 hours and 100% of hydrogels after 20 hours.

Incubation with a higher dsDNA trigger concentration (1 μM) led to CB-DNA detachment from all electrodes within 10 hours. Complete detachment resulted in an opening of the circuit across the electrode, whereas partial detachment of the CD-DNA hydrogels at lower dsDNA trigger concentrations led to intermediate conductivities (Figure 13B-C). Exposure of electrodes with CB-DNA gels to ssDNA-specific MBN resulted in a similar response, confirming that detachment was a consequence of Cas12a activation and ssDNA hydrolysis. This inexpensive CB-DNA gel formulation provides a direct link between dsDNA triggers and electrical outputs.

2.2.5 Cas12a-controlled hydrogel formation in a paper fluidic device enables diagnostic readouts

We used a tunable PA-DNA hydrogel to control the permeability and electrical readout of a paper-based microfluidic device (Figure 14). Paper-based technologies have shown promise for point-of-care diagnostics, as they are low cost, equipment-free, and easy to use [Pardee *et al.*, 2014, 2016]. Our device expands on the concept of microfluidic paper-based analytical devices (μPADs) that rely on the capacity of hydrogels to obstruct flow through porous channels [He *et al.*, 2015].

The layers of the device were folded to create a multilayered structure in which the hydrophilic regions are topologically aligned. Capillary-driven flow through the device terminated in a fifth layer where the output was measured. In this system, an intermediary layer contains PA-DNA gel precursors (Ps-X and Ps-Y) that, when mixed with ssDNA cross-linker, form a hydrogel in the paper channels [Badu-Tawiah *et al.*, 2015; Wei *et al.*, 2015]. The extent of gel formation, and therefore the rate of buffer flow, is dependent on the extent of degradation of the ssDNA gel cross-linker during a preincubation step (Figure 15). The activation of Cas12a can be confirmed by adding

a fluorescent ssDNA reporter during this step. By degrading the cross-linker by using Cas12a, we were able to couple the level of buffer flow to the concentration of dsDNA trigger added to a Cas12a reaction incubated for 4 hours.

When nonspecific dsDNA trigger is present during preincubation, ssDNA cross-linkers are not cleaved, allowing for hydrogel assembly in the microchannel (Figure 15). Conversely, in the presence of a specific dsDNA trigger, unimpeded flow can be visually detected by adding dyes to the μPAD channel. We found the rate of buffer flow through a μPAD to be inversely related to the concentration of an MRSA dsDNA trigger. Using this visual output, we were able to detect dsDNA concentrations down to 400 pM.

To optimize our CRISPR-μPAD for field diagnostic applications, we used reverse transcription (RT) to expand the range of detectable biomarkers to RNA and coupled the RT to an isothermal amplification step [recombinase polymerase amplification (RPA)] to improve the limit of detection. We used RT-RPA followed by a μPAD readout to detect synthetic Ebola genomic RNA [Magro *et al.*, 2017] down to 11 aM (Figure 16A), a sensitivity matching other state-of-the-art CRISPR-based diagnostics [Chen *et al.*, 2018; Gootenberg *et al.*, 2018, 2017]. This approach is promising for point-of-care diagnostics and has overall better performances in terms of sensitivity, portability, and cost than other molecular diagnostics.

Visual readouts of buffer flow are commonly used, yet they are difficult to couple to downstream hardware for data processing. To overcome this limitation, we modified the CRISPR-actuated fluidic system to read buffer flow as an electric signal: the microfluidic channel in the final layer was sandwiched between two electrodes and connected to an ohmmeter (Figures 14,15). Electrical conductivity between the electrodes relied on electrolytes provided by the flowing buffer and was directly correlated to the buffer penetration length in the μPAD channel [Fu *et al.*, 2010]. Using this approach, sub-nanomolar concentrations of dsDNA trigger were successfully detected at a 5-min end

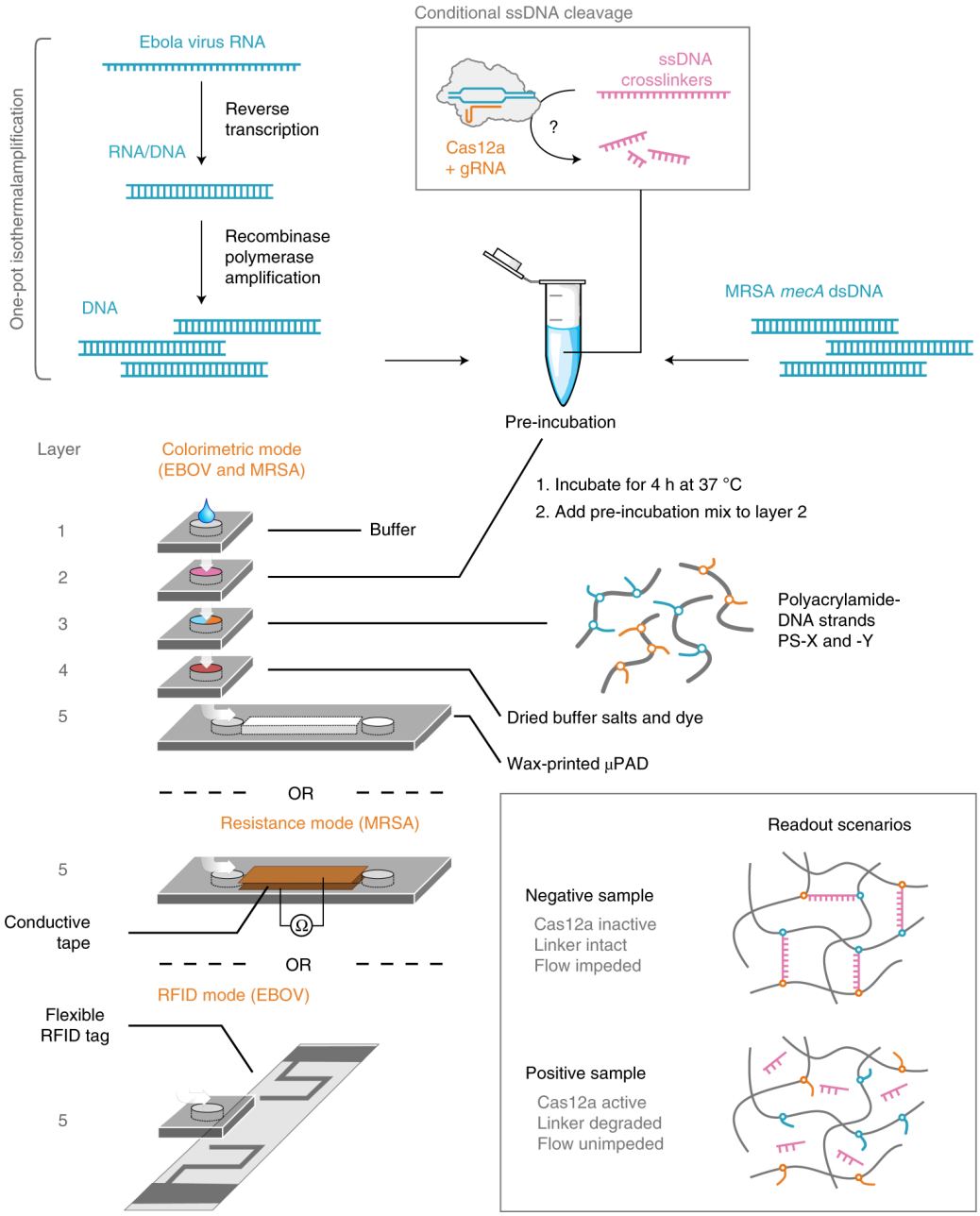

Figure 14 – [*Caption on next page*]

Figure 14 – [*Continued from previous page*] A schematic of the workflow for the detection of DNA and RNA targets using CRISPR-responsive materials as fluidic valves in paper devices. RNA targets are first converted into a DNA signal, because Cas12a is preferentially activated by dsDNA targets. Cas12a then probes input sequences for gRNA-matching dsDNA triggers and conditionally digests the ssDNA linkers. If sufficient degradation occurs, the linkers are unable to crosslink PA-DNA hydrogels in subsequent steps. In the folded fluidic device, buffer applied to the top layer (L1) brings the product of the pre-incubation (in L2) into contact with the PA-DNA macromers (in L3), thereby polymerizing a gel within the pores of the paper, which obstructs the channel. In the case of a successful Cas12a–gRNA complex activation by dsDNA, the digestion of ssDNA bridges prevents gel formation, and buffer proceeds through L4, where it dissolves salts and dyes before reaching the lateral flow channel in L5. There, the buffer can be detected by various means: visually, or electronically, either by measuring the increase in electrical conductance through the channel (analog signal) or by recording the short-circuiting of an RFID antenna (digital signal).

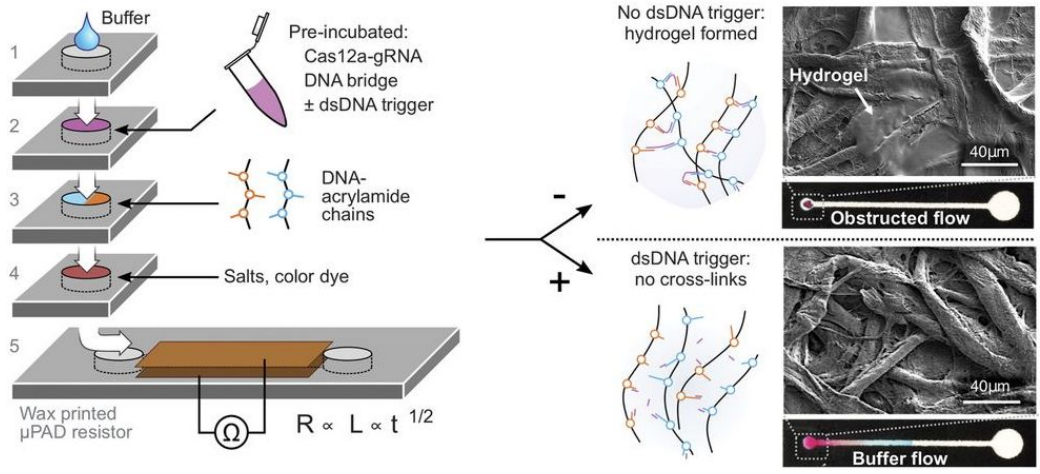

Figure 15 – Principle of operation of CRISPR-actuated µPADs. The stackable µPAD is designed for operation with CRISPR gels and electrical readout. Layers 1-4 contain hydrophilic regions that form a continuous channel on folding and feed into a lateral flow channel in layer 5. The channel in layer 5 was covered with conductive tape to measure conductivity as a function of buffer wicking. In the presence of target trigger, Cas12a cleaves the DNA linker, preventing hydrogel cross-linking in the channel and enabling flow. The inset shows SEM images of channels with (top) and without (bottom) cross-linked hydrogel.

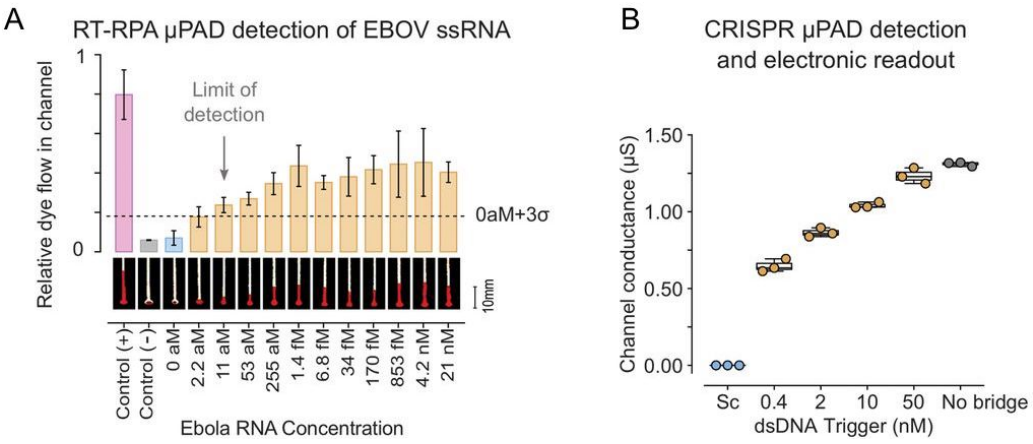

Figure 16 – Detection of pathogen nucleic acids using Cas12a-based μPADs. (A) End point measurements (t = 5 min) of the colorimetric-coupled RT-RPA μPAD hydrogel detection system for different concentrations of ssRNA Ebola virus (EBOV) input (mean ± SD, n = 3 μPADs). Representative images of μPAD channel flow are shown. The positive control corresponds to flow with no ssDNA bridging strand in the preincubation reaction, and the negative control corresponds to flow with an undigested ssDNA bridging strand. Student's t test P = 0.0057 for differences in the means of the 0- and 11-aM ssRNA samples. (B) End point measurements (5 min) of resistance across the channel for different concentrations of dsDNA MRSA trigger input after a 4-hour predigestion step. Sc = 50 nM scrambled dsDNA.

point, without DNA amplification, demonstrating the potential of the CRISPR μPAD for embedded sensor applications (Figure 16B). Nonspecific dsDNA trigger did not activate Cas12a, thus leaving the electrical circuit open. We were able to reduce the preincubation time required to observe a signal to 1 hour by tuning the properties of the acrylamide precursors.

The wireless, decentralized logging of individual clinical tests during infectious disease outbreaks could address challenges with record keeping and logistics. To integrate CRISPR-Cas reactions with electronic monitoring systems through hydrogel actuation, we incorporated a wireless radio-frequency identification (RFID) module into the μPAD. The original design was modified such that buffer flow would short-circuit an

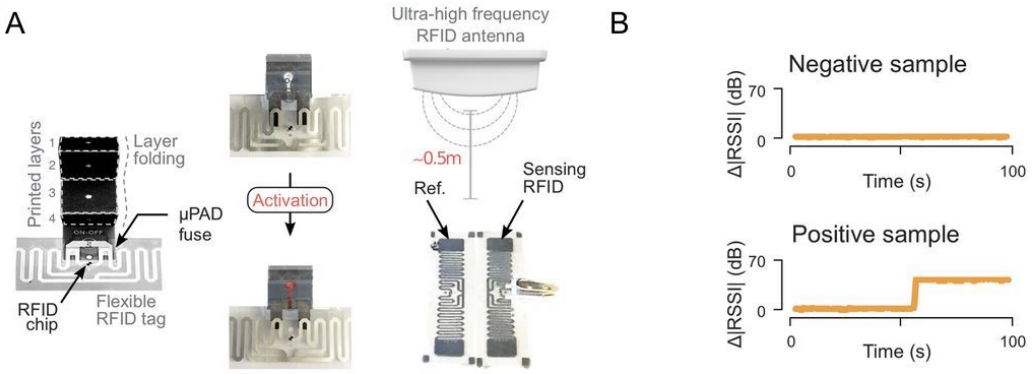

Figure 17 – (A) Schematic illustrating the integration of the paper-fluidic device with an RFID flexible tag. Cas12a activation in the preincubation step results in the short-circuiting of an interdigitated electrode arrangement in the loop RFID tag, thereby altering the received signal strength indicator (RSSI) compared with a reference tag (Ref.). An increase in absolute RSSI difference between the tags is indicative of Cas12a activation by a dsDNA trigger. (B) Representative signal traces for positive and negative results in the experimenter-blinded trial of the RFID μPAD device. Samples containing either 0 aM (negative) or 11 aM (positive) EBOV ssRNA trigger were amplified by RT-RPA, incubated with the ssDNA gel bridging strand and Cas12a-gRNA for 4 hours, and assayed on a μPAD-RFID device.

interdigitated silver electrode, thereby modulating the efficiency of signal transmission by a flexible RFID tag (Figure 17A). We then conducted an experimenter-blinded trial consisting of 12 samples (containing either 11 or 0 aM Ebola ssRNA amplified by RT-RPA) divided across three geographic locations. The experimenter preincubated the samples with Cas12a and Ebola-specific gRNA for 4 hours and then recorded the RFID-μPAD signals over the course of 2 min. Buffer flow through the μPAD in Ebola-positive samples caused short-circuiting of the RFID tag antenna, which was detected in real time as a change in the signal strength compared with an unmodified reference RFID tag (Figure 17B). All positive and negative samples were correctly assigned using the RFID-μPAD.

2.3 Discussion

We have demonstrated several strategies to interface biological signals with materials that combine the inherent programmability of Cas enzymes with hydrogel systems. These strategies offer control over a variety of complex behaviors and properties, including the release of molecules, NPs, and live cells, as well as bulk hydrogel degradation, electronic signal transduction, and microfluidic valve actuation. By exploiting the enzymatic properties of Cas12a, we have designed a platform that improves on hydrogel programmability and versatility, as only the gRNA molecule needs to be changed to allow hydrogel response to a user-defined DNA sequence. The catalytic activity of Cas12a improves sensitivity compared with DNA-responsive hydrogels requiring stochiometric amounts of DNA triggers for material activation. Finally, we demonstrate various forms of output that expand the capabilities of CRISPR-responsive materials and enhance existing biomaterial-based approaches for tissue engineering, molecular diagnostics, and bioelectronic interfaces with programmable readouts.

CHAPTER 3

Autocatalytic Base Editing for RNA-Responsive Translational Control

3.1 Background, Motivation

Developing robust tools to modulate the activity of genetic payloads in response to pre-defined cellular cues is a pressing challenge in biomedicine and biological engineering [Ilia & Del Vecchio, 2022]. Context-aware genetic circuits would have extensive applications in clinical settings as they could adjust gene expression during disease progression or facilitate precise, cell-specific targeting while minimizing off-target effects [Sedlmayer *et al.*, 2018; Wu *et al.*, 2019]. Notably, recent advances in transcriptomics have generated rich datasets that capture the molecular signatures of cell states and cell types [Tabula Sapiens Consortium, 2022], motivating efforts to harness this information for the selective, on-demand expression of therapeutic transgenes using novel sense-and-respond modules.

Transcripts of interest can be detected upon specific hybridization with engineered RNA molecules. As such, a key advantage of RNA as a sensor module is its ability to detect targets of interest by simple base pairing, thus facilitating the design of highly

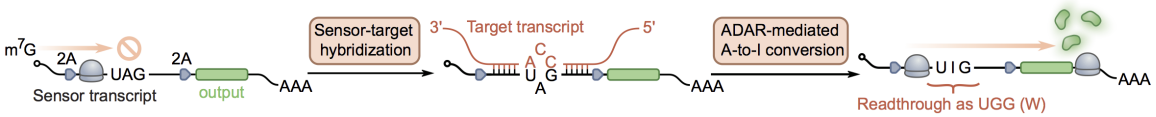

Figure 18 – Schematic presenting an overview of a basic ADAR-mediated translational switch. ADAR-based RNA-responsive sensors are activated by the specific hybridization of target transcripts, followed by the enzymatic deamination of the mismatched A in the central stop codon. The edited residue is interpreted as a G by the ribosome, allowing the translation of the downstream payload.

programmable tools that can be easily repurposed for new applications [English *et al.*, 2021; Schmidt & Smolke, 2019]. In particular, strand displacement has been explored as a strategy for the direct sensing of RNA triggers both in prokaryotes and eukaryotes [Green *et al.*, 2014; Siu & Chen, 2018]. Recently, the repertoire of transcript-sensing riboregulators was broadened to eukaryotes in a technology known as eToeholds, which relies on engineered mRNA internal ribosome entry sites (IRES) [Zhao *et al.*, 2021]. In eToeholds, inhibitory loops of IRES structures are disrupted upon hybridization with target RNAs, thereby restoring ribosome recruitment and enabling RNA-responsive translational control.

Most recently, three groups have independently described convergent approaches to design RNA-based sensors [Jiang *et al.*, 2022; Kaseniit *et al.*, 2022; Qian *et al.*, 2022]. In these preliminary reports, base editing by adenosine deaminases acting on RNAs (ADARs) couples the detection of an RNA trigger to the translation of a user-defined genetic payload (Figure 18). ADARs efficiently edit mismatched adenosines within imperfect double-stranded RNA (dsRNA) structures [Song *et al.*, 2020]. The specific hybridization of an engineered sensor transcript with an RNA target of interest therefore allows the conditional recruitment of these RNA-editing enzymes to pre-defined edit sites on the sensors. As adenosines and inosines are interpreted differently by the

translational machinery [Licht *et al.*, 2019], sensor transcript sequences can be designed such that an in-frame UAG stop codon is converted to UIG. As a result of the base editing, the amber codon becomes a sense (tryptophan) codon that does not block translation, leading to the expression of a protein payload encoded downstream of the edited codon (Figure 18). Through this process, ADAR enzymes convert the detection of an RNA target (via base pairing) into translational activation.

As ADARs are ubiquitous in metazoan cells, these sensors could be used in isolation to detect RNA molecules of interest (Figure 19,i). Although this design paradigm has been validated *in vivo* in neurons [Qian *et al.*, 2022], the nervous system is known to express high levels of ADAR [Uhlén *et al.*, 2015]. Therefore, circuits using endogenous levels of ADARs might not be as effective in other tissues. Overexpression of exogenous ADAR has been explored as a possible soltion to enhance the performance of this class of circuits in cells with a lower supply of endogenous ADAR [Jiang *et al.*, 2022; Kaseniit *et al.*, 2022] (Figure 19,ii). This, however, results in an increase in the number of transcriptional units, which may hinder the delivery of such a system to cells of interest. Additionally, wild-type ADAR enzymes are promiscuous, and their overexpression may lead to off-target effects. Together, these limitations highlight the need for compact, modular, and self-sufficient circuit designs that operate across various cell types irrespective of the cell's resource context.

Here, we describe a circuit topology that overcomes the constraints imposed by the endogenous ADAR supply without stymying delivery. We hypothesized that an autocatalytic circuit activated by ADAR expressed at endogenous levels could be engineered to express not only the desired protein output of interest, but also ADAR itself to edit additional sensors (Figure 19,iii). This led us to design DART VADAR (**D**etection and **A**mplification of **R**NA **T**riggers **v**ia **ADAR**), a circuit architecture with several key advantages over existing ADAR-based translational switches. At the RNA population

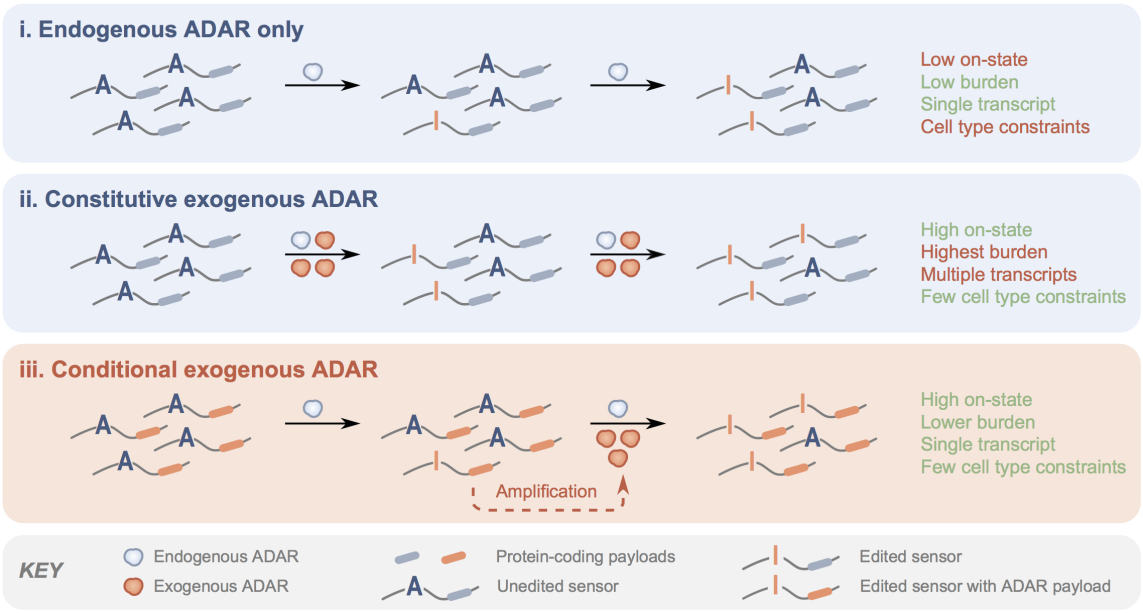

Figure 19 – Three different ways to design ADAR-based sensing circuits; these, as well as pros (in green) and cons (in orange) inherent in these designs, are summarized in panels i, ii, and iii. (i) ADAR-based RNA sensors can be designed such that there is no exogenous supplementation of ADAR.10 In such systems, the low levels of endogenous ADAR carry out editing of a subset of sensor molecules. (ii) Other implementations rely on constitutive overexpression of exogenous ADAR.9,11 Here, high levels of ADAR efficiently mediate editing of sensor molecules, but these systems are more difficult to deliver, and exogenous ADAR is overexpressed in all cells receiving the circuit, resulting in unnecessary consumption of cellular resources. (iii) A potential solution that builds on the advantages of the aforementioned approaches is based on conditional expression of exogenous ADAR. In such circuits, endogenous ADAR mediates editing in a small subpopulation of sensor molecules. This step prompts the translation of the circuit payload, which includes ADAR itself. After this initial editing step by endogenous ADAR, the system produces ADAR in order to increase the frequency of editing events and achieve higher dynamic range as a result of this amplification step. m7G: mRNA cap; 2A: selfcleaving 2A peptide; AAA: poly(A) tail.

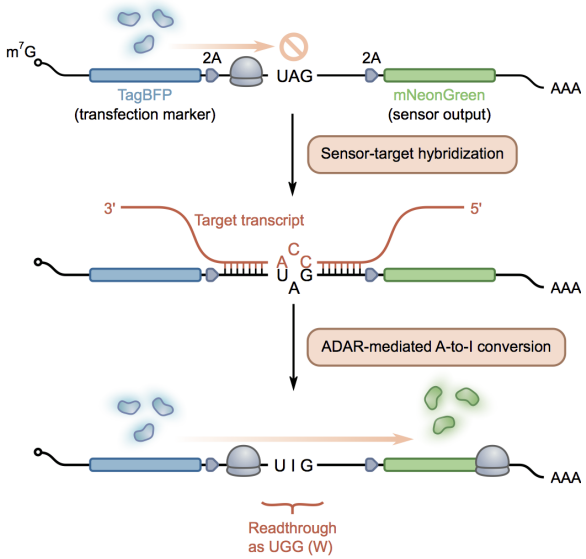

Figure 20 – First-generation ADAR-based RNA-responsive sensors, as have been previously reported, are activated by the specific hybridization of target transcripts, followed by the enzymatic deamination of the mismatched A in the central stop codon. We used this preliminary design as the basis for optimizing our DART VADAR sensors. Here, we included a TagBFP reporter sequence at the 5' end of the sensor transcript to account for plasmid dosage, and an mNeonGreen coding sequence downstream of the sensor sequence as the output. All the elements are insulated by self-cleaving 2A peptide sequences. m7G: mRNA cap; 2A: self-cleaving 2A peptide; AAA: poly(A) tail.

level, DART VADAR forms a positive feedback loop, amplifying the signal from endogenous ADAR on-demand. Additionally, this topology is compact and encoded in a single transcript.

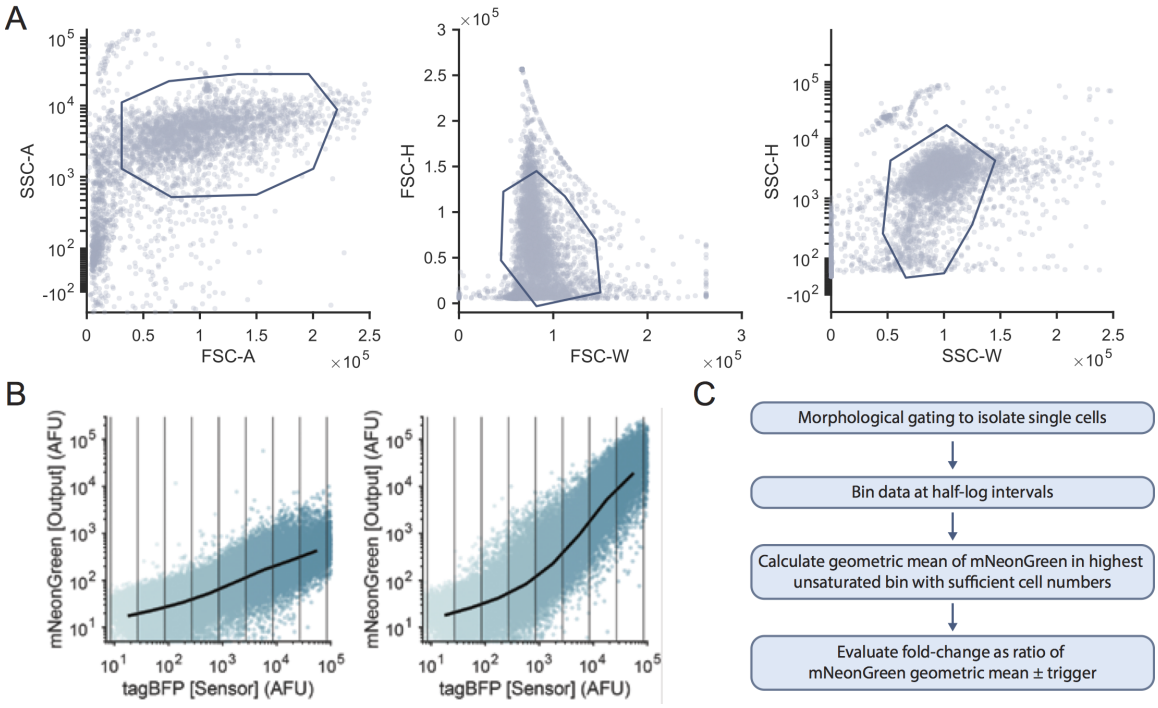

Figure 21 – Flow cytometry analysis pipeline. (A) Cells are gated based on forward- and side-scatter signals. (B) Data acquired via flow cytometry were binned at half-log intervals, excluding datapoints with saturated fluorescence measurements. This example presents representative data for sensor CCA60 in the absence (left) or presence (right) of secreted iRFP720 trigger. (C) The workflow presents an overview of our data processing strategy.

3.2 Results

3.2.1 Performance of ADAR-based riboregulators is dependent on enzyme availability

To lay the foundation for DART VADAR, we first sought to validate the hypothesis that ADAR availability is a limiting factor in RNA editing-based sensors. To do so, we designed and tested a basic ADAR-mediated sensor architecture (Figure 20). We used

flow cytometry to quantify the expression of the mNeonGreen payload across a panel of sensors targeting different regions of a trigger encoding the iRFP720 fluorescent protein (Figure 21). The sensors were designed to be complementary to sequences centered on CCA sites in the trigger, with the exception of the adenosine in the stop codon. Co-transfection of plasmids encoding the sensor variants and trigger in HEK293FT cells consistently resulted in higher payload expression compared to the sensor alone, across all CCA sites tested. We observed this trend for both short (51 bp) and longer (75 bp) sensor sequences (Figure 22); as the latter provided better performance, we proceeded with 75 bp sensor sequences for optimization of the basic ADAR-mediated sensor designs. In agreement with our hypothesis, supplying exogenous ADAR from an additional plasmid resulted in a marked increase in mNeonGreen output levels, suggesting that low endogenous levels of ADAR limit sensor performance (Figure 22). Of note, the p150 isoform of ADAR1 seemed to enhance output expression slightly more than the p110 isoform, yielding up to 8-fold activation — while weak, the difference seemed consistent across various preliminary experiments and prompted us to focus on this isoform.

The output activation in cells transfected with a sensor, ADAR p150, and a trigger was readily observable at the protein level via microscopy, whereas this was not the case for cells transfected with the sensor and trigger alone (Figure 23). To quantify this output at the mRNA level, we evaluated the editing efficiency of sensor transcripts via next-generation sequencing (Figure 24). We observed over 30% editing of the adenosine in the central UAG stop codon of sensor transcripts harvested from cells transfected with a sensor, ADAR p150, and trigger. Importantly, this editing was observed to a much lesser extent (about 3%) in cells receiving only the sensor and trigger plasmids, confirming that endogenous ADAR edits sensor transcripts but that its activity is insufficient to mediate efficient sensing. Additionally, we found that ADAR-mediated editing is specific:

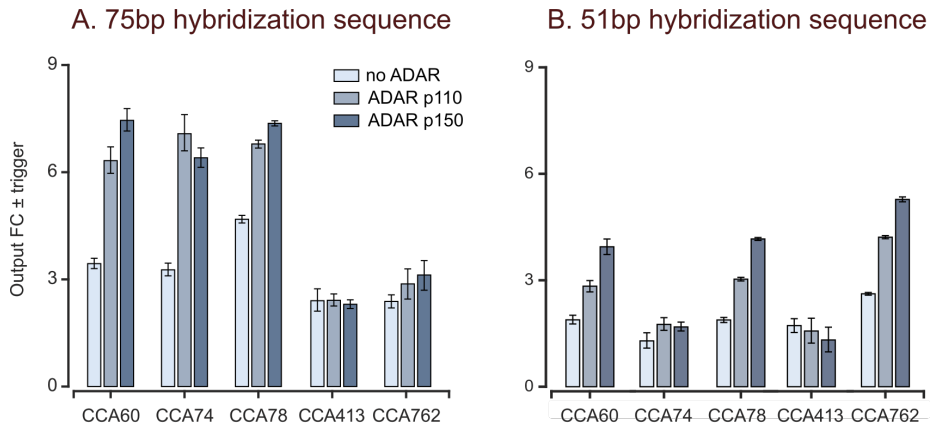

Figure 22 – Exogenous supplementation of ADAR improves sensor performance. Numbers following the CCAs indicate the nucleotide position of the central target triplet, using the start codon as position +1. The exogenous supplementation of ADAR improves the performance of sensors of both tested length, although 75bp variants (A) have slightly higher dynamic range compared to the shorter 51 bp sensors. Output fold-change (FC) is the ratio of the geometric mean of mNeonGreen expression in the presence and absence of trigger. Error bars represent 95% confidence intervals for the fold-change values.

we did not detect substantial off-target editing of other nearby adenosine residues in the sensor. These data, combined with considerations about deployment of such a technology for practical applications, prompted us to engineer sensors containing an autocatalytic feedback motif that does not require constitutive ADAR expression for sensitive detection of transcripts of interest.

We envisaged a self-amplifying circuit – DART VADAR – that consists of a sensor transcript containing four in-frame components insulated by self-cleaving 2A peptides (Figure 25). We cloned a transfection marker (TagBFP) upstream of the central UAG sensor to normalize for plasmid dosage. The sensor module contains a sequence complementary to a transcript of interest, with the exception of the adenosine in the central UAG stop codon. The conditionally expressed payload (the fluorescent reporter mNeonGreen) is encoded downstream of this stop codon. Further, an ADAR coding sequence is

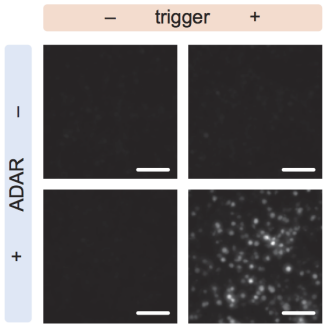

Figure 23 – Fluorescence microscopy of mNeonGreen illustrates the performance of the CCA60 sensor against iRFP720 in HEK293FT cells, 48 hr after transfection (Scale bar: 300 μm).

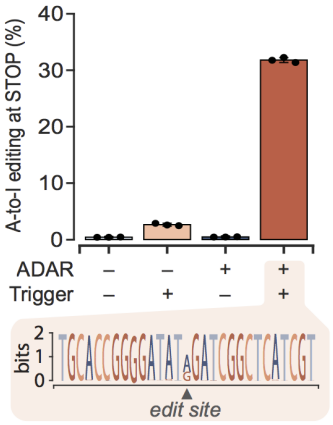

Figure 24 – High-throughput sequencing data confirms increased A-to-I editing of the CCA60 sensor in the presence of trigger in samples where exogenous ADAR p150 is supplied. The sequence logo demonstrates ADAR-mediated editing is specific to the central A in the UAG stop codon. Data collected on n=3 biological replicates.

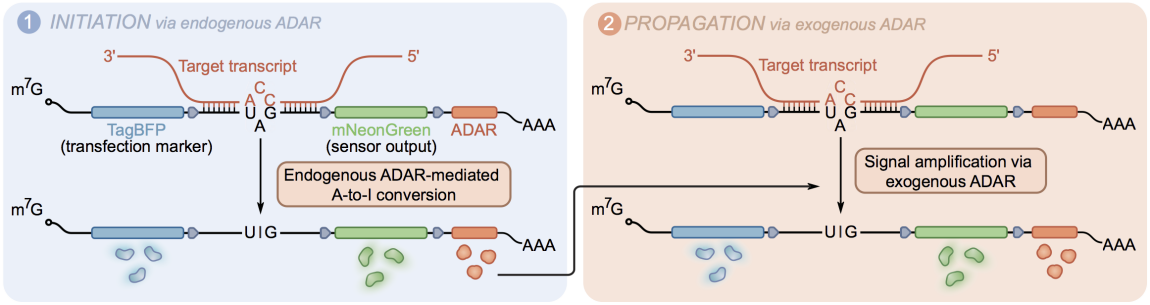

Figure 25 – DART VADAR relies on an initial editing step by endogenous ADAR enzymes, which is then amplified by the translation of additional ADAR.

linked to the sensor output via another 2A peptide. In this system, we expected that all cells transcribing the sensors would produce TagBFP, but only cells expressing the trigger RNA would also produce mNeonGreen and exogenous ADAR.

3.2.2 Identification of design rules for DART VADAR sensors

Considering the modular nature of our sensors, we first sought to independently optimize the trigger-sensor interface, starting with a simple topology in which ADAR is expressed constitutively from a separate transcript rather than conditionally from the sensor transcript. Accordingly, we set out to define general rules for the efficient targeting of RNA sequences of interest. We reasoned that since most gene-length RNA sequences harbor multiple CCA motifs, the question of which target sites should be prioritized for sensor engineering needs to be addressed. We hypothesized that the translational machinery may interfere with ADAR editing by disrupting dsRNA in coding sequences (Figure 26A) [Takyar *et al.*, 2005]. To test this hypothesis, we compared the performance of our validated sensors targeting trigger RNA sequences in three different contexts: (*a*) within the original protein coding sequence; (*b*) in a frame-shifted construct such that the target sites are part of the mRNA 3'UTR; and (*c*) in the coding sequence of a

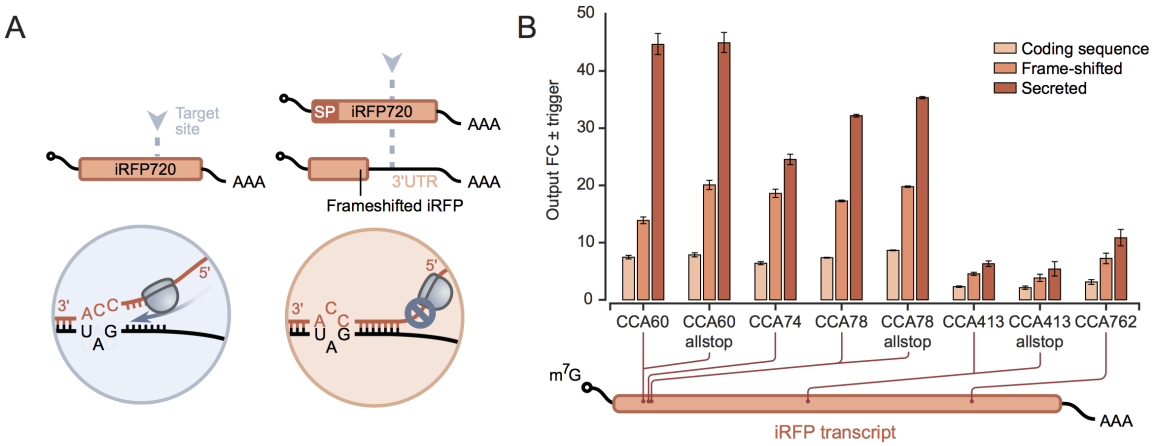

Figure 26 – (A) The performance of sensors (black) targeting a sequence in the coding sequence of a transcript is hypothesized to be diminished due to dehybridization by ribosomes translating the trigger sequence (orange). Given this, the performance of sensors designed against secreted proteins or 3'UTR sequences is expected to be enhanced as stalled and dissociated ribosomes are less likely to disrupt sensor-trigger hybridization. SP: signal peptide; UTR: untranslated region. (B) ADAR-based sensors yield higher dynamic range when designed to target the 3'UTRs of transcripts, or coding sequences of secreted proteins. "allstop" indicates that all the sites in the sensor aligning with CCA sites in the target were made into editable UAG codons (as opposed to only the central codon). Fold-change (FC) is the ratio of the geometric mean of mNeonGreen expression in the presence and absence of trigger. Error bars represent 95% confidence intervals for the fold-change values.

secreted version of the same protein (Figure 26A). Across all sensor sequences, targeting a secreted protein (and to a lesser extent a 3'UTR) yielded much higher activation levels than the same sites within the original protein-coding sequence – up to about 45-fold (Figure 26B). Since the ribosome pauses early during the translation of endoplasmic reticulum-targeted proteins [Shao & Hegde, 2011], our observations suggested that ribosome-free RNA sequences are generally better targets. This mechanistic insight explains why preliminary descriptions of ADAR-based sensors reported highly variable performance depending on the chosen target [Jiang *et al.*, 2022]. Of note, the importance of ribosome occupancy strongly suggests that ADAR-mediated editing is cytoplasmic. To

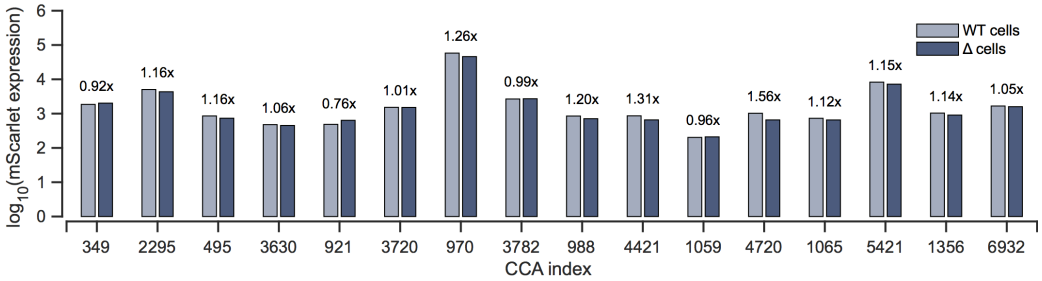

Figure 27 – Detecting nuclear transcripts. ADAR-mediated RNA-responsive sensors targeting the nuclear lncRNA MALAT1, as well as exogenous ADAR p150 and p110, were transiently transfected in two A549 cell lines. WT cells: parental cell line; Δ cells: MALAT1 knock-out derivative. The sensor output expression was comparable in both cell lines across 16 different sensors, suggesting that current ADAR-mediated RNA-responsive sensors function in the cytosol. Positions of CCA sites are numbered following McCown *et al.* [2019].

probe this further, we designed 16 sensors against the nuclear transcript MALAT1 [Wilusz *et al.*, 2012]. We did not observe output activation, even when we supplemented the transfection with the predominantly nuclear-localized p110 isoform of ADAR[1] [Poulsen *et al.*, 2001] (Figure 27). This supported and reinforced the hypothesis that in our system most editing events take place in the cytosol.

Next, we optimized the design of the modules that mediate autocatalysis in DART VADAR sensors. The natural ADAR isoforms are large (Figure 28), and therefore using one of these as the amplifier would undercut the delivery potential of our constructs. For instance, clinically approved adeno-associated viruses (AAVs) have a packaging limit of about 5 kilobases [Wu *et al.*, 2010]; the coding sequence of ADAR p150 would therefore expend over 70% of that capacity. Additionally, the dsRNA binding domains that mediate the recruitment of natural ADARs are promiscuous; supplying one of these

[1] Interestingly, our attempts to detect MALAT1 also proved unsuccessful using special sensors specifically designed for the detection of nuclear transcripts, and harboring nuclear localization elements: tandem SIRLOIN sequences [Lubelsky & Ulitsky, 2018], tandem KSHV PAN-ENE triple helices [Conrad & Steitz, 2005; Mitton-Fry *et al.*, 2010], or 6xMS2 hairpins recruiting a NES- and NLS-fused MCP nucleocytoplasmic shuttle protein [Woerner *et al.*, 2016].

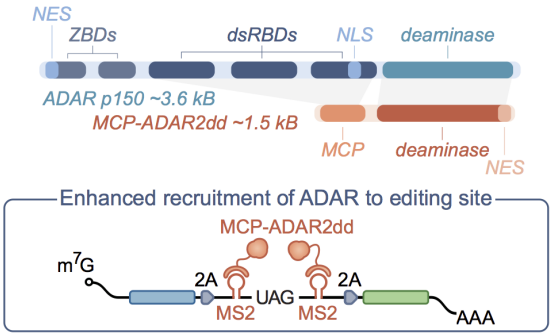

Figure 28 – MCP-ADAR2dd is a compact RNA base editor, and the MCP-MS2 binding system facilitates the specific recruitment of the enzyme to the sensor edit site. NES: nuclear export sequence; ZBDs: Z-DNA binding domains; dsRBDs: dsRNA-binding domains; NLS: nuclear localization signal; MCP: MS2 major coat protein; m7G: mRNA cap; 2A: self-cleaving 2A peptide; AAA: poly(A) tail.

ADARs in *trans* could therefore carry risks of off-target effects in bystander transcripts. Drawing inspiration from prior work focused on RNA-guided endogenous transcript editing [Katrekar *et al.*, 2019; Rauch *et al.*, 2019], we sought to overcome these limitations by substituting natural ADARs with an engineered ADAR variant that (*a*) contains only the ADAR catalytic domain necessary for RNA editing, and (*b*) could be recruited to the edit site to increase the frequency of editing events. To this end, we used a hyperactive, minimal version of ADAR2, namely MCP-ADAR2DD(E488Q)-NES (Figure 28) [Katrekar *et al.*, 2019] – hereafter referred to as MCP-ADAR. The MS2 bacteriophage major coat protein (MCP) specifically binds to a short MS2 RNA hairpin and replaces the promiscuous dsRNA-interacting domains of natural ADAR enzymes with a short, localized, and orthogonal RNA-binding moiety. We integrated MCP-ADAR in-frame in the sensor transcript and added two MS2 hairpins flanking the sensor UAG codon.

Upon testing the activity of sensors modified with MS2 hairpins in human cells, we observed that the constitutive expression of MCP-ADAR results in high sensor activation in the absence of trigger (Figure 29), thus reducing dynamic range. However, since

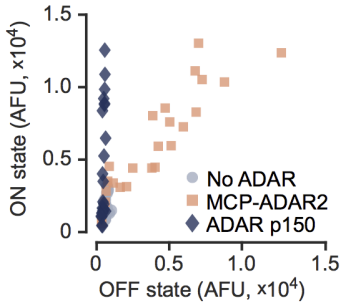

Figure 29 – Constitutive expression of MCP-ADAR results in leaky sensors. We tested the functionality of sensors containing MS2 hairpins without ADAR, with ADAR p150, or with MCP-ADAR2dd. The OFF and ON states correspond to mNeonGreen expression in the absence and presence of iRFP720 trigger mRNA, respectively.

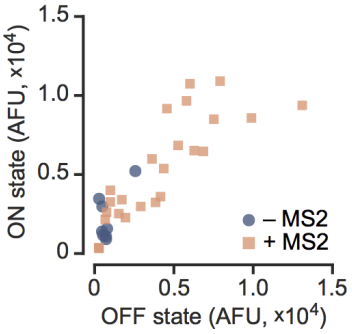

Figure 30 – MCP-ADAR specifically activates the translation of payloads encoded in sensor transcripts containing MS2 RNA hairpins.

leaky activation by MCP-ADAR was only observed in sensors harboring MS2 hairpins (Figure 30), we inferred that the basal activation by MCP-ADAR is unlikely to be indicative of promiscuous activity that would result in the editing of bystander transcripts. We therefore reasoned that MCP-ADAR would be a viable option for DART VADAR if we could enhance the dynamic range by reducing background editing.

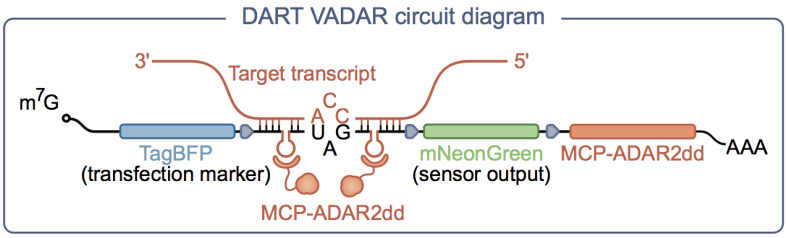

Figure 31 – Schematic illustrating the DART VADAR circuit design.

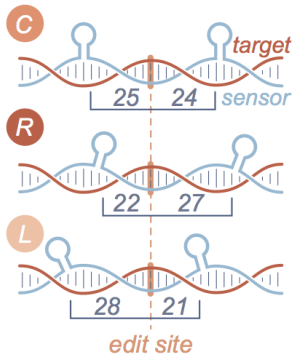

Figure 32 – We modified ADAR-based RNA-responsive sensors by adding two flanking MS2 hairpins upstream and downstream of the edit site in three configurations. Numeric annotations correspond to the number of base pairs between the edit site and MS2 hairpin. L, left; R, right; C, center.

3.2.3 Compact DART VADAR autocatalytic architecture boosts sensor performance

In DART VADAR sensors (Figure 31), MCP-ADAR is only expressed upon sensor activation. In the presence of trigger, these sensors rely on an initial editing step by endogenous ADARs, thereby yielding stop-less transcripts from which MCP-ADAR can be translated. In turn, MCP-ADAR can edit additional sensor molecules upon recruitment to the MS2 hairpins (integrated in the various ways shown in Figure 32), thus efficiently amplifying

the initial signal. This forms a positive feedback loop in which edited sensors give rise to the enzyme that further catalyzes this editing. We reasoned that this approach could capitalize on the low background editing by natural ADARs and the targeted and efficient editing by MCP-ADAR. Additionally, the system is highly compact and can be encoded in a single transcript, potentially facilitating its delivery to cells of interest.

To benchmark the performance of DART VADAR, we compared its activity (closed loop, CL) against an open-loop (OL) control in which MCP-ADAR is constitutively expressed in trans (Figure 33A). We observed that, across all tested prototypes, DART VADAR yielded low background activation without compromising maximal activity in the presence of the trigger (Figure 33B,C). As a result, the great majority of tested DART VADAR prototypes had increased dynamic range compared to the open-loop system, suggesting the broad applicability of this approach for improving sensor performance. A poly-transfection allowed us to de-correlate the amounts of sensors and triggers [Gam *et al.*, 2019], highlighting that the implementation of the feedback mechanism improves the transfer function for a given amount of sensor (Figure 33D). Together, these results suggest that the DART VADAR architecture is a promising approach to generate useful *in vivo* sense-and-respond modules.

3.2.4 DART VADAR sensors are specific and sensitive

To explore the utility of DART VADAR sensors for sensing cellular states, we tested their specificity and sensitivity in model mammalian cell lines. First, we investigated whether ADAR editing could be leveraged to discriminate between two RNA molecules with minimal differences. Somatic mutations are responsible for myriad complex diseases, ranging from cancer to cardiovascular and neurological conditions [Mustjoki & Young, 2021; Poduri *et al.*, 2013]. Therefore, the ability to discriminate healthy and diseased

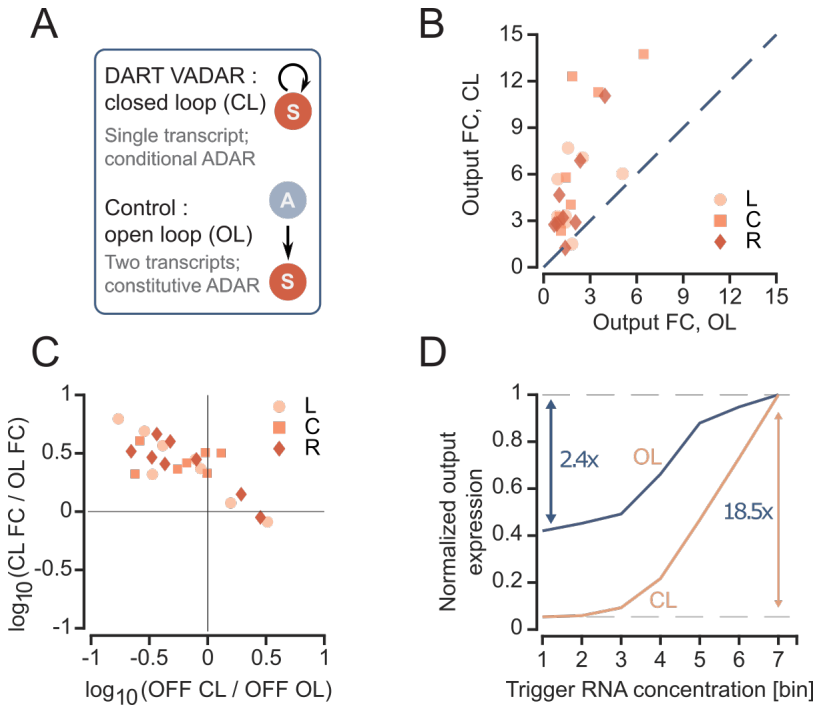

Figure 33 – Autocatalysis improves sensor performance. (A) As it forms a positive feedback loop, DART VADAR is a closed-loop (CL) system. To benchmark DART VADAR's performance, we constructed an open-loop (OL) control, in which ADAR is constitutively expressed and supplied in trans. (B) The fold-change (FC) of the geometric mean of mNeonGreen (output) expression levels is plotted for open-loop (OL) and closed-loop (CL) variants. Sensors represented by points that fall near the blue dashed diagonal line are minimally improved by autocatalysis, whereas points that fall above this line correspond to sensors that perform better with autocatalysis. (C) A comparison of the ratio of basal activity (x-axis) and fold-change (y-axis) in open- and closed-loop sensor variants demonstrates the performance boost provided by the autocatalytic architecture of DART VADAR. Closed-loop sensors with x-axis values below zero demonstrated a decrease in mNeonGreen expression in the absence of trigger, and closed-loop sensors with y-axis values above zero showed an increase in dynamic range. (D) Open- and closed-loop sensors have different transfer curves for a given sensor expression level. The iRFP720 bin #1 corresponds to a "no-trigger" condition. For each variant, mNeonGreen expression is normalized to the maximal sensor activation (bin #7).

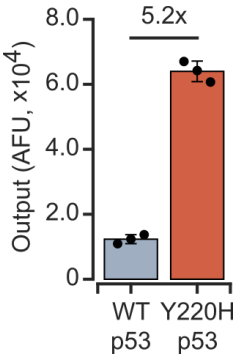

Figure 34 – DART VADAR sensors can be designed to specifically activate in response to a point mutation (n = 3 biological replicates). WT: wild-type p53 mRNA; Y220H: mutant p53 mRNA.

cells in mosaic tissues would be of great interest for precision therapeutics. We therefore tested whether a DART VADAR sensor targeted towards a point mutation of interest could specifically trigger translation in cells expressing a disease biomarker.

As a case study, we focused on a single-base mutation in the human p53 tumor suppressor gene (c.658T>C), which results in a Y220H substitution that is known to destabilize the DNA binding domain of p53, making it a driver of breast, lung, and liver cancers [Bauer *et al.*, 2020; COSMIC database, 2021]. We transfected HEK293FT cells with a DART VADAR sensor specifically designed to detect the p53 mutant, alongside plasmids expressing either the wild-type or Y220H mutant p53 gene. We observed a 5-fold activation in the reporter gene downstream of the sensor in cells expressing p53-Y220H, highlighting the specificity of DART VADAR sensors (Figure 34).

We next investigated whether DART VADAR could be used to discriminate closely related cell types based on differentially expressed endogenous genes. To date, ADAR-based sensors have only been tested *in vivo* without ADAR supplementation in the cerebral cortex [Qian *et al.*, 2022] or the liver [Jiang *et al.*, 2022]; both tissues are however known to express high basal levels of ADAR isoforms (Figure 35) [Uhlén

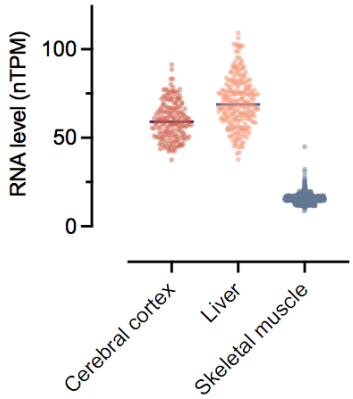

Figure 35 – Human tissues differ in endogenous ADAR expression levels. Transcriptomic data was generated by the Genotype-Tissue Expression (GTEx) project and retrieved through the Human Protein Atlas server. Each data point corresponds to mean values of different samples from each tissue. Plots represent n> 200 individuals per tissue. nTPM: normalized protein-coding transcripts per million.

et al., 2015], which facilitates the activation of sensors. We sought to investigate the performance of DART VADAR in a more challenging context: we chose a model system representative of the skeletal muscle in which ADAR expression levels are low. We reasoned that if our sensors are able to initiate the autocatalytic cascade despite the limited availability of endogenous ADAR, it would be compelling evidence that the system can be functional in most tissues. We focused our study on the C2C12 murine myoblast cell line, a well-described model of cell differentiation (Figure 36A). When they reach confluency, and particularly in serum-restricted conditions, C2C12 cells differentiate to form functional myotubes. Alternatively, upon exposure to bone morphogenetic protein-2 (BMP-2), the cells are biased to differentiate towards an osteoblastic lineage [Katagiri *et al.*, 1994]. We designed sensors targeting RNA markers of both cell fates, namely the 3' UTRs of mRNAs encoding myogenin and slow-twitch myosin heavy chain I (two proteins expressed during myogenesis), and the coding sequence of alkaline

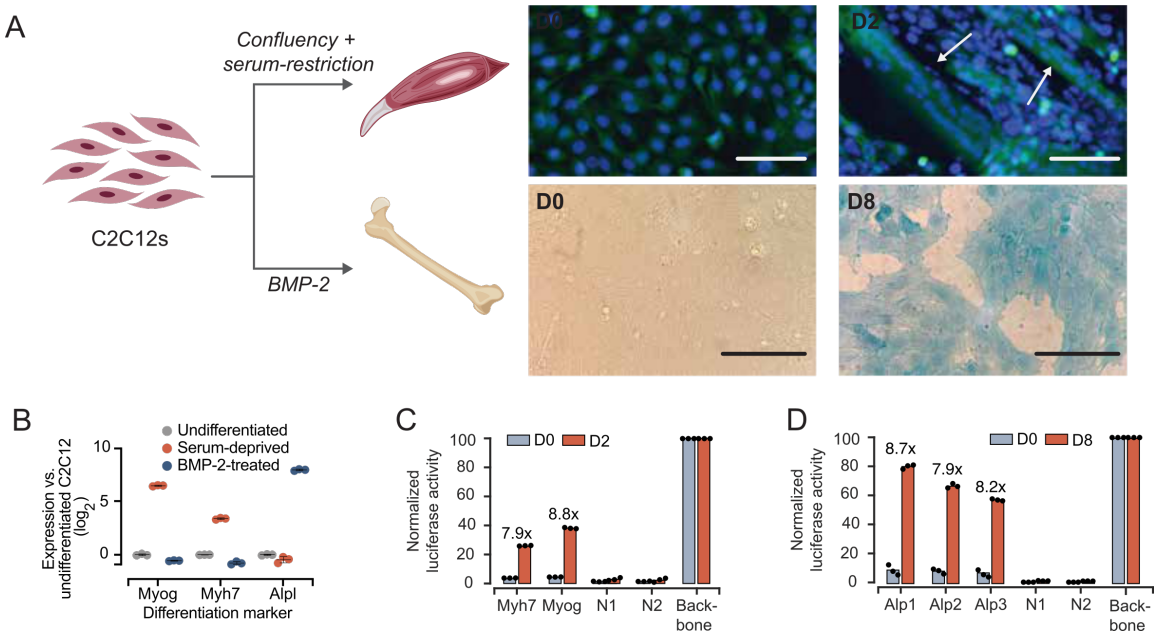

Figure 36 – Detection of endogenous transcripts during cell differentiation. (A) C2C12 cell differentiation can be steered towards the myoblastic or the osteoblastic lineage. Top right: a Hoechst 33342 (DNA, blue) and CFSE (whole cells, green) staining demonstrates the presence of multinucleated syncytia (arrows) two days after switching C2C12 cells to the differentiation-inducing medium. Bottom right: a colorimetric BCIP/NBT assay detects alkaline phosphatase activity in C2C12 cells treated with BMP-2 for 8 days. (Scale bars: 150 μm) (B) RT-qPCR gene expression analysis highlights muscle and bone lineage-specific markers in undifferentiated and differentiated C2C12 cells. Bars represent mean and standard deviation measured on n=3 technical replicates. (C) Sensors targeting endogenous myosin heavy chain (Myh7) and myogenin (Myog) mRNAs are specifically activated between days 0 and 2 post-induction of differentiation. Backbone: stop-less sensor RNA, constitutively active; N1, N2: sensors for osteoblastic differentiation (negative controls). (D) Three sensors targeting endogenous alkaline phosphatase (ALP) mRNA are detected on days 0 and 8 post-treatment with BMP-2. Backbone: stop-less sensor RNA, constitutively active; N1, N2: sensors for myogenic differentiation (negative controls).

phosphatase (a bone-mineralizing enzyme). We then differentiated C2C12 cells, which we confirmed phenotypically either by the presence of multinucleated syncytia indicative of early myotube formation (eventually forming functional contractile units), or by the detection of strong alkaline phosphatase activity (Figure 36A). Reverse transcription followed by quantitative PCR (RT-qPCR) also confirmed the expected increase in the expression of the target mRNAs (Figure 36B), indicative of the transcriptional changes that drive differentiation. We observed that our DART VADAR constructs expressed their payload (Nanoluc luciferase) as a response: sensors targeting the myogenin and myosin mRNAs were activated in myotubes (Figure 36C), while alkaline phosphatase-targeting sensors were strongly activated in BMP-2-induced osteoblasts (Figure 36D) – up to 80% of the maximum level defined by a stop-less control. These observations demonstrate that DART VADAR constructs are sensitive enough to drive high levels of expression of user-defined payloads in response to endogenous levels of natural transcripts, making them well suited to sense and respond to transcriptional changes across both cell types and cell states.

3.3 Discussion

In this chapter, we presented DART VADAR, a sensitive, programmable, modular, and compact RNA sense-and-respond circuit. Hybridization of a DART VADAR sensor with a user-defined trigger transcript initiates RNA editing of a premature stop codon, driving the translation of the downstream payload sequences. We validated a secondary payload in the form of a hyperactive, minimal version of ADAR2 and targeted it to the edit site via the MS2 RNA hairpin-coat protein interaction, resulting in an autocatalytic positive feedback loop. This configuration relies on endogenous ADAR to elicit the initial response with a high degree of specificity. We demonstrated that by using autocatalysis,

we attenuated the circuit background and enhanced the output dynamic range by close to eight-fold relative to an open-loop configuration, while reducing the overall number of components and genetic footprint of the technology. The resulting circuit is able to detect minimal differences between RNA molecules and interpret endogenous signals to control transgene expression across different cell states.

While we have defined general rules for targeting user-defined RNA targets, the choice of a target site for *in vivo* applications might involve additional considerations beyond editing efficiency. Machine learning would be a straightforward way to optimize target detection, as has been done for toehold switches [Angenent-Mari *et al.*, 2020; Valeri *et al.*, 2020], but the design of editing-based sensors might involve unique trade-offs between efficacy and safety. Sensor sequences encode translated peptides, the exact sequences of which are defined by the target RNA sites; different sensors targeting a given RNA sequence will therefore produce different peptides, which might vary in their immunogenicity. We expect that recent computational advances in the prediction of peptide immunogenicity could be leveraged to further refine the prediction of optimal target sites [Peters *et al.*, 2020], thereby guiding the design of therapeutically relevant DART VADAR sensors.

Our work expands the application space of editing-based riboregulators: the auto-catalytic feedback implementation features a size of less than 5 kb (including promoter and terminator), making it amenable for delivery in clinically relevant vectors [Wu *et al.*, 2010]. Importantly, as ADAR enzymes are endogenously expressed in most human tissues [Uhlén *et al.*, 2015], we expect most cells to be able to trigger autocatalysis when provided with DART VADAR sensors. We envision that DART VADAR could lay the foundation for easy-to-deliver smart RNA-based therapeutics.

CHAPTER 4

Concluding remarks

4.1 A common thread across nucleic acid-based tools

Here we developed two technologies that use RNAs as sensors for nucleic acids of interest, and proteins as catalytic intermediates to generate a diverse range of downstream responses *in vivo* and *in vitro*, from biochemical activities to electronic signals. While operating in very different contexts and at different scales, the two approaches developed here have strong similarities, summarized in Table 1; these illustrate broad design principles for nucleic acid-based sensor-actuators.

While in the case of CRISPR-actuated materials, Cas12a acts on bystander molecules, endogenous and engineered ADAR variants modify the sensor molecule itself; in both examples though, the functional output is decoupled from the sensing moiety. The independent reprogramming of the input and the output is a generalizable strategy to facilitate the transfer of the actuators to new functional contexts [English *et al.*, 2021]. This ensures that newer molecular tools can adapt to user-defined constraints, seamlessly integrating synthetic tools in real-life environments.

Table 1 – Similarities between CRISPR actuation of materials and ADAR-based sensors

Feature	CRISPR materials	DART VADAR
Analyte	Nucleic acid (DNA)	Nucleic acid (RNA)
Target programmability	User-defined target with a PAM	User-defined target cytosolic RNA
Sensing modality	Pairing with a designer gRNA	Pairing with a designer mRNA
Detection of hybridization	Through a protein (Cas12a)	Through a protein (ADAR1)
Interpreter protein activity	Permanent nucleic acid modification (hydrolysis)	Permanent nucleic acid modification (base deamination)
Downstream amplification	Activated Cas12a cuts multiple ssDNA molecules	Stop codon suppression leads to multiple downstream translation events
Output programmability	Various downstream responses defined by material chemistry	Various downstream responses defined by sensor ORFs

4.2 Challenges and opportunities for a new generation of nucleic acid-based tools

4.2.1 Harnessing the power of computational methods

Nucleic acid-based sensors greatly simplify the problem of probe design, as predicting base pairing is straightforward compared for example to protein-protein interaction predictions. Yet, as illustrated throughout this thesis (Figures 7, 10B, 22 and 26) sensors targeting different sequences often lead to noticeably different performances, even when they are designed following the same rules and tested in similar conditions. This is true across most sensing modalities, including CRISPR and ADAR-based tools. In our hands, the performance of a sensor molecule cannot be predicted easily from simple metrics such as the GC content, which is in agreement with previous observations. Recent efforts to identify nucleic acid effectors with little to no target sequence constraints highlight the need to better understand which sequences make for "good" and "poor"

targets [Gao *et al.*, 2017; Konermann *et al.*, 2018; Walton *et al.*, 2020]. Machine learning algorithms provide a powerful way to test new variants *in silico*, and infer not only their on-target performance but also other metrics of interest such as their propensity for nonspecific activation. While black-box models can help predict the performance of nucleic acid-based tools, efforts to create more interpretable models help guide the design of reliable molecular sensors and actuators [Angenent-Mari *et al.*, 2019; Valeri *et al.*, 2020].

The past few years have witnessed major progress in the field of *de novo* protein structure prediction [Jumper *et al.*, 2021], while parallel technologies in the realm of nucleic acids are still fledgling. In parallel, recent efforts to predict the activity of RNA actuators show that computational models benefit from the addition of even simple structural information in training data [Wei *et al.*, 2022]. We are confident that as we gain a better understanding of RNA structural rules and dynamics, this information will drive the development of powerful *in silico* tools facilitating the design of nucleic acid-based tools for operation in new contexts.

4.2.2 Original chemistries for novel actuators

The examples developed here illustrate how various chemical activities (DNA cleavage, RNA editing) can be harnessed to trigger specific responses in response to nucleic acid signals. The range of possible applications of nucleic acid sensor-actuators is limited by the types of signals that can be interpreted (that is, what can be used as an input) as well as by the type of outputs that can be generated, which depends mostly on how signal transduction operates at a molecular level.

Beyond using DNA and RNA as triggers, other biological molecules can interact with RNAs and could be used as signals of interest. In particular, aptamers can bind to

proteins and small molecules; inspired by natural riboregulators, engineers have started using those to control RNA activity in the context of mRNAs [Bayer & Smolke, 2005] and CRISPR effectors [Kundert *et al.*, 2019]. Generating aptamers is however more challenging than predicting Watson-Crick pairing; we see great potential in efforts to develop high-throughput approaches to diversify ligand-binding nucleic acids [Townshend *et al.*, 2021].

Alternative chemical activities could also help create more diverse biological responses for nucleic acid-based actuators. For example, DART VADAR sensors described here are engineered to edit out an amber codon, but other RNA-editing enzymes like cytidine deaminases could, for example, create nonsense mutations and generate alternative responses to the signal of interest [Huang *et al.*, 2020].

We envision that approaches combining bioprospection, directed evolution and computational design will yield many molecular domains that significantly expand the range of inputs and outputs compatible with nucleic acid-based regulators. However, we anticipate that embedding these in a truly modular and decoupled architecture will be a key challenge for the widespread adoption of these new molecular tools.

Appendix:
Experimental methods

Methods for CRISPR-actuated materials

Note: The following methods are reproduced (with permission from AAAS) from English *et al.* [2019], and are described step by step in even greater detail in Gayet *et al.* [2020].

DNA and RNA sequences – For this study, we obtained all DNA oligonucleotides from Integrated DNA Technologies. Cas12a gRNAs were produced by *in vitro* transcription using an HiScribe T7 transcription kit (NEB) and oligonucleotide templates (Figure 37); gRNAs were subsequently purified using an RNA Clean & Concentrator kit (Zymo Research). The sequences used are provided in Tables 2, 3, and 4.

In vitro Cas12a reagent validation with ssDNA – We measured collateral degradation of non-target ssDNA upon Cas12a in solution by mixing trigger dsDNA with Cas12a-gRNA complex and using a quenched, fluorescently labeled reporter. We assembled the Cas12a-gRNA complex by incubating 200 nM Cas12a with 250 nM gRNA in 1X NEB 2.1 buffer at 37^{o}C for 10 min. To initiate the reaction, we mixed the Cas12a complexes with dsDNA triggers and a quenched, ssDNA fluorescently labeled reporter [FQ reporter: 5'(6FAM)-TTATT-(Iowa Black FQ)3'] to final concentrations of 50 nM Cas12a, 62.5 nM gRNA, 750 nM FQ reporter and dsDNA triggers in NEB 2.1 buffer. We incubated

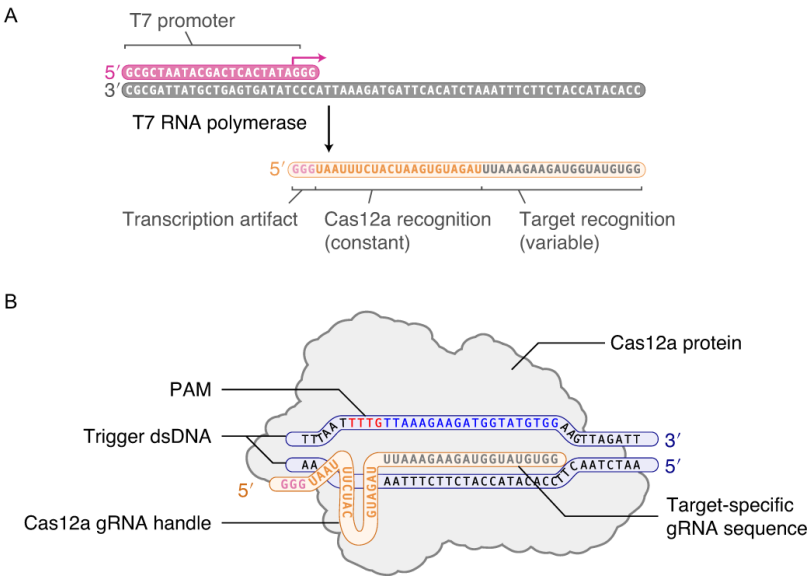

Figure 37 – Design and synthesis of guide RNA molecules. (A) The IVT of gRNAs is performed by hybridizing an adaptor (pink) with a template oligonucleotide (gray) upstream of the guide sequence. This generates a double-stranded promoter that efficiently recruits the T7 RNA polymerase. (B) In the Cas12a ribonucleoprotein, the target-specific gRNA sequence (orange) hybridizes with the DNA target molecule. The 'TTTG' PAM (pink) is immediately 5' of the sequence that matches the guide sequence. The sequences shown in both panels correspond to those used to activate Cas12a in response to dsDNA fragments (blue) derived from the *Staphylococcus aureus mecA* gene.

reactions (3 μL, 384-well microplate) in a fluorescence plate reader (Biotek NEO HTS) for 120 min at 37^{o}C. Fluorescence readings were recorded every 2 min (Ex: 485 nm; Em: 535 nm).

Synthesis and digestion of PEG hydrogels with reporter DNA – With the exception of explicitly mentioned protocol variations, we produced DNA-decorated PEG hydrogels as follows:

– *DNA-thiol reduction.* We mixed 0.5 μL of tris(2-carboxyethyl)phosphine (TCEP, 0.5M solution, pH7, Millipore Sigma) with 10 μL of double-functionalized reporter

Table 2 – Cas12a gRNAs

gRNA	Sequence (5' to 3')
mecA	GGGUAAUUUCUACUAAGUGUAGAUUUAAAGAAGAUGGUAUGUGG
ermA	GGGUAAUUUCUACUAAGUGUAGAUCUAUUAAUGGUGGAGAUGGA
ermC	GGGUAAUUUCUACUAAGUGUAGAUAAUCGUCAAUUCCUGCAUGU
spa	GGGUAAUUUCUACUAAGUGUAGAUUGGUAAUGCUUGAGCUUUGU
vanA	GGGUAAUUUCUACUAAGUGUAGAUGUAUUCAUCAGGAAGUCGAG
ZEBOV	GGGUAAUUUCUACUAAGUGUAGAUGGUGCUGGAGGAACUGUUAA

oligonucleotides (5'-C6-Thiol,3'-Cy3 oligos, custom-synthesized, HPLC purified, Integrated DNA Technologies) resuspended at 500 μM in water. We then incubated the solution for 3.5 h in the dark at room temperature to reduce the disulfide groups on the DNA.

– *DNA grafting on PEG precursors.* We prepared a fresh stock of 8-arm vinyl sulfone-activated PEG (PEG-VS, MW10 kDa, JenKem Technology) by resuspending aliquots of PEG-VS powder at 4% w/v (assuming a PEG density of 1.1) in 1M triethanolamine (pH of 8). We added 125 μL of PEG-VS stock to the reduced DNA solution and incubated in the dark at room temperature for about 18 h, to allow the base-catalyzed Michael addition of thiols on the vinyl sulfones. We included a large amount of PEG reactive ends (800-fold relative to DNA thiols) to capture the majority of DNA molecules and guarantee the availability of extra vinyl sulfone moieties in the subsequent polymerization step.

– *Hydrogel polymerization.* We prepared a fresh stock of 4-arm thiol-activated PEG (PEG-SH, MW10kDa, JenKem Technology) by resuspending aliquots of PEG-SH powder at 4% w/v (assuming a PEG density of 1.1) in water. On ice, we added 125 μL of PEG-SH stock to the DNA/PEG-VS solution and 239.5 μL of water to reach a volume of 500 μL. The final gel contained 2% w/v PEG (1% w/v of each precursor), had a cross-linking density of 4 mM and harbored 10 μM immobilized ssDNA. The gel precursor remained

Table 3 – Cas12a bacterial and viral targets

Name	Sequence (5' to 3')	Notes
Scrambled dsDNA trigger	TAGTAGTGATTATGTTAGAT AGTGAATAGGTTTAATGTAT	Permutation of the mecA trigger.
mecA dsDNA trigger	TTTAATTTTGTTAAAGAAGA TGGTATGTGGAAGTTAGATT	Trigger for mecA gRNA-primed Cas12a
mecA -1 mismatch	TTTAATTTTGTTAAAGAAGA TGTTATGTGGAAGTTAGATT	Single substitution variant of mecA
mecA -3 mismatches	TTTAATTTTGTTAAATAAGA TGTTATGTAGAAGTTAGATT	Triple substitution variant of mecA
ermA dsDNA trigger	GCTTTGGGTTTACTATTAAT GGTGGAGATGGATATAAAAA	Trigger for mecA gRNA-primed Cas12a
ermC dsDNA trigger	TAATATTGTTTAAATCGTCA ATTCCTGCATGTTTTAAGGA	Trigger for mecA gRNA-primed Cas12a
spa dsDNA trigger	TTCACCAGTTTCTGGTAATG CTTGAGCTTTGTTAGCATCT	Trigger for mecA gRNA-primed Cas12a
vanA dsDNA trigger	ACGGAATCTTTCGTATTCATC AGGAAGTCGAGCCGGAAAA	Trigger for mecA gRNA-primed Cas12a
ZEBOV VP30 dsDNA	GTGCGCGTTCCTACTGTATTTCATAA GAAGAGAGTTGAACCATTAACAGTT CCTCCAGCACCTAAAGACATATGTC CGACCTTGAAAAAAGGATTTTTGTG TGACAGTAGTTTTTGCAAAAAAGAC CACCAGTTAGAAAGTTTAACTGATAG GGAATTACTCCTACTAATCGCCCGTA AGACTTGTGGATCAGTAGAACAACA ATTAAATATAACTGCACCCAAGGACT CG	Template for PCR
ZEBOV-T7	GCGCTAATACGACTCACTATAG GGTGCGCGTTCCTACTGTATT	PCR primer for ZEBOV VP30 dsDNA, with T7 for IVT
qPCR-ZEBOV-F	GTGCGCGTTCCTACTGTATT	qPCR primer for ZEBOV
qPCRT-ZEBOV-R	GAGTCCTTGGGTGCAGTTATATT	qPCR and RT primer for ZEBOV
ZEBOV RPA-1	CTACTGTATTTCATAAGAAGAGAGTTGAACC	RPA forward primer
ZEBOV RPA-2	AATTGTTGTTCTACTGATCCACAAGTCTTAC	RPA reverse primer

Table 4 – Targets for Cas12a collateral activity and structural hydrogel components

Name	Sequence (5' to 3')	Modifications	Notes
Fluorophore-quencher ssDNA reporter	TTATT	5'-6FAM 3'-IowaBlack	In-solution reporter Fluorescent after cleavage
Acrydite oligo X	TTATTCTTGTCTCCCGAGAT	5'-Acrydite	Grafted in PA-DNA gels
Acrydite oligo Y	TTATTTCACAGATGAGTATC	5'-Acrydite	Grafted in PA-DNA gels
Linker-15	GATACTCATCTGTGATTATT TTATTTTATTATCTCGGGAG ACAAG	5'-6FAM-dT (if fluorescent)	PA-DNA gel cross-linker
PEG gel reporter	TTATTATTACTATCTATTATC ATTATCATT	5'-C6-SH 3'-Cy3	Grafted in PEG gels
PEG gel reporter A	TTTACACAAGCACTACGTAC ACTACCACAT	5'-DTPA 3'-6FAM	Grafted in PEG gels Anneals with protector A'
Protector sequence A	ATGTGGTAGTGTACGTAGTG CTTGTGTAAA	N/A	Grafted in PEG gels Anneals with reporter A
PEG gel reporter B	TTTTTATTTATCTATCTGACG A	5'-C6-SH 3'-Cy3	Grafted in PEG gels Anneals with protector B'
Protector sequence B	TCGTCAGATAGATAAATAAA AA	N/A	Grafted in PEG gels Anneals with reporter B
Biotin anchor	TTATTATTACTATCTATTATC ATTATCATT	5'-C6-SH 3'-Cy3	Anchors avidin conjugates in PEG gels

liquid for several minutes, during which we cast individual 5 μL hydrogels either in microtubes or non-treated, clear flat bottom 96-well plates. We sealed the containers and allowed the gels to polymerize for 1 h at room temperature.

– *Hydrogel washing and swelling.* After polymerization, we washed the gels three times to eliminate unbound precursors and polymerization buffer; these steps also allowed the swelling of hydrogels to their equilibrium volume. Washing steps lasted at least 4 h each, and were performed in an excess (>30-fold relative to gel precursor volume) of washing buffer (10 mM Tris-HCl, 50 mM NaCl, 10 mM $MgCl_2$, pH of 8) at 37^{o}C.

– *In-gel cleavage of ssDNA anchors.* Unless mentioned otherwise, PEG cargo release assays were performed as follows: we mixed 50 nM of Cas12a with a two-fold excess of

the appropriate guide RNA and 50 nM of dsDNA trigger or scrambled sequence. We assembled the reactions in NEB buffer 2.1 (10 mM Tris-HCl, 50 mM NaCl, 10 mM $MgCl_2$, 100 μg/ml BSA, pH of 7.9). For quantitative experiments, we used a 20-fold volume excess of reaction mix relative to hydrogel pre-swelling volume; e.g., we added 100 μL of reaction mix on top of 5 μL gels. All digestions were performed at 37^{o}C with periodic shaking (1 s/min). We observed the progression of ssDNA cutting in the gels on a plate reader (M5 SpectraMax, Molecular Devices) by continuously measuring fluorescence accumulation in the supernatant, caused by the release of the DNA-bound Cy3 dye. We used wavelengths (Ex.554 / Em.625) maximizing the signal-to-noise ratio of the fluorophore. We normalized the data versus complete (100%) cleavage, defined by measuring fluorescence in a solution of fluorophore-bound oligonucleotides, diluted so as to match the expected molarity of anchors in the buffer+gel system, assuming perfect functionalization and release. We applied first-order Savitzky-Golay filters to correct for measurement noise.

Spike-in experiments in PEG gels – To test the dynamic response of Cy3-DNA-decorated gels upon activation of Cas12a, followed the basic gel synthesis and Cas12a-mediated degradation protocols, with small variations. We used larger gels (20 μL on the sides of 48-well TCPS plates) overlaid with 250 μL of supernatant. During the experiment, we initially introduced reaction buffer without enzymes or nucleic acids. At timepoint t = 1 h, we spiked in a concentrated (200X) solution of primed enzyme (10 μM Cas12a, 15 μM gRNA in 1X NEB 2.1 NEB 2.1 buffer), and monitored the response of the system.

Grafting and release of HRP on PEG gels – We synthesized 3 μL PEG hydrogels in microtubes following the method described above, with smaller final concentrations

of PEG (1.5% w/v) and DNA (5 μM). In addition to the 5'-thiol modification, the oligonucleotides harbored a 3'-biotin modification instead of a fluorophore, which we used to capture streptavidin-modified HRP. After casting the gels and washing overnight, we blocked any remaining unreacted vinyl sulfones by incubating the gels for 4 h at 37^{o}C with 20 mM of dithiothreitol freshly dissolved in wash buffer. We then rinsed the gels (3x 1h) in wash buffer, after which we added 55 μg/ml of streptavidin-conjugated HRP (Pierce) to wash buffer for an overnight (16 h) incubation at room temperature. We then washed the gels (incubations of 2 h in wash buffer) until there was no residual HRP activity in the supernatant. We assessed residual HRP activity by diluting wash buffer aliquots 5-fold in a 3,3',5,5'-tetramethylbenzidine (TMB) substrate solution (Millipore Sigma) and incubating at 37^{o}C for 20 min before checking for the presence of a blue TMB oxidation product. We then proceeded to the digestion of the gels using Cas12a; we overlaid the hydrogels with 20μL of pre-warmed reaction mix (10 nM Cas12a, 20 nM gRNA, 10 nM trigger or scrambled dsDNA in 1X NEB buffer 2.1) and incubated the gels at 37^{o}C with gentle rocking. At each time point, we pipetted out the supernatant, which we stored at 4^{o}C until the end of the experiment. After the last sampling, we pipetted 10 μL of each supernatant into 40 μL of TMB substrate solution dispensed in a 96-well plate, incubated the reaction at 37^{o}C with shaking for 10 min and blocked the reaction with 50 μL of 1M H2SO4. We quantified relative enzymatic activity in the supernatant by measuring absorbance ($\mu = 450$nm). When testing for the ability to discriminate between trigger and scrambled sequences, we diluted a 100 nM stock of Cas12a, gRNA and dsDNA (1:2:1 molar ratio) to the appropriate desired concentrations and used 50 μL of supernatant on the DNA-HRP decorated gels, which we incubated for 3 h at 37^{o}C before testing for enzymatic activity in the supernatant by incubation with TMB substrate and absorbance monitoring at 650 nm.

Input dsDNA sequence specificity of Cas12a-mediated cleavage in PEG hydrogels – We performed all the cross-reactivity tests on 5 μL PEG gels (2% w/v) synthesized as described above in a 96-well plate, using the same digestion protocol: all enzymes and dsDNA fragments were introduced at 50 nM with a two-fold molar excess of gRNA, and reactions were monitored by fluorimetry for 12 h.

Measuring PEG-DNA cutting kinetics for various amounts of dsDNA input – We performed the experiment as described above, with successive 5-fold dilutions of dsDNA trigger while maintaining constant the molarity of enzyme and guide (50 nM and 100 nM, respectively).

Modulation of Cas12a activity through alterations of PEG gel physical properties – We made the following changes to the general PEG hydrogel synthesis strategy: we only added half of the usual volume of PEG-VS stock at 4% (w/v) for reaction with the reduced DNA; at the end of the grafting reaction, we added another half-volume of PEG-VS diluted in 1M triethanolamine (stock concentration: 2, 2.4, 2.8, 3.2, 3.6 and 4%), thereby decreasing the final PEG-VS concentration by up to 25% while maintaining the DNA concentration constant. We then added a full volume of PEG-SH stock diluted accordingly (stock concentrations: 3, 3.2, 3.4, 3.6, 3.8 and 4%, respectively), and adjusted the volume with water before casting the gels in a 96-well plate; the resulting hydrogels had concentrations ranging from 1.5 to 2%. We then washed and digested the gels following the usual procedure described above.

Hybridization-mediated protection against Cas12a cutting in PEG gels – Protection assays were performed in 1.5% (w/v) PEG gels harboring 2.5 μM of reporter oligonucleotides functionalized on the gel-distal end with 6-carboxyfluorescein (6-FAM).

After casting, swelling and washing the DNA-decorated hydrogels, we incubated them in wash buffer supplemented with oligonucleotides complementary to the 6-FAM anchors, or containing an identical amount of non-matching DNA as a control. We tested three orders of magnitude of anchor to free oligos ratios; for instance, 5 μL hydrogels with 2.5 μM of immobilized reporter DNA were covered with 50 μL of complementary or non-complementary oligonucleotides at 250 nM in buffer solution. Hydrogels were incubated at 37^{o}C overnight (16 h) with the DNA solutions for hybridization, then washed (3x 2h) with wash buffer without DNA to remove unbound oligonucleotides. We then assayed Cas12a sensitivity following the general method outlined above.

Synthesis of carbon black-DNA gels – We prepared aqueous suspensions of carbon black according to a modified version of the protocol by Parant *et al.* [2017]. We prepared a stock of 1.5% (w/v) Arabic gum (Sigma, CAS: 9000-01-5) by dissolving for 2 h in water at 80^{o}C. We then added 8% (w/v) acetylene black particles (>99.9%, Alfa Aesar, AA3972430) and resuspended by ultrasonication for 15 min (Fisher Scientific FB505 Sonic Dismembrator). We prepared carbon black-DNA hydrogels according to the protocol described by Xu *et al.* [2010a], but we used an 8% (w/v) carbon black suspension in place of the reduced graphene oxide. Briefly, we mixed the 8% (w/v) carbon black (with 1.5% (w/v) Arabic gum) in a 1:1 ratio with a solution of 20 mg/ml salmon sperm DNA (Sigma, CAS: 438545-06-3). We heated the mixture to 90^{o}C with shaking at 1400 rpm for 5 min, before depositing 1-3 μL via pipette onto inkjet-printed, interdigitated silver electrodes (IDEs). After 5 s (before significant evaporation could occur), we submerged the gel-coated electrodes in liquid nitrogen and lyophilized them for 18-24 h in a benchtop freeze-dryer (Labconco, USA). We fabricated the flexible interdigitated electrode using a silver nanoparticle ink pattern deposited over a polyethylene terephthalate NanoBenefit 3G Series film (Mitsubishi Imaging MPM

Inc., Rye, NY) using a previously reported conductive inkjet printing method [Cai *et al.*, 2017].

Conductivity measurements of carbon black-DNA gels – To estimate the conductivity of the lyophilized carbon black-DNA gels, we prepared samples on inkjet-printed silver electrodes with an adhesive silicone isolator as a mold. We cast the gels with a length of 2.00 mm, width of 2.00 mm, and height above substrate of 1.00 mm such that they spanned a 0.43 mm gap between two printed silver electrodes, and lyophilized the gels in the molds for 24 h. We used a multimeter (Fluke, USA) to measure the resistance reading between the silver electrodes spanned by the gel. Specifically, we used the two-contact probe method described by Sun *et al.* [2016] to calculate the conductivity σ using the cross-sectional area of the gel and the distance between the probes:

$$\sigma = \frac{1}{V} \times \frac{L}{wt}$$

Where L is the separation distance (0.43 mm), w is the width (2.00 mm) and t is the height (1.00 mm). By measuring the conductivity of 10 samples, we obtained a mean value of 4.2 ±0.8 mS/cm.

***In vitro* reaction of Cas12a with carbon black-DNA gels –** To measure the detachment of lyophilized carbon black-DNA gels from a surface, we deposited gels on flexible, inkjet-printed silver electrodes. After lyophilization of the gels for 18h, we took resistance measurements using a multimeter (Model 179, Fluke, USA) and any electrodes with a reading >1 kΩ were excluded as defective before assigning the electrodes to the test groups. We then placed electrodes individually in the bottom of 1.5 mL Eppendorf tubes and then submerged in 75 μL of the Cas12a reaction mix to ensure the gels were

completely covered. The aqueous Cas12a reaction mix contained 1X NEB 2.1 buffer, 0.75 μM Ca12a, 1.3 μM gRNA and varying concentrations of the dsDNA trigger (0.05, 0.1, 0.5 and 1.0 μM). The control reaction mixes contained 1 μM of a scrambled trigger dsDNA sequence and 0 μM dsDNA (Cas12a-gRNA only control). We incubated the lyophilized gels in the Cas12a reaction mixtures at 37°C for 24 h, with five replicates for each dsDNA trigger concentration (including the control). At 1 h intervals, the Eppendorf tubes were shaken for 10 s at 800 rpm. After shaking, we visually inspected the silver electrodes and recorded the complete detachment of any gels from the substrate. Upon detachment of a gel, we removed the corresponding electrode from the reaction and allowed it to dry. We recorded images of the electrode with a Leica MZ10 F microscope (brightfield mode, 100 ms exposure, gain = 2.0, saturation = 1.0) and a took resistance measurements with a multimeter. At the 24h timepoint, we removed all remaining electrodes from the reactions, and recorded images and resistance measurements as above. Finally, we manually quantified the area of the gels remaining on the electrodes (in pixels) relative to the area of the electrode itself using ImageJ version 1.52a. We then repeated this experiment an additional two times, with the modification that all electrodes were removed from the reaction at a single, set timepoint (10 h and 21 h, respectively). For the first repeat, we used dsDNA trigger concentrations of 1.0 and 0.5 μM as well as a 1.0 μM scrambled dsDNA control (n = 6 for each condition); after 10 h, we stopped the reaction, dried the electrodes in air, and took a resistance measurement, using a multimeter (Model 179, Fluke, USA). For the second repeat, we used dsDNA trigger concentrations of 0.1 and 0.05 μM, as well as a 1.0 μM scrambled dsDNA control (n = 6 for each condition); after 21 h, we stopped the reaction, dried the electrodes in air, and took a resistance measurement.

***In vitro* reaction of carbon black-DNA gels with Mung Bean Nuclease (MBN) –** PET/Ag Electrodes with carbon black-DNA gels were prepared as above and initial resistance measurements taken using a multimeter (Model 179, Fluke, USA). The electrodes were placed in 1.5 mL Eppendorf tubes and submerged in 75 μL of reaction mix. We prepared reactions (n = 10 for each condition) containing 0.2 U/μL MBN (NEB), 0.2 U/μL heat-inactivated MBN (HI MBN), and no MBN all in 1X Mung Bean Nuclease buffer (NEB). We produced the HI MBN by incubating a 1 mL solution of 0.2 U/μL MBN in 1X MBN buffer at 95^{o}C for 2 h before allowing it to cool to room temperature before the experiment. We incubated the lyophilized carbon black-DNA gels in the reaction mixtures at 30^{o}C for 2 h, at which point we removed all the electrodes and allowed them to dry. We recorded images of each electrode with a Leica MZ10 F microscope (100 ms exposure, gain = 2.0, saturation = 1.0) and took resistance measurements with a multimeter.

Synthesis of acrylamide-DNA gel precursors – We produced acrylamide-DNA hydrogels using a modified version of a previously described method [Previtera & Langrana, 2014]. HPLC-purified single-stranded oligos (Oligo-X and Oligo-Y, described below) functionalized with a methacryl group at their 5'-end (IDT) were resuspended in water to a final concentration of 3 mM. Linker oligos (IDT) without functionalization (L15, described below) were also resuspended in water to a final concentration of 3 mM. We prepared a 10X concentrated stock of the reaction buffer from Bio-Rad 50X TAE buffer supplemented with magnesium acetate (125 mM) such that the final concentrations in the reaction were 1X TAE and 12.5 mM Mg^{2+}. Fresh aqueous solutions of 20 v/v% N,N,N',N'-tetramethylethane-1,2-diamine (TEMED, Millipore Sigma, USA) and 2% (w/v) ammonium persulfate (APS, Millipore Sigma,USA) were prepared before each reaction.

Production of oligo-functionalized acrylamide polymers Ps-X and Ps-Y – We prepared separate reactions of between 50-400 μL for each oligo X and Y in 1.5 mL Eppendorf tubes (final concentration in brackets). We mixed methacryl-functionalized oligos (1 mM), TAE/Mg^{2+} buffer (1X) and 40% acrylamide (4%) in water at room temperature, vortexed briefly to mix, and de-gassed the reactions under vacuum for 15 min. We then added APS (0.05% (w/v)), inverted the tube to mix, and collected the contents by spinning down briefly. TEMED (0.5% v/v) was then added and the mixing repeated. We allowed the reactions to proceed under vacuum at room temperature for 20 min. Incorporation of DNA oligos into the polymer strands was confirmed by agarose gel electrophoresis. To confirm incorporation of ssDNA into the polyacrylamide backbone, the pre- and post-reaction mixtures were run on an agarose gel. For this, we prepared a 2% agarose gel containing 1X NorthernMax-Gly gel running buffer (Invitrogen). For ssDNA methacryl-oligos X and Y, samples from the relevant pre-reaction mixes containing 10 pmol of each oligo were brought to 4 μL, mixed with 4 μL of NorthernMax-Gly gel loading dye, and incubated at 50^{o}C for 30 min before loading into the gel alongside a low molecular weight DNA ladder (NEB). We took 2 μL samples of the polymerized gel precursors X and Y (4% or 7%), mixed them with 2 μL of water and 4 μL of NorthernMax-Gly gel loading dye, and incubated at 50^{o}C for 30 min before loading into the gel alongside a low molecular weight DNA ladder (NEB). The gel was run for 1.5 h at 80 V 1X NorthernMax-Gly gel running buffer and imaged under UV light using a G:Box Mini (Syngene USA). Ps-X and Ps-GRNA stocks were stored at 4^{o}C for up to 2 weeks.

Bulk degradation of polyacrylamide-DNA gels using FITC-dextran microparticles – We prepared 10 μL gel mixtures in 1.5 mL Eppendorf tubes by combining (in order): 4% or 7% Ps-X & -Y (3.00 μL), 10X NEB 2.1 buffer (0.67 μL), 2.5 mg/ml FITC-Dextran

(500 kDa, 1.00 μL), Cas12a reaction master mix (1.00 μL), 100 μM trigger or scrambled dsDNA (0.33 μL) and 3 mM linker DNA (L-15, 1.0 μL). The Cas12a master mix was prepared on ice and consisted of NEB LbaCas12a (10 μM) and an MRSA gRNA (15 μM) in 1X NEB 2.1 buffer. The final concentrations of the reagents in the 10 μL gels were as follows: 1.0 μM Cas12a, 1.5 μM MRSA gRNA, 0.25 mg/ml FITC-Dextran, 3.3 μM trigger or scrambled DNA. To enable gelation, the mixtures were incubated at room temperature for 20 min. After gelation, a supernatant consisting of 850 μL of 1X NEB 2.1 buffer was added. The final concentrations of the reagents in the wells were as follows: 11.6 nM Cas12a, 17.4 nM MRSA gRNA, 2.90 μg/ml FITC-Dextran, 38.4 nM trigger or scrambled DNA. The reaction tubes were incubated at 37^{o}C for 20 h. Every 4 h, the tubes were inverted once, and imaged under UV light (Ex: 385 nm / Em: 525 nm) using a G:Box gel imager (Syngene USA).

Gold nanoparticle synthesis and PEG functionalization – We produced gold NPs (AuNPs) by reducing chloroauric acid ($HAuCl_4$, Sigma) with sodium citrate (Sigma), following the method of Turkevich *et al.* [1951]. Briefly, we added 1 mL of a 6.8 mM sodium citrate solution to 50 mL of 0.25 mM gold (III) chloride, while the gold chloride solution was boiling. We stirred the samples and heated for 15 min during which the gold crystals formed. Nanoparticles were left to cool down to room temperature while stirring continued. To functionalize the AuNPs with PEG, we added 0.33 mL of 2 mM, 5 kDa thiol-terminated poly(ethylene glycol) methyl ether (mPEG, Nanocs, USA) to the synthesized AuNPs and allowed to them We performed AuNP characterization after synthesis by assessing optical absorption. We obtained spectra of the AuNPs on a Cary 300 UV-Vis (Agilent Technologies, USA). We characterized the morphology of the AuNPs was characterized with a FEI Tecnai G2 TEM at 120 kV. We then used ImageJ to process the images and measure the dimensions of the AuNPs. Finally, we used a Zetasizer Nano

Zen3600 (Malvern Instruments, UK) to measure the hydrodynamic diameter and the zeta potential (ζ) of the NPs.

Gold nanoparticle release from acrylamide gels – We prepared 9 μL gel mixtures in PCR tubes by combining (in order): 4% or 7% Ps-X & -Y (3.00 μL), 10X NEB 2.1 buffer (0.67 μL), 5 μM PEG-AuNPs (1.00 μL), Cas12a reaction master mix (1.00 μL), and 100 μM trigger or scrambled dsDNA (0.33 μL). The Cas12a master mix was prepared on ice and consisted of NEB LbaCas12a (10 μM) and an MRSA gRNA (15 μM) in 1X NEB 2.1 buffer. The final concentrations of the reagents in the 10 μL gels were as follows: 1.0 μM Cas12a, 1.5 μM MRSA gRNA, 0.5 μM PEG-AuNPs, and 3.3 μM trigger or scrambled DNA. Press-to-Seal silicone isolators (round, 2.0 mm diameter, 1.7 mm depth, ThermoFisher Scientific, USA) were cut into single units and attached to the center of the bottom of individual wells in a 24-well tissue culture plate. We pipetted the 9 μL gel mixtures into the silicone isolators, and added 3 mM linker DNA (L-15, 1.0 μL). The mixtures were stirred briefly with a pipette tip and then incubated at room temperature for 20 min. After gelation, we added a supernatant consisting of 850 μL of 1X NEB 2.1 buffer to each well. The final concentrations of the reagents in the wells were as follows: 11.6 nM Cas12a, 17.4 nM MRSA gRNA, 5.81 nM PEG-AuNPs, 38.4 nM trigger or scrambled DNA. We then transferred the 24-well plate to a plate reader and recorded absorbance readings (520 nm) from the center of the 24-well plate (i.e. through the gel itself) every 2 min for 15 h at 37^{o}C; data were smoothened with a first-order Savitzky-Golay filter. At the 15 h timepoint, we removed the 24-well plate and took a 200 μL sample of the supernatant from each reaction and transferred them to a 96-well plate. To calculate the final % release of AuNPs, we measured the A520nm of the supernatant and compared it to a 100% release standard containing 5.81 nM PEG-AuNPs.

Preparation of polyacrylamide-DNA gels for bulk degradation using EvaGreen and cell release – We prepared a pre-gel stock with a 1:1:0.6 ratio of Ps-X, Ps-Y and 10μM bridge and incubated to cross-link for 10 min. We then used an Amicon 10kDa spin filter to centrifuge and resuspend the pre-gel stock to remove free acrylamide monomers. We performed washing and spin filtering two additional times prior to Evagreen bulk degradation or cell release. We used a nanodrop to normalize the concentration of the final pre-gel stock mix to 1.8 mg/ml of ssDNA.

Gelation of polyacrylamide (PA)-DNA with EvaGreen for bulk hydrogel degradation – We prepared 150μL gel mixtures by combining 100 μL of the pre-gel stock mix at 1.8 mg/ml ssDNA with 5 μL of 3mM bridge, 15 μL of 10X NEB 2.1 solution, 7.5 μL of 20X EvaGreen and 22.5 μL of PBS. The mixture was kept at 37^{o}C to minimize cross-linking while the gels were spotted on a 384-well plate. We dropped the 1 μL gels at the bottom of the 384-well plate and allowed them to cross-link for 20 min. For gel-degradation experiments, we added 20 μL of a solution containing 1 μM Cas12a, 1.5 μM gRNA and dsDNA trigger (5 μM, 2 μM, 1 μM, 0.2 μL) on top of the PA-DNA hydrogels, and EvaGreen fluorescence was recorded on a Synergy Neo at 37^{o}C (Ex: 490 nm / Em: 535 nm).

Primary cells for DNA-polyacrylamide gel release – We performed cell release experiments using primary peripheral blood mononuclear cells (PBMCs). Mobilized peripheral blood and leukapheresis product were anonymously collected from donors undergoing stem cell mobilization at the Massachusetts General Hospital (MGH) under Institutional Review Board approved protocol #2015P001859. We purified the mononuclear cells via Histopaque 1077 gradient (Sigma, 10771). We expanded PBMCs in RPMI 1640 + GlutaMAX Medium (Thermo Fisher Scientific, Waltham, MA) supplemented with 10%

fetal bovine serum and 2 ng/ml recombinant IL-2. We prepared the cell suspension by spinning down the cell culture at 300 x g for 5 min and resuspending cells at 10^7 cells/ml.

Gelation of polyacrylamide (PA)-DNA with encapsulated cells – We combined 30 μL of washed pre-gel stock with 30 μL of cell-bridge mixture containing 270 μM bridge, 30 μM fluorescently labeled bridge, $2x10^6$ cells and 30 mM $MgCl_2$ in 1X PBS. The solution was mixed until gelling appeared homogeneous and the pipette flow became highly viscous. Hydrogel droplets (2 μL) were deposited at the center of each well in a sterile 96-well plate with flat clear bottom, and incubated at 37^oC for 2 min. After droplet incubation, we added 100 μL of RPMI with 10% FBS (R10) or OMEM media with 10% FBS and 10mM $MgCl_2$ (O10 + $MgCl_2$) with Cas degradation reagents gently from the side of the well to avoid pressure driven hydrogel dislodgement. In the representative cell-encapsulation image of Figure 12, PBMCs were pre-stained before encapsulation to allow for in-gel visualization using calcein blue-AM (live, blue color) and ethidium homodimer-1 (dead, red color). In other experiments, PBMCs were not pre-stained to allow for cell viability assessment after gel degradation and release.

Cell release from DNA-polyacrylamide gel and viability analysis – We incubated the hydrogels with encapsulated PMBCs at 37^oC with 100 μL Cas12a solutions containing 0.5 μM Cas12a, 1 μM gRNA, 0.1X NEB buffer 2.1, scrambled dsDNA at 5 μM, or trigger dsDNA at 5 μM, 1 μM, and 0. 2μM. Negative controls contained RPMI media with 10% FBS, as well as OMEM media with 10% FBS and 10 mM $MgCl_2$. Gel degradation started upon addition of the Cas solution, and we monitored hydrogels to assess degradation kinetics. After Cas-mediated hydrogel degradation and PBMC release, we assessed cell viability using ethidium homodimer-1 (Invitrogen) and calcein blue-AM. This was

performed on replicates of the experiments where the cells had not been pre-stained for imaging purposes. We performed the cell-encapsulation and cell-release imaging using an EVOS FL digital inverted imaging system with four-color fluorescence and transmitted-light capabilities. We acquired images of PA-DNA hydrogel macroscopic morphology before and after Cas degradation using an EVOS® FL digital inverted microscope set for GFP fluorescence (Ex: 470 nm / Em: 525 nm) using a 4x magnification objective, 30% LED illumination intensity and 50% contrast. After gel degradation we acquired images of released PBMCs from PA-DNA hydrogels using an EVOS FL digital inverted microscope with a 20X objective. We performed imaging of live cells using DAPI mode (Ex: 360 nm / Em: 447n m) with 40% LED illumination intensity and 90% contrast. Dead cells were imaged using the RFP mode (Ex: 530 nm / Em: 593 nm) with 50% LED illumination intensity and 90% contrast. The GFP channel was also acquired at this magnification to assess gel degradation.

Cell viability in Cas12a reaction conditions – We assessed viability after 24h incubation at 37^{o}C by staining cells with calcein-AM and ethidium homodimer-1 (Invitrogen, Eugene, Oregon). We incubated cells in the following conditions: R10 media (RPMI with 10% FBS), O10 test media containing OMEM media, 10% FBS and 10 mM $MgCl_2$, and O10 test media with 0.5 μM Cas12a, 1 μM gRNA, 0.1X NEB buffer 2.1 and 1 μM scrambled or trigger dsDNA.

Fabrication of CRISPR-gel μPad stop-flow system with electrical readout – We fabricated paper μPADs according to a modified version of the protocol published by Wei *et al.* [2015], using a double-sided wax printing pattern. We designed top and bottom μPAD wax layers using Illustrator CC v23.0.4 (Adobe Inc. San Jose, CA), and printed them on Whatman Grade 1 chromatographic filter paper (Thermo Fisher Scientific,

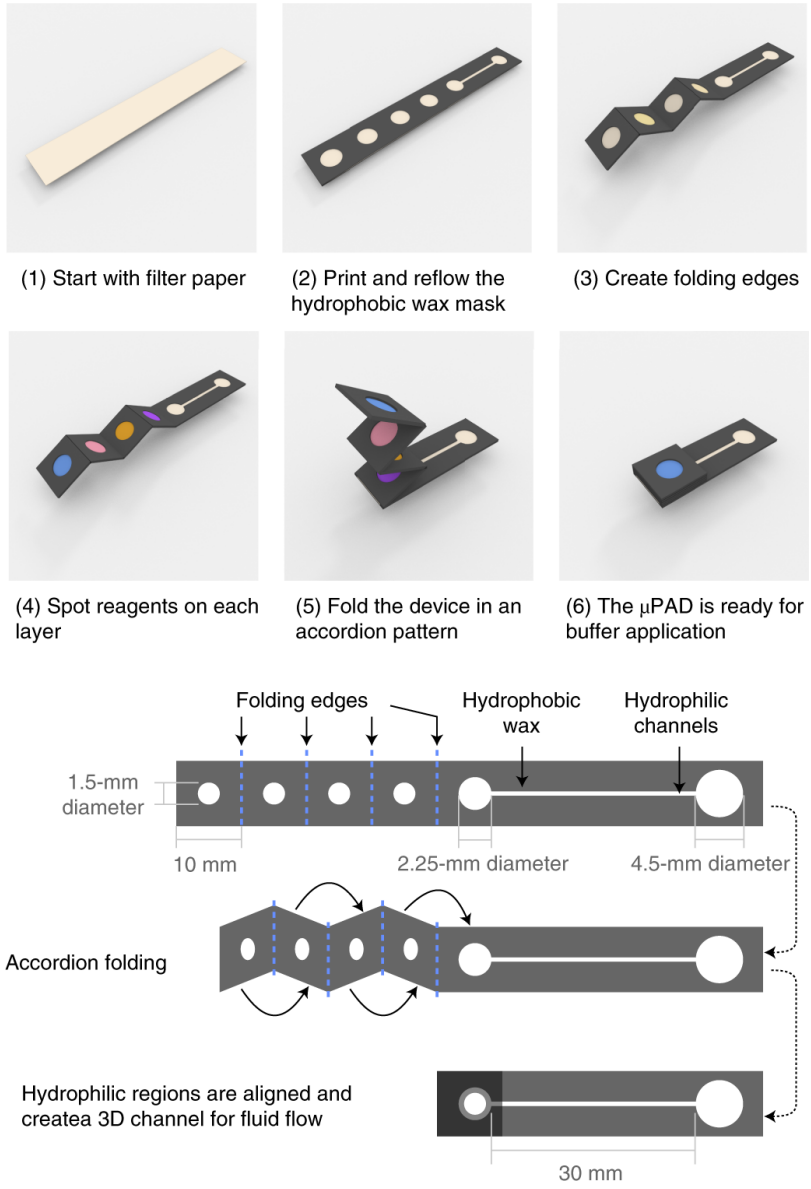

Figure 38 – Folding of μPAD devices. Top: the μPAD assembly starts with a piece of filter paper (1) to which a hydrophobic mask is applied by wax printing (2). The structure is then folded (3–5) to generate the assembled device, before buffer application (6). Bottom: the stacked μPAD structure is assembled by folding paper layers on top of each other so as to align the hydrophilic regions and create a continuous channel that ends in the final lateral flow channel.

Waltham, MA) using a Xerox Phaser 8560 printer. Printed μPAD sheets were wax reflowed through hot pressing for 15 s at 125°C using a Cricut EasyPress (Cricuit Inc., Fork, UT), and then cooled to room temperature. We cut and folded individual μPADs (Figure 38), and confirmed alignment of hydrophilic sections using a light source and visual inspection. Any μPADs with visible printing, reflowing or alignment defects were discarded. After baking and folding, layers 1 to 4 of the μPADs were ensured to exhibit circular hydrophilic paper regions for vertical flow of approximately 1.5 mm in diameter, surrounded by an evenly distributed hydrophobic wax coating to prevent undesired lateral flow. Layer 5 of the μPADs contains a 1.5 x 30 mm lateral flow channel with marked lengths. To prepare functional μPADs, first, we filled layer 3 with 0.5 μL of oligo-functionalized acrylamide polymer solution containing both Ps-X and Ps-Y (1:1). Then we filled layer 4 with PBS buffer containing food color dye (0.5 μL, 1:5 red dye/PBS). We then freeze-dried paper μPADs with deposited reagents in layers 3 and 4 before continuing assembly. To measure conductivity measurements, we covered Layer 5 of the μPADs with 3x30 mm strips of 87580-Nickel/Copper Conductive Fabric Tape (Laird Technologies EMI, Pall Mall, London) placed along the top and bottom sides of the lateral flow channel to act as parallel conductive planes to measure channel electrical resistance as a function of buffer wicking distance. We laminated both the conductive tape and wiring for connection over layer 5 using plastic tape to prevent detachment. We left layer 1 and layer 2 of the μPADs uncovered to receive the conductive buffer and DNA linker during testing.

Flow and conductivity measurements in μPAD – At the time of testing, we filled layer 2 of the μPADs with 0.3 μL of ssDNA linker (100 μM) that had been pre-incubated for 4 h at 37°C in a cutting solution containing 300 nM Cas12a, 1 μM MRSA gRNA, and dsDNA MRSA Trigger (at concentrations 0 nM, 0.4 nM, 2 nM, 10 nM, 50 nM) in

1X NEB Buffer 2.1. Negative control reactions were performed with scrambled MRSA dsDNA. After the pre-digested ssDNA bridge solution had been deposited and air dried for 1 min, we collapsed the μPAD to fluidically connect all hydrophilic regions with layer 1 acting as a protective cover for all other layers and as the inlet for running PBS buffer. MRSA μPAD experiments were conducted using 10 μL of running PBS buffer, while EBOV μPAD experiments were done using 2 μL running PBS buffer. We continuously monitored μPAD channel resistance using a 34411A Digital Multimeter (Keysight Technologies Inc., Santa Rosa, CA) for dynamic measurements, and we took endpoint values at 5 min for determining the sensitivity curve. We conducted testing of flow and conductivity measurements in the μPAD in triplicate. Representative samples of paper μPAD regions with visible polyacrylamide-DNA gelation due to the presence of uncut DNA linker were imaged using a scanning electron microscope and compared to un-gelled regions where cut ssDNA linker was present. We performed positive controls to validate enzyme activity during Cas12a-mediated cleavage of the polyacrylamide gel linker in reactions that contained 300 nM Cas12a, 1 μM MRSA gRNA, and increasing concentrations of dsDNA MRSA Trigger (0 nM, 0.4 nM, 2 nM, 10 nM, 50 nM) and NEB Buffer 2.1 (1X), as well as 750 nM ssDNA quenched fluorescently labeled reporter. We used the fluorescence readings as a proxy to confirm the activity of Cas12a in the pre-incubation reaction.

RFID integration in CRISPR-mediated stop-flow μPAD – To construct the CRISPR-active RFID sensor, we modified a 10 x 70 mm flexible WRL-14147 ultrahigh-frequency RFID tag (SparkFun Electronics Inc., Niwot, CO) with a flexible IDE capable of short-circuiting an inner loop of the tag antenna in the presence of conductive buffer at a specific vertical layer or lateral flow distance of the previously described μPAD. We fabricated the flexible interdigitated electrode using a silver nanoparticle ink pattern,

deposited over a polyethylene terephthalate NanoBenefit 3G Series film (Mitsubishi Imaging MPM Inc., Rye, NY) using a previously reported conductive inkjet printing method [Lee *et al.*, 2005]. We connected both electrode terminals to the first loop regions at this specific RFID tag antenna, which is located in close proximity to the UHF-RFID chip. For the MRSA μPAD RFID measurements we assembled a modified four-layer μPAD stack (without layer 5) on top of the RFID device as a flow-through arrangement, aligning the bottom of the hydrophilic region in layer 4 to be in contact with the interdigitated electrode. For the EBOV μPAD RFID measurements we assembled a modified five-layer μPAD aligning entry of the lateral flow hydrophilic channel of layer 5 to be in direct contact with the interdigitated electrode. We performed reagent placement and activation as with the μPAD flow and conductivity measurements previously described. We measured the relative received signal strength (RSSI) of each μPAD RFID tag in the presence or absence of target DNA after incubation in the cutting solution containing Cas12a, gRNA, and linker DNA. Reduction in absolute RSSI values indicates that the power level of the received radio signal has decreased due to conductive buffer flow and RFID tag antenna short-circuiting. As initial proof-of-concept of this effect in the MRSA μPAD RFID arrangement, we measured the RSSI for two independent tags (one modified and one unmodified) both placed at a distance of 0.5 m from a WRL-14131 UHF-RFID TNC antenna (SparkFun Electronics Inc., Niwot, CO) connected to a M6E-NANO simultaneous RFID tag reader (SRTR) (ThingMagic Inc. Bedford, MA) and an Arduino Uno microcontroller (Arduino LLC, Somerville, MA) using the M6E-NANO RFID Arduino library.

Ebola diagnostic and EBOV RT-RPA CRISPR μPAD – To demonstrate applicability of the CRISPR μPAD RFID mode of sensing, we sought to develop a sensitive Ebola virus RT-RPA CRISPR μPAD. To achieve this, dsDNA fragment encoding for Zaire strain

Ebola virus VP30 protein was obtained from IDT, and was then amplified by PCR and transcribed *in vitro* using HighScribe Quick (NEB). We tested serial dilutions of the RNA by RT-RPA followed by Cas12a detection. We used Superscript (Invitrogen) for the RT step using EBOV-R primer, following manufacturer's instructions. Then, we added 5 μL of the reverse-transcribed RNA to 50 μL of RPA basic (TwistDx) lyophilized reactions that contained 480 μM of each RPA primer and 14 mM magnesium acetate, as per manufacturer's instructions. We incubated the RPA reaction for 40 min at 37^{o}C. After amplification, we added the ssDNA linker, gRNA and Cas12a to final concentrations of 300 μM, 0.9 μM and 0.5 μM, respectively. We incubated samples for 4 h, then diluted 1:1 with nuclease-free water (all called RT-RPA/linker mix) and tested in the μPADs. To assemble the μPAD, we deposited 0.3μL of RT-RPA/linker mix in layer 2, 0.3 μL of 4% Ps-XY in layer 3 and 0.3 μL 1X PBS with red dye in layer 4. Lateral flow region in layer 5 was placed in contact with the interdigitated electrode of the modified RFID tag starting at 2 mm from channel entry. Reagents were air dried for 2 min and μPAD was collapsed to allow for contact of hydrophilic sections. Running 1X PBS buffer (2 μL) was added to the Layer 1 (top) of the μPAD to start readings. Colorimetric readings of the EBOV RT-RPA CRISPR μPAD detection system were obtained at increasing concentrations of input EBOV RNA trigger (0 aM, 2 aM, 11 aM, 53 aM, 255 aM, 1.4 fM, 6.8 fM, 34 fM, 170 fM, 853 fM, 4.2 nM and 21 nM). In solution readouts from analogous RPA reactions for comparison with the μPAD system, we prepared with final concentrations of 50 nM Cas12a: 62.5 nM gRNA: 750 nM FQ reporter in NEB 2.1 buffer to 50 μL of RPA reactions. We then incubated these verification reactions (3 μL, 384-well microplate) at 37^{o}C for 2 h and fluorescence was recorded in a fluorescence plate reader (Biotek NEO HTS) (Ex: 485 nm / Em: 535 nm).

RFID readings of EBOV RT-RPA CRISPR μPAD – The detection an RFID signal change from the EBOV RT-RPA CRISPR-active μPADs is caused by conductive buffer flow through layer 5, which is located in contact with the inkjet-printed interdigitated electrodes that are in turn connected to the first antenna loop of the RFID tags. We measured the received signal strength indicator (RSSI) in the testing RFID μPAD in combination with an attached unmodified reference tag using an ultra-high frequency (UHF) RFID antenna positioned around 0.5 m from RFID μPAD arrangement (Figure 4D). A rapid increase in absolute RSSI difference between testing and reference RFID tags indicates conductive buffer flow through the μPAD and presence of EBOV RNA in the sample. For the experimenter blinded multi-center evaluation (n = 12, 6 positive and 6 blank) of the fuse-like behavior of the EBOV RT-RPA CRISPR RFID μPAD, samples contained either 0 aM (-) or 11 aM (+) of EBOV RNA trigger previously amplified via RT-RPA and incubated in Cas solution for 4 h, prior to running in the CRISPR μPAD RFID assembly.

Methods for ADAR-based RNA sensors

Cloning – For the sensor expression plasmids, we built custom entry vectors by isothermal assembly of dsDNA fragments using the NEBuilder HiFi DNA assembly mix (NEB #E2621). We generated fragments by PCR using high-fidelity Q5 polymerase (NEB #M0494), with in-house plasmids and custom-synthesized gBlocks (Integrated DNA Technologies) as templates. We designed the entry vectors such that the fluorescent protein expression cassettes harbor a multiple cloning site (MCS) without in-frame stop codons, insulated from the fluorescent proteins by sequences coding for 2A peptides. To assemble the final sensor plasmids, we ordered sensor sequences as long oligonucleotides (Sigma Aldrich) with 5' and 3' adapter sequences overlapping with the vectors around the HindIII site of the MCS. We made the oligonucleotides double-stranded by PCR and inserted the resulting dsDNA products into HindIII-linearized entry vectors using HiFi assembly mix.

To build ADAR-expressing plasmids, we used plasmids pmGFP-ADAR1-p150 and pmGFP-ADAR1-p110, kindly provided by Kumiko Ui-Tei (Addgene #117927 and #117928, respectively) as a starting point. We excised the GFP sequences from the plasmids by amplifying the backbones with Q5 polymerase before circularizing the PCR products with KLD mix (NEB #M0554). The MCP-ADAR sequence was amplified from plasmid MS2-adRNA-MCP-ADAR2DD(E488Q)-NES, kindly provided by Prashant Mali (Addgene #124705). After each cloning and transformation step, we verified the regions of interest in individual clones by Sanger sequencing (QuintaraBio, Azenta). We propagated all the plasmids in *Escherichia coli* Turbo (NEB #C2984) or Stable (NEB #C3040) strains, with 100 μg/mL carbenicillin (Teknova #C2110) for selection.

Human cell culture – We obtained cryopreserved HEK293FT cells from Invitrogen (#R70007) and maintained them in Dulbecco's modification of Eagle's medium (DMEM, Gibco #10569010) supplemented with 10% v/v fetal bovine serum (FBS, Gibco #16000044) and 1X MEM non-essential amino acids (Gibco #11140050). Both wild-type and MALAT1 knock-out A459 cells were kindly provided by Sven Diederichs (DKFZ Heidelberg, Germany) [Gutschner *et al.*, 2011]; we propagated these cells in Ham's F-12K (Kaighn's) Medium (Gibco #21127030) supplemented with 10% v/v FBS. We grew all the cells in a humidified atmosphere at 37^{o}C with 5% CO_2, and split the cells using trypsin-EDTA (Gibco #25300054) every 2-3 days to ensure they did not surpass 80% confluence. We used cells at low passage numbers (<15) for all experiments.

C2C12 cell culture and differentiation – We obtained C2C12 cells from ATCC (CRL-1772) and maintained the cells in culture in DMEM supplemented with 10% v/v FBS. Care was taken to ensure that they did not exceed 50% confluence. For differentiation to the muscle lineage, we allowed the cells to become fully confluent (which we defined as day 0) one day after transfections, at which point we switched the growth medium to DMEM supplemented with 2% v/v horse serum (Cytiva #SH3007402) and 1X insulin-transferrin-selenium supplement (Sigma Aldrich #I3146). We replaced the growth medium every 48 hr until the end of the differentiation experiment. For differentiation to the bone lineage, we grew the cells in DMEM + 10% v/v FBS supplemented with 1000 ng/mL recombinant BMP-2 (R&D Systems #355BEC025) for 5 days prior to transfection with DART VADAR sensor plasmids.

Transfections – We used Lipofectamine 3000 (Invitrogen #L3000015) for transient transfections. We transfected cells at 70-90% confluence. In each well of a 96-well plate, we transfected a total of 150 ng plasmid DNA, which included 50 ng of each

plasmid (sensor, ADAR, and/or target). When leaving out one or several plasmids, we standardized the mass of transfected plasmids by adding a filler plasmid (carrying an Fluc2 gene with or without a promoter). For each well, we diluted 0.5 μL of P3000 reagent in a final volume of 5 μL of OptiMEM (Gibco #51985091), as well as 0.5 μL of Lipofectamine in 5 μL of OptiMEM. For larger culture vessels, we scaled up the transfections according to the area of the plates. We analyzed the cells 48 hr after transfection.

Fluorescence analyses – We analyzed fluorescent protein expression by flow cytometry. To do so, we harvested cells 48 hr after transfection using trypsin-EDTA. We washed the cells three times with flow cytometry buffer, made of phosphate buffered saline without calcium or magnesium (Corning #21031CV) supplemented with 1% FBS and 5 mM EDTA. We kept cells on ice until analysis with the HTS module of a BD LSR-II flow cytometer (Koch Institute flow cytometry core). We analyzed the data using Matlab scripts (based on https://github.com/jonesr18/MATLAB_Flow_Analysis). As a general strategy, we binned cell populations according to their transfection levels, at half-log intervals in the TagBFP-Pacific Blue channel (Figure 21).

Microscopy – For the imaging of HEK293FT cells, we transfected cells in a tissue-culture treated polystyrene 24-well plate. After 48 hr, we replaced the growth medium of the transfected cells with Hank's balanced salts solution without phenol red (Sigma Aldrich #H6648) and proceeded with the imaging at room temperature. We collected the images on a Nikon Ti-E inverted microscope equipped with a Nikon CFI S Plan Fluor ELWD 20X0.45 NA objective. We used a Nikon Intensilight C-HGFIE mercury lamp for illumination, and the following filters for mNeonGreen: a 470/40 excitation filter and a 425/50 emission filter (Chroma #49002). We acquired images with a Hamamatsu

ORCA-Flash 4.0 CMOS camera controlled with NIS Elements AR 4.13.05 software.

RNA editing analysis – We transfected HEK293FT cells in triplicates in 6-well plates with the appropriate plasmids. After 48 hr, we harvested the cells with trypsin-EDTA; we then washed the cells with flow cytometry buffer and used fluorescence-activated cell sorting (FACS) to isolate transfected cells (TagBFP-positive cells, detected in the Pacific Blue channel). We sorted the cells directly in the lysis buffer from the Qiagen RNeasy Mini kit (#74106), and stored the homogenized samples at -80^{o}C until we proceeded with total RNA extraction following the manufacturer's instructions. A third-party company (Quintara Biosciences) produced cDNAs by reverse transcription of the sensor regions using an EasyQuick RT MasterMix (Cwbio #CW2019M) and primers CTGAAACAGGCAGGAGATGTGGA / CCGCATGTAAGCAGACTTCCTCT (5'→3'). The samples were then sequenced on an Illumina MiSeq platform using a MiSeq Reagent Nano Kit v2 (300-cycles). We estimated editing efficiency by aligning the reads of each sample using Geneious mapper at medium sensitivity with up to 5 iterations per alignment, and used a custom Matlab script to detect A-to-G substitutions at each nucleotide position.

Quantification of gene expression – At each timepoint, we harvested cells from 16 wells of a 96-well plate using 1 mL of Tri-reagent RT (Molecular Research Center #RT111), and vortexed the samples vigorously for 5 min. We stored samples in the Tri-reagent at -80^{o}C until extraction. After thawing the samples, we added 50 μL of 4-bromoanisole (Thermo Scientific #A1182422) to the homogeneate, vortexed and stored the samples on ice for 5 min prior to a 21,000 rcf centrifugation at 4^{o}C for 15 min. From the upper, clear aqueous phase, we carefully harvested 500 μL that we thoroughly mixed 1:1 with isopropanol. We applied the mixture on a silica spin column (Epoch Life

Table 5 – Oligonucleotides for RT-qPCR of murine genes

Name	Sequence (5' to 3')	Application
org1462_csnk2a2_qpcr_f	CCGGAGGCCCTAGATCTTCTTGAC	RT-qPCR for murine casein kinase 2 alpha 2
org1463_csnk2a2_qpcr_r	GGGACTGCTCCTTCACCACC	RT-qPCR for murine casein kinase 2 alpha 2
org1464_myog_qpcr_f	TTGCTCAGCTCCCTCAACCAG	RT-qPCR for murine myogenin
org1465_myog_qpcr_r	AGCCGCGAGCAAATGATCTC	RT-qPCR for murine myogenin
org1472_myh7_qpcr_f	GGCGCATCAAGGAGCTCACC	RT-qPCR for murine myosin heavy chain I
org1473_myh7_qpcr_r	CCTGCTCCTCCGCCTCCTC	RT-qPCR for murine myosin heavy chain I
org1476_alpl_qpcr_f	CACCTGCCTTACCAACTCTTTTGTG	RT-qPCR for murine alkaline phosphatase
org1477_alpl_qpcr_r	GGCTACATTGGTGTTGAGCTTTTGG	RT-qPCR for murine alkaline phosphatase

Science #1910), which we spun and washed three times, once with buffer RW1 (Qiagen #1053394) and twice with buffer RPE (Qiagen #1018013). We eluted the samples in nuclease-free water and checked the RNA quality and concentration using a Nanodrop spectrophotometer. We then used about 100 ng of total RNA in each RT-qPCR reaction using the Luna Universal One-Step RT-qPCR Kit (NEB #E3005), set up according to manufacturer's instructions and analyzed on a CFX Opus 96 instrument (Bio-Rad) in the SYBR-green channel. We normalized C2C12 gene expression within each biological sample to the levels of the housekeeping gene Csnk2a2. Primer sequences are available in Table 5.

Luciferase assays – At each time point of interest, we sacrificed wells transfected with the combinations of plasmids of interest. In each well of a 96-well plate containing 100 µL of growth medium, we added another 100 µL of Nano-Glo lysis/reaction buffer

(Promega #N1110/N3040) reconstituted following manufacturer's recommendations. We vigorously pipetted to ensure complete homogeneization, and incubated the samples for 5 min at room temperature; we then transferred 150 μL of each sample to a white-bottom 96-well plate and measured luminescence on a ClarioStar Plus instrument (BMG Labtech) set with an acquisition window of 480/70 nm.

Staining – We stained C2C12 cells with Hoechst 33342 (Thermo Fisher #62249) and carboxyfluorescein succinimidyl ester (CFSE, Invitrogen #65085084) during differentiation to the muscle lineage. We diluted 1 μL Hoechst staining solution (20 mM stock) and 1 μL of 1000X CFSE (10 mM stock in DMSO) in 1 mL PBS and added 100 μL of this working staining solution to one well in a 96-well plate. We incubated the samples at room temperature protected from light for 10 minutes. Afterwards, we washed the wells three times with PBS prior to imaging on an EVOS M5000 microscope equipped with DAPI and GFP light cubes (Invitrogen #AMEP4950, AMEP4951). To generate images overlaying the DAPI (Hoechst) and GFP (CFSE) channels, we used the "Merge channels" function in Fiji 2. For the functional evaluation of alkaline phosphatase expression in C2C12s treated with BMP-2, we fixed the cells with a paraformaldehyde-based buffer (Biolegend #420801) for 10 minutes at room temperature protected from light. We then washed the cells with water and subsequently stained with nitro blue tetrazolium chloride and 5-bromo-4-chloro-3-indolyl-1-phosphate (BCIP/NBT, Sigma Aldrich #AB0300). We then washed the samples again with water, prior to imaging with an iPhone 12 mini (dual 12 MP, f/1.6 aperture, and iOS 15.5 software) mounted on a light transmission microscope.

DART VADAR sensor design – The general workflow for designing DART VADAR sensors is described in Figure 39.

Figure 39 – General workflow for designing DART VADAR sensors. We provide a step-by-step guide for designing DART VADAR sensors with MS2 hairpins. Instructions are tailored for our specific DART VADAR sensor expression cassette (distributed through Addgene) but can be transposed to other vectors, as long as the reading frame is preserved.

Bibliography

Almeida, A., Mitchell, A. L., Boland, M., Forster, S. C., Gloor, G. B., Tarkowska, A., Lawley, T. D. and Finn, R. D. (2019). A new genomic blueprint of the human gut microbiota. Nature *568*, 499–504.

Alon, U. (2006). An Introduction to Systems Biology: Design Principles of Biological Circuits. Chapman and Hall, CRC Press, London.

Angenent-Mari, N. M., Garruss, A. S., Soenksen, L. R., Church, G. and Collins, J. J. (2019). Deep Learning for RNA Synthetic Biology. bioRxiv *872077*, https://10.1101/872077.

Angenent-Mari, N. M., Garruss, A. S., Soenksen, L. R., Church, G. and Collins, J. J. (2020). A deep learning approach to programmable RNA switches. Nature Communications *11*, 1–12.

Arthur, M., Molinas, C., Mabilat, C. and Courvalin, P. (1990). Detection of erythromycin resistance by the polymerase chain reaction using primers in conserved regions of erm rRNA methylase genes. Antimicrobial Agents and Chemotherapy *34*, 2024–2026.

Badu-Tawiah, A. K., Lathwal, S., Kaastrup, K., Al-Sayah, M., Christodouleas, D. C., Smith, B. S., Whitesides, G. M. and Sikes, H. D. (2015). Polymerization-based signal amplification for paper-based immunoassays. Lab on a Chip *15*, 655–659.

Barker, K., Rastogi, S. K., Dominguez, J., Cantu, T., Brittain, W., Irvin, J. and Betancourt, T. (2016). Biodegradable DNA-enabled poly(ethylene glycol) hydrogels prepared by copper-free click chemistry. Journal of Biomaterials Science, Polymer Edition *27*, 22–39.

Bashor, C. J. and Collins, J. J. (2018). Understanding Biological Regulation Through Synthetic Biology. Annu. Rev. Biophys. *47*, 399–423.

Bauer, M. R., Krämer, A., Settanni, G., Jones, R. N., Ni, X., Khan Tareque, R., Fersht, A. R., Spencer, J. and Joerger, A. C. (2020). Targeting cavity-creating p53 cancer mutations with small-molecule stabilizers: the Y220X paradigm. ACS Chemical Biology *15*, 657–668.

Bayer, T. S. and Smolke, C. D. (2005). Programmable ligand-controlled riboregulators of eukaryotic gene expression. Nat. Biotechnol. *23*, 337–343.

Becskei, A. and Serrano, L. (2000). Engineering stability in gene networks by autoregulation. Nature *405*, 590–593.

Blake, W. J., KÆrn, M., Cantor, C. R. and Collins, J. J. (2003). Noise in eukaryotic gene expression. Nature *422*, 633–637.

Cai, W., Xie, S., Zhang, J., Tang, D. and Tang, Y. (2017). An electrochemical impedance biosensor for Hg2+ detection based on DNA hydrogel by coupling with DNAzyme-assisted target recycling and hybridization chain reaction. Biosensors and Bioelectronics *98*, 466–472.

Cangialosi, A., Yoon, C. K., Liu, J., Huang, Q., Guo, J., Nguyen, T. D., Gracias, D. H. and Schulman, R. (2017). DNA sequence–directed shape change of photopatterned hydrogels via high-degree swelling. Science *357*, 1126–1130.

Chen, J. S., Ma, E., Harrington, L. B., Da Costa, M., Tian, X., Palefsky, J. M. and Doudna, J. A. (2018). CRISPR-Cas12a target binding unleashes indiscriminate single-stranded DNase activity. Science *360*, 436–439.

Conrad, N. K. and Steitz, J. A. (2005). A Kaposi's sarcoma virus RNA element that increases the nuclear abundance of intronless transcripts. The EMBO journal *24*, 1831–1841.

COSMIC database (2021). Catalogue Of Somatic Mutations In Cancer, version 95. Entry ID: COSV52760651.

CRyPTIC Consortium (2018). Prediction of Susceptibility to First-Line Tuberculosis Drugs by DNA Sequencing. New England Journal of Medicine *379*, 1403–1415.

Elowitz, M. B. and Leibler, S. (2000). A synthetic oscillatory network of transcriptional regulators. Nature *403*, 335–338.

Elowitz, M. B., Levine, A. J., Siggia, E. D. and Swain, P. S. (2002). Stochastic gene expression in a single cell. Science *297*, 1183–1186.

English, M. A., Gayet, R. V. and Collins, J. J. (2021). Designing biological circuits: synthetic biology within the operon model and beyond. Annual Review of Biochemistry *90*, 221–244.

English, M. A., Soenksen, L. R., Gayet, R. V., de Puig, H., Angenent-Mari, N. M., Mao, A. S., Nguyen, P. Q. and Collins, J. J. (2019). Programmable CRISPR-responsive smart materials. Science *365*, 780–785.

Fu, E., Lutz, B., Kauffman, P. and Yager, P. (2010). Controlled reagent transport in disposable 2D paper networks. Lab on a Chip *10*, 918–920.

Gam, J. J., DiAndreth, B., Jones, R. D., Huh, J. and Weiss, R. (2019). A 'poly-transfection' method for rapid, one-pot characterization and optimization of genetic systems. Nucleic Acids Research *47*, e106–e106.

Gao, L., Cox, D. B., Yan, W. X., Manteiga, J. C., Schneider, M. W., Yamano, T., Nishimasu, H., Nureki, O., Crosetto, N. and Zhang, F. (2017). Engineered Cpf1 variants with altered PAM specificities increase genome targeting range. Nature biotechnology *35*, 789.

Gardner, T. S., Cantor, C. R. and Collins, J. J. (2000). Construction of a genetic toggle switch in Escherichia coli. Nature *403*, 339–342.

Gayet, R. V., de Puig, H., English, M. A., Soenksen, L. R., Nguyen, P. Q., Mao, A. S., Angenent-Mari, N. M. and Collins, J. J. (2020). Creating CRISPR-responsive smart materials for diagnostics and programmable cargo release. Nature protocols *15*, 3030–3063.

Gayet, R. V., Ilia, K., Razavi, S., Tippens, N. D., Lalwani, M. A., Zhang, K., Chen, J. X., Chen, J. C. and Collins, J. J. (2022). Autocatalytic base editing for RNA-responsive translational control. [Manuscript] *(unreviewed)*.

Gjorevski, N., Sachs, N., Manfrin, A., Giger, S., Bragina, M. E., Ordóñez-Morán, P., Clevers, H. and Lutolf, M. P. (2016). Designer matrices for intestinal stem cell and organoid culture. Nature *539*, 560–564.

Gootenberg, J. S., Abudayyeh, O. O., Kellner, M. J., Joung, J., Collins, J. J. and Zhang, F. (2018). Multiplexed and portable nucleic acid detection platform with Cas13, Cas12a and Csm6. Science *360*, 439–444.

Gootenberg, J. S., Abudayyeh, O. O., Lee, J. W., Essletzbichler, P., Dy, A. J., Joung, J., Verdine, V., Donghia, N., Daringer, N. M., Freije, C. A., Myhrvold, C., Bhattacharyya, R. P., Livny, J., Regev, A., Koonin, E. V., Hung, D. T., Sabeti, P. C., Collins, J. J. and Zhang, F. (2017). Nucleic acid detection with CRISPR-Cas13a/C2c2. Science *356*, 438–442.

Green, A. A., Silver, P. A., Collins, J. J. and Yin, P. (2014). Toehold Switches: de-novo-designed regulators of gene expression. Cell *159*, 925–939.

Guido, N. J., Wang, X., Adalsteinsson, D., McMillen, D., Hasty, J., Cantor, C. R., Elston, T. C. and Collins, J. J. (2006). A bottom-up approach to gene regulation. Nature *439*, 856–860.

Gutschner, T., Baas, M. and Diederichs, S. (2011). Non-coding RNA gene silencing through genomic integration of RNA destabilizing elements using zinc finger nucleases. Genome Research *21*, gr.122358.111.

Hajian, R., Balderston, S., Tran, T., deBoer, T., Etienne, J., Sandhu, M., Wauford, N. A., Chung, J. Y., Nokes, J., Athaiya, M., Paredes, J., Peytavi, R., Goldsmith, B., Murthy, N., Conboy, I. M. and Aran, K. (2019). Detection of unamplified target genes via CRISPR–Cas9 immobilized on a graphene field-effect transistor. Nature Biomedical Engineering *3*, 427–437.

He, Y., Wu, Y., Fu, J. Z. and Wu, W. B. (2015). Fabrication of paper-based microfluidic analysis devices: a review. RSC Advances *5*, 78109–78127.

Heitzer, E., Ulz, P. and Geigl, J. B. (2015). Circulating tumor DNA as a liquid biopsy for cancer. Clinical Chemistry *61*, 112–123.

Hooshangi, S., Thiberge, S. and Weiss, R. (2005). Ultrasensitivity and noise propagation in a synthetic transcriptional cascade. PNAS *102*, 3581–3586.

Huang, X., Lv, J., Li, Y., Mao, S., Li, Z., Jing, Z., Sun, Y., Zhang, X., Shen, S., Wang, X., Di, M., Ge, J., Huang, X., Zuo, E. and Chi, T. (2020). Programmable C-to-U RNA editing using the human APOBEC3A deaminase. The EMBO Journal *39*, e104741.

Iglesias, P. A. and Ingalls, B. P., eds (2009). Control theory and systems biology. MIT Press, Cambridge.

Ilia, K. and Del Vecchio, D. (2022). Squaring a circle: to what extent are traditional circuit analogies impeding synthetic biology? GEN Biotechnology *1*, 150–155.

Isaacs, F. J., Hasty, J., Cantor, C. R. and Collins, J. J. (2003). Prediction and measurement of an autoregulatory genetic module. PNAS *100*, 7714–7719.

Jiang, K., Koob, J., Chen, X. D., Krajeski, R. N., Zhang, Y., Villiger, L., Zhou, W., Abudayyeh, O. O., Chen, F. and Gootenberg, J. S. (2022). Programmable eukaryotic protein expression with RNA sensors. bioRxiv *(unreviewed)*, 2022.01.26.477951.

Johns, N. I., Gomes, A. L. C., Yim, S. S., Yang, A., Blazejewski, T., Smillie, C. S., Smith, M. B., Alm, E. J., Kosuri, S. and Wang, H. H. (2018). Metagenomic mining of regulatory elements enables programmable species-selective gene expression. Nature Methods *15*, 323–329.

Jumper, J., Evans, R., Pritzel, A., Green, T., Figurnov, M., Ronneberger, O., Tunyasuvunakool, K., Bates, R., Žídek, A., Potapenko, A., Bridgland, A., Meyer, C., Kohl, S. A., Ballard, A. J., Cowie, A., Romera-Paredes, B., Nikolov, S., Jain, R., Adler, J., Back, T., Petersen, S., Reiman, D., Clancy, E., Zielinski, M., Steinegger, M.,

Pacholska, M., Berghammer, T., Bodenstein, S., Silver, D., Vinyals, O., Senior, A. W., Kavukcuoglu, K., Kohli, P. and Hassabis, D. (2021). Highly accurate protein structure prediction with AlphaFold. Nature 2021 596:7873 *596*, 583–589.

Kahn, J. S., Trifonov, A., Cecconello, A., Guo, W., Fan, C. and Willner, I. (2015). Integration of Switchable DNA-Based Hydrogels with Surfaces by the Hybridization Chain Reaction. Nano Letters *15*, 7773–7778.

Kaseniit, K. E., Katz, N., Kolber, N. S., Call, C. C., Wengier, D. L., Cody, W. B., Sattely, E. S. and Gao, X. J. (2022). Modular and programmable RNA sensing using ADAR editing in living cells. bioRxiv *(unreviewed)*, 2022.01.28.478207.

Katagiri, T., Yamaguchi, A., Komaki, M., Abe, E., Takahashi, N., Ikeda, T., Rosen, V., Wozney, J. M., Fujisawa-Sehara, A. and Suda, T. (1994). Bone morphogenetic protein-2 converts the differentiation pathway of C2C12 myoblasts into the osteoblast lineage. The Journal of Cell Biology *127*, 1755–1766.

Katrekar, D., Chen, G., Meluzzi, D., Ganesh, A., Worlikar, A., Shih, Y. R., Varghese, S. and Mali, P. (2019). In vivo RNA editing of point mutations via RNA-guided adenosine deaminases. Nature Methods *16*, 239–242.

Khalil, A. S. and Collins, J. J. (2010). Synthetic biology: applications come of age. Nat. Rev. Genet. *11*, 367–379.

Kleinstiver, B. P., Tsai, S. Q., Prew, M. S., Nguyen, N. T., Welch, M. M., Lopez, J. M., McCaw, Z. R., Aryee, M. J. and Joung, J. K. (2016). Genome-wide specificities of CRISPR-Cas Cpf1 nucleases in human cells. Nature Biotechnology *34*, 869–874.

Knott, G. J. and Doudna, J. A. (2018). CRISPR-Cas guides the future of genetic engineering. Science *361*, 866–869.

Konermann, S., Lotfy, P., Brideau, N. J., Oki, J., Shokhirev, M. N. and Hsu, P. D. (2018). Transcriptome Engineering with RNA-Targeting Type VI-D CRISPR Effectors. Cell *173*, 665–676.

Kundert, K., Lucas, J. E., Watters, K. E., Fellmann, C., Ng, A. H., Heineike, B. M., Fitzsimmons, C. M., Oakes, B. L., Qu, J., Prasad, N., Rosenberg, O. S., Savage, D. F., El-Samad, H., Doudna, J. A. and Kortemme, T. (2019). Controlling CRISPR-Cas9 with ligand-activated and ligand-deactivated sgRNAs. Nature Communications 2019 10:1 *10*, 1–11.

Lee, H. H., Chou, K. S. and Huang, K. C. (2005). Inkjet printing of nanosized silver colloids. Nanotechnology *16*, 2436–2441.

Li, J. and Mooney, D. J. (2016). Designing hydrogels for controlled drug delivery. Nature Reviews Materials *1*.

Li, S. Y., Cheng, Q. X., Liu, J. K., Nie, X. Q., Zhao, G. P. and Wang, J. (2018). CRISPR-Cas12a has both cis- and trans-cleavage activities on single-stranded DNA. Cell Research *28*, 491–493.

Licht, K., Hartl, M., Amman, F., Anrather, D., Janisiw, M. P. and Jantsch, M. F. (2019). Inosine induces context-dependent recoding and translational stalling. Nucleic Acids Research *47*, 3.

Lin, D. C., Yurke, B. and Langrana, N. A. (2004). Mechanical properties of a reversible, DNA-crosslinked polyacrylamide hydrogel. Journal of Biomechanical Engineering *126*, 104–110.

Liu, B., Salgado, S., Maheshwari, V. and Liu, J. (2016). DNA adsorbed on graphene and

graphene oxide: Fundamental interactions, desorption and applications. Current Opinion in Colloid and Interface Science *26*, 41–49.

Lu, C. H., Yang, H. H., Zhu, C. L., Chen, X. and Chen, G. N. (2009). A graphene platform for sensing biomolecules. Angewandte Chemie - International Edition *48*, 4785–4787.

Lubelsky, Y. and Ulitsky, I. (2018). Sequences enriched in Alu repeats drive nuclear localization of long RNAs in human cells. Nature *555*, 107.

Magro, L., Jacquelin, B., Escadafal, C., Garneret, P., Kwasiborski, A., Manuguerra, J. C., Monti, F., Sakuntabhai, A., Vanhomwegen, J., Lafaye, P. and Tabeling, P. (2017). Paper-based RNA detection and multiplexed analysis for Ebola virus diagnostics. Scientific Reports *7*.

Manohar, S., Mantz, A. R., Bancroft, K. E., Hui, C. Y., Jagota, A. and Vezenov, D. V. (2008). Peeling single-stranded DNA from graphite surface to determine oligonucleotide binding energy by force spectroscopy. Nano Letters *8*, 4365–4372.

Martino, M. M., Briquez, P. S., Güç, E., Tortelli, F., Kilarski, W. W., Metzger, S., Rice, J. J., Kuhn, G. A., Muller, R., Swartz, M. A. and Hubbell, J. A. (2014). Growth factors engineered for super-affinity to the extracellular matrix enhance tissue healing. Science *343*, 885–888.

McCown, P. J., Wang, M. C., Jaeger, L. and Brown, J. A. (2019). Secondary structural model of human MALAT1 reveals multiple structure-function relationships. International Journal of Molecular Sciences *20*, 5610.

Meng, F. and Ellis, T. (2020). The second decade of synthetic biology: 2010–2020. Nature Communications 2020 11:1 *11*, 1–4.

Mitton-Fry, R. M., DeGregorio, S. J., Wang, J., Steitz, T. A. and Steitz, J. A. (2010). Poly(A) tail recognition by a viral RNA element through assembly of a triple helix. Science *330*, 1244–1247.

Mustjoki, S. and Young, N. S. (2021). Somatic mutations in "benign" disease. New England Journal of Medicine *384*, 2039–2052.

Na, W., Nam, D., Lee, H. and Shin, S. (2018). Rapid molecular diagnosis of infectious viruses in microfluidics using DNA hydrogel formation. Biosensors and Bioelectronics *108*, 9–13.

Okolie, C. E., Wooldridge, K. G., Turner, D. P., Cockayne, A. and James, R. (2015). Development of a heptaplex PCR assay for identification of Staphylococcus aureus and CoNS with simultaneous detection of virulence and antibiotic resistance genes. BMC Microbiology *15*.

Ozbudak, E. M., Thattai, M., Kurtser, I., Grossman, A. D. and Van Oudenaarden, A. (2002). Regulation of noise in the expression of a single gene. Nature Genetics *31*, 69–73.

Parant, H., Muller, G., Le Mercier, T., Tarascon, J. M., Poulin, P. and Colin, A. (2017). Flowing suspensions of carbon black with high electronic conductivity for flow applications: Comparison between carbons black and exhibition of specific aggregation of carbon particles. Carbon *119*, 10–20.

Pardee, K., Green, A. A., Ferrante, T., Cameron, D. E., Daleykeyser, A., Yin, P. and Collins, J. J. (2014). Paper-based synthetic gene networks. Cell *159*, 940–954.

Pardee, K., Green, A. A., Takahashi, M. K., Braff, D., Lambert, G., Lee, J. W., Ferrante, T., Ma, D., Donghia, N., Fan, M., Daringer, N. M., Bosch, I., Dudley, D. M., O'Connor,

D. H., Gehrke, L. and Collins, J. J. (2016). Rapid, Low-Cost Detection of Zika Virus Using Programmable Biomolecular Components. Cell *165*, 1255–1266.

Pawlyta, M., Rouzaud, J. N. and Duber, S. (2015). Raman microspectroscopy characterization of carbon blacks: Spectral analysis and structural information. Carbon *84*, 479–490.

Peters, B., Nielsen, M. and Sette, A. (2020). T-cell epitope predictions. Annual Reviews in Immunology *38*, 123–145.

Poduri, A., Evrony, G. D., Cai, X. and Walsh, C. A. (2013). Somatic mutation, genomic variation, and neurological disease. Science *341*, 1237758.

Poulsen, H., Nilsson, J., Damgaard, C. K., Egebjerg, J. and Kjems, J. (2001). CRM1 mediates the export of ADAR1 through a nuclear export signal within the Z-DNA dinding domain. Molecular and Cellular Biology *21*, 7862–7871.

Previtera, M. L. and Langrana, N. A. (2014). Preparation of DNA-crosslinked polyacrylamide hydrogels. Journal of Visualized Experiments *90*, 51323.

Purcell, B. P., Lobb, D., Charati, M. B., Dorsey, S. M., Wade, R. J., Zellars, K. N., Doviak, H., Pettaway, S., Logdon, C. B., Shuman, J. A., Freels, P. D., Gorman, J. H., Gorman, R. C., Spinale, F. G. and Burdick, J. A. (2014). Injectable and bioresponsive hydrogels for on-demand matrix metalloproteinase inhibition. Nature Materials *13*, 653–661.

Qian, Y., Li, J., Zhao, S., Matthews, E., Adoff, M., Zhong, W., An, X., Yeo, M., Park, C., Wang, B.-S., Southwell, D. and Huang, Z. J. (2022). Programmable RNA sensing for cell monitoring and manipulation. bioRxiv *(unreviewed)*, 2022.05.25.493141.

Qin, M., Sun, M., Bai, R., Mao, Y., Qian, X., Sikka, D., Zhao, Y., Qi, H. J., Suo, Z. and He, X. (2018). Bioinspired Hydrogel Interferometer for Adaptive Coloration and Chemical Sensing. Advanced Materials *30*.

Qureshi, N. K., Yin, S. and Boyle-Vavra, S. (2014). The role of the staphylococcal VraTSR regulatory system on vancomycin resistance and vana operon expression in vancomycin-resistant staphylococcus aureus. PLoS ONE *9*.

Rauch, S., He, E., Srienc, M., Zhou, H., Zhang, Z. and Dickinson, B. C. (2019). Programmable RNA-guided RNA effector proteins built from human parts. Cell *178*, 122–134.

Rosales, A. M. and Anseth, K. S. (2016). The design of reversible hydrogels to capture extracellular matrix dynamics. Nature Reviews Materials *1*.

Rosenfeld, N., Young, J. W., Alon, U., Swain, P. S. and Elowitz, M. B. (2005). Gene regulation at the single-cell level. Science *307*, 1962–1965.

Sberro, H., Fremin, B. J., Zlitni, S., Edfors, F., Greenfield, N., Snyder, M. P., Pavlopoulos, G. A., Kyrpides, N. C. and Bhatt, A. S. (2019). Large-Scale Analyses of Human Microbiomes Reveal Thousands of Small, Novel Genes. Cell *178*, 1245–1259.

Schmidt, C. M. and Smolke, C. D. (2019). RNA Switches for Synthetic Biology. CSH Perspect. Biol. *11*, a032532.

Sedlmayer, F., Aubel, D. and Fussenegger, M. (2018). Synthetic gene circuits for the detection, elimination and prevention of disease. Nature Biomedical Engineering *2*, 399–415.

Shao, S. and Hegde, R. S. (2011). Membrane protein insertion at the endoplasmic reticulum. Annual Review of Cell and Developmental Biology *27*, 25–56.

Siu, K. H. and Chen, W. (2018). Riboregulated toehold-gated gRNA for programmable CRISPR–Cas9 function. Nature Chemical Biology *15*, 217–220.

Song, Y., Yang, W., Fu, Q., Wu, L., Zhao, X., Zhang, Y. and Zhang, R. (2020). irCLASH reveals RNA substrates recognized by human ADARs. Nature Structural & Molecular Biology *27*, 351–362.

Spahr, M., Gilardi, R. and Bonacchi, D. (2016). Carbon black for electrically conductive polymer applications. In Fillers for Polymer Applications. Polymers and Polymeric Composites: A Reference Series., (Rothon, R., ed.),. Springer NYC.

Strommenger, B., Kettlitz, C., Werner, G. and Witte, W. (2003). Multiplex PCR assay for simultaneous detection of nine clinically relevant antibiotic resistance genes in Staphylococcus aureus. Journal of Clinical Microbiology *41*, 4089–4094.

Sugimoto, S., Sato, F., Miyakawa, R., Chiba, A., Onodera, S., Hori, S. and Mizunoe, Y. (2018). Broad impact of extracellular DNA on biofilm formation by clinically isolated Methicillin-resistant and -sensitive strains of Staphylococcus aureus. Scientific Reports *8*.

Sun, L., Park, S. S., Sheberla, D. and Dincă, M. (2016). Measuring and Reporting Electrical Conductivity in Metal-Organic Frameworks: Cd2(TTFTB) as a Case Study. Journal of the American Chemical Society *138*, 14772–14782.

Tabula Sapiens Consortium (2022). The Tabula Sapiens: a multiple-organ, single-cell transcriptomic atlas of humans. Science (New York, N.Y.) *376*, eabl4896.

Takyar, S., Hickerson, R. P. and Noller, H. F. (2005). mRNA helicase activity of the ribosome. Cell *120*, 49–58.

Townshend, B., Xiang, J. S., Manzanarez, G., Hayden, E. J. and Smolke, C. D. (2021). A multiplexed, automated evolution pipeline enables scalable discovery and characterization of biosensors. Nature Communications 2021 12:1 *12*, 1–15.

Turkevich, J., Stevenson, P. C. and Hillier, J. (1951). A study of the nucleation and growth processes in the synthesis of colloidal gold. Discussions of the Faraday Society *11*, 55–75.

Uhlén, M., Fagerberg, L., Hallström, B. M., Lindskog, C., Oksvold, P., Mardinoglu, A., Sivertsson, A., Kampf, C., Sjöstedt, E., Asplund, A., Olsson, I. M., Edlund, K., Lundberg, E., Navani, S., Szigyarto, C. A. K., Odeberg, J., Djureinovic, D., Takanen, J. O., Hober, S., Alm, T., Edqvist, P. H., Berling, H., Tegel, H., Mulder, J., Rockberg, J., Nilsson, P., Schwenk, J. M., Hamsten, M., Von Feilitzen, K., Forsberg, M., Persson, L., Johansson, F., Zwahlen, M., Von Heijne, G., Nielsen, J. and Pontén, F. (2015). Tissue-based map of the human proteome. Science *347*.

Valeri, J. A., Collins, K. M., Ramesh, P., Alcantar, M. A., Lepe, B. A., Lu, T. K. and Camacho, D. M. (2020). Sequence-to-function deep learning frameworks for engineered riboregulators. Nature Communications *11*, 5058.

Voigt, C. A. (2020). Synthetic biology 2020–2030: six commercially-available products that are changing our world. Nature Communications 2020 11:1 *11*, 1–6.

Walton, R. T., Christie, K. A., Whittaker, M. N. and Kleinstiver, B. P. (2020). Unconstrained genome targeting with near-PAMless engineered CRISPR-Cas9 variants. Science *368*, 290–296.

Wang, K. W., Betancourt, T. and Hall, C. K. (2018). Computational Study of DNA-Cross-

Linked Hydrogel Formation for Drug Delivery Applications. Macromolecules *51*, 9758–9768.

Wei, B., Cheng, I., Luo, K. Q. and Mi, Y. (2008). Capture and release of protein by a reversible DNA-induced sol-gel transition system. Angewandte Chemie - International Edition *47*, 331–333.

Wei, J., Lotfy, P., Faizi, K., Wang, E., Slabodkin, H., Kinnaman, E., Chandrasekaran, S., Kitano, H., Durrant, M. G., Duffy, C. V., Hsu, P. D. and Konermann, S. (2022). Deep learning and CRISPR-Cas13d ortholog discovery for optimized RNA targeting. bioRxiv *(unreviewed)*, 2021.09.14.460134.

Wei, X., Tian, T., Jia, S., Zhu, Z., Ma, Y., Sun, J., Lin, Z. and Yang, C. J. (2015). Target-responsive DNA hydrogel mediated stop-flow microfluidic paper-based analytic device for rapid, portable and visual detection of multiple targets. Analytical Chemistry *87*, 4275–4282.

Weissman, J. S. (2010). The epistemology of cell biology. Molecular biology of the cell *21*, 3825.

Wilusz, J. E., JnBaptiste, C. K., Lu, L. Y., Kuhn, C.-D., Joshua-Tor, L. and Sharp, P. A. (2012). A triple helix stabilizes the 3' ends of long noncoding RNAs that lack poly(A) tails. Genes & development *26*, 2392–407.

Woerner, A. C., Frottin, F., Hornburg, D., Feng, L. R., Meissner, F., Patra, M., Tatzelt, J., Mann, M., Winklhofer, K. F., Hartl, F. U. and Hipp, M. S. (2016). Cytoplasmic protein aggregates interfere with nucleocytoplasmic transport of protein and RNA. Science (New York, N.Y.) *351*, 173–176.

Wu, M. R., Nissim, L., Stupp, D., Pery, E., Binder-Nissim, A., Weisinger, K., Enghuus, C., Palacios, S. R., Humphrey, M., Zhang, Z., Maria Novoa, E., Kellis, M., Weiss, R., Rabkin, S. D., Tabach, Y. and Lu, T. K. (2019). A high-throughput screening and computation platform for identifying synthetic promoters with enhanced cell-state specificity (SPECS). Nature Communications 2019 10:1 *10*, 1–10.

Wu, Z., Yang, H. and Colosi, P. (2010). Effect of genome size on AAV vector packaging. Molecular Therapy *18*, 80–86.

Xu, Y., Sheng, K., Li, C. and Shi, G. (2010a). Self-assembled graphene hydrogel via a one-step hydrothermal process. ACS Nano *4*, 4324–4330.

Xu, Y., Wu, Q., Sun, Y., Bai, H. and Shi, G. (2010b). Three-dimensional self-assembly of graphene oxide and DNA into multifunctional hydrogels. ACS Nano *4*, 7358–7362.

Yang, H., Liu, H., Kang, H. and Tan, W. (2008). Engineering target-responsive hydrogels based on aptamer-target interactions. Journal of the American Chemical Society *130*, 6320–6321.

Zhao, E. M., Mao, A. S., de Puig, H., Zhang, K., Tippens, N. D., Tan, X., Ran, F. A., Han, I., Nguyen, P. Q., Chory, E. J., Hua, T. Y., Ramesh, P., Thompson, D. B., Oh, C. Y., Zigon, E. S., English, M. A. and Collins, J. J. (2021). RNA-responsive elements for eukaryotic translational control. Nature Biotechnology *40*, 539–545.

Zhu, Z., Wu, C., Liu, H., Zou, Y., Zhang, X., Kang, H., Yang, C. J. and Tan, W. (2010). An aptamer cross-linked hydrogel as a colorimetric platform for visual detection. Angewandte Chemie - International Edition *49*, 1052–1056.